UNIVERSITY
OF TRENTO - Italy
Department of Materials Engineering
and Industrial Technologies

Doctoral School in Materials Engineering – XXII cycle

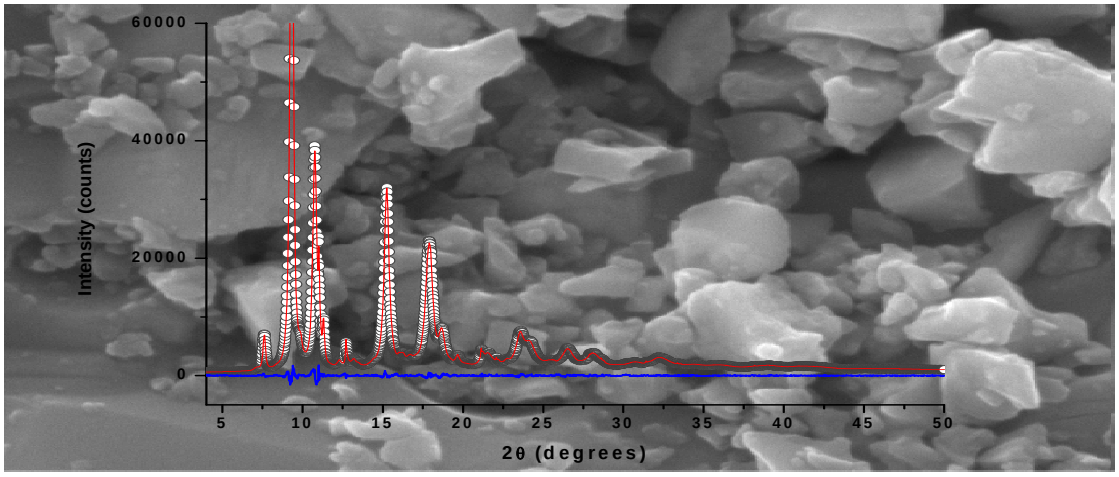

Nanostructured Copper Oxides: Production and Applications

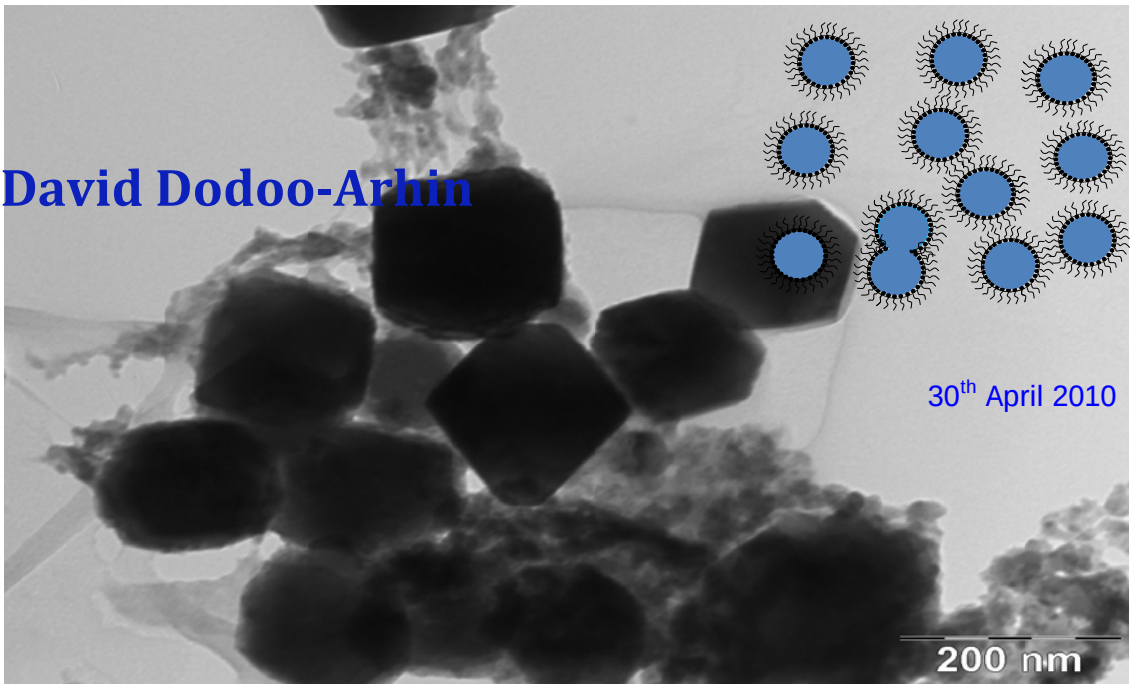

Accepted on the recommendation of:

Prof. Paolo Scardi - Università degli studi di Trento
Facoltà di Ingegneria – Dip. Ing. Materiali e Tecnologie Industriali
Via Mesiano, 77 - 38100 Trento
Tel.: 0461/282417-2476
E-mail: Paolo.Scardi@unitn.it

Prof. Matteo Leoni – Università degli studi di Trento
Facoltà di Ingegneria - Dip.Ing.Materiali e Tecnologie Industriali
Via Mesiano, 77-38100 Trento
Tel.: +39 0461/282416-2467
E-mail: Matteo.Leoni@unitn.it

Prof. Claudio Migliaresi - Università degli Studi di Trento
DIMTI: - Via Mesiano, 77 - 38123 Trento
Tel. +390461/281916; Fax 0461/281977;
E-mail: Claudio.Migliaresi@ing.unitn.it

Prof. Cristina Siligardi - Università degli Studi di Modena e Reggio Emilia
Dipartimento di Ingegneria dei Materiali e dell'Ambiente
Via Vignolese 905 - 41100 Modena
Tel. +39-059 2856236; fax 059 2056243

Prof. Pranesh B. Aswath - University of Texas at Arlington
Mechanical and Aerospace Engineering Department
500 West First Street, Rm. 325 - Arlington, TX 76019 (USA)
Tel. 817-272-7108;
E-mail: aswath@uta.edu.
Webpage: http://www.uta.edu/ra/real/editprofile.php?onlyview= l&pid=5

Author Email: david.dodooarhin@unitn.it

Dedication

I dedicate this thesis work to my wife Barbara,

my children Paolo and Emmanuel

as well as my family

for their unconditional love, sacrifice, encouragement and support.

ABSTRACT

Abstract

Cuprite (Cu_2O) and tenorite (CuO) have been extensively studied because of their potential use in several electronic applications, which include solar cells and gas sensors, just to mention the most appealing ones. Both materials are p-type semiconductors, the one with a wide bandgap (Cu_2O, 2.0 eV-2.2 eV), the other with a much narrower one (CuO, 1.2 eV-1.8 eV), and both show interesting optical properties in the visible and near-visible range.

This Thesis work is devoted to the synthesis, characterisation and application of nanostructured copper oxides in the field of renewable energies. Within this broad scope the Thesis focuses on:

- production of defect-free nanocrystals (Cu_2O & CuO) and investigation of the correlation between experimental parameters and resulting microstructure;
- production of highly defective nanocrystalline Cu_2O powders, with the estimation of the effect of milling on microstructure and phase transformations;
- production of inks for photonic applications in photovoltaic cells.

Reverse micelle microemulsions (a bottom-up approach) have been employed for the production of the defect-free nanocrystals. Models have been proposed for the nanocrystal formation and growth, validated by means of several techniques such as X-ray Diffraction (XRD), Scanning Electron Microscopy (SEM) and Transmission Electron Microscopy (TEM), UV-Visible and Fourier Transform InfraRed spectroscopy (UV-Vis and FTIR). The produced nanocrystals show good crystallinity with Cu_2O and CuO exhibiting cuboidal and rod-like structures, respectively. The nanometric nature of the primary domains (20 nm – 4 nm) leads to quantum confinement phenomena highlighted by photoluminescence measurements.

A top-down approach has been exploited to produce highly defective

particles to be possibly employed in new-generation intermediate-band solar cells. A high-energy mill, suitably modified to work in controlled temperature and environment, allowed the production of highly defective copper oxides with little or no phase transformation and contamination from the mill. Finely dispersed powders with a high density of line defects ($\rho \approx 4\times10^{-16}$ m^{-2}) were ultimately obtained. The effect of milling on the microstructure evolution was investigated using both traditional and synchrotron radiation XRD line profile analysis supported by High Resolution TEM and SEM.

The synthesised powders were employed for the production of copper oxide inks for photonic applications. Those inks would allow solar cells to be directly printed on a substrate, with a dramatic reduction of production costs and the possibility of coating objects of any shape. Sprayed films usually need high consolidation temperatures: the proposed formulation, on the contrary, allows sintering of the ink-derived films at a relatively low temperature (below 600 °C), thus making possible the deposition on inexpensive substrates such as aluminium. Prototype solar cells based on the copper oxide inks have been fabricated using simple coating techniques. Results can be considered as a first step towards the production of fully recyclable solar cells, made of low-cost raw materials and realized by cost-effective deposition techniques.

Acknowledgements

I wish to thank, Prof Paolo Scardi (Tutor) for giving me all this opportunity to reach this very important ladder in my academic /professional life. Thanks for agreeing and accepting me in spite of the background to XRD. Though it may seem an opportunity and training for an individual, it is actually for generations near and far.

Matteo Leoni (Co-Tutor); you have really taught me the rudiments of scientific research and how to live and work in a scientific field. Thanks for all the strategies applied to guide me, and the big heart you had especially when things went the other way. Thanks also for all the software training sessions and encouragement.

Special thanks to Prof. John Justice Fletcher (*Old J.J*) of SNAS, Ghana Atomic Energy Commission for this wonderful opportunity to become a scientist. Your encouragements, ideals, ideas, and most importantly your determination to guide and urge on young naive students to become important figures in academia/professional life cannot be over looked. You are not only a tutor/supervisor but a real father of many generations. Thanks for believing in and encouraging me to undertake such a herculean task.

Dr. Arianna Lopresti is thanked for all the encouragement, advice during my search for collaboration (Senegal) as well as during my PhD studies here in Italy. Thanks to Prof. Djibril Diop of the Cheik Anta Diop University, Senegal as well as the conference organizers of the 1st African School on X-rays in Materials (2005) where it all began.

Emmanuel Garnier (Universitè de Poitiers, France) thanks for all the tutorials you gave me in the micellar synthesis techniques as well as pieces of advice: they are really appreciated.

Dr. Mirco D'Incau; thanks for all the help you gave to me in the lab and in

the thesis work. Most importantly, you will forever be remembered as an Angel during the most difficult time of my PhD life: you were there just on time, Cristy (You are a valuable sister. Thanks for all the love, encouragement, tutoring, advice, help and for accepting me to live with you during my initial arrival in Italy); Hector Pesenti (thanks for teaching me most of the initial laboratory practical tools and processes. You are not just an under tutor and Friend but a really cherished brother). Valeria Tagliazucca (FTIR and Chemistry advisor. I appreciate your love and care. You are a valuable friend), Caterina Zanella (Electrochemistry); Aylin, Romain and Enrico Moser. You were really helpful.

Dr. Gloria Ischia and Prof. Gianellela are acknowledged for all the TEM analysis and discussions. Prof. Ceccato for BET analysis and technical advice on solar cells. Thanks to Prof. Marilena Vasilescu, Dr. Daniel Angelescu and Dr. Mihaela Negoi (Romanian Institute of Physical Chemistry and Politehnica University of Bucharest) for their help and useful discussions.

Giovanna Carlà, ("Mama Joana"),thank you so much for being my first family on arrival in Trento; I thank you on behalf of myself and my entire family in Ghana for all you did and continue to do. You will forever be remembered.

Sara Benvenuto, thank you for all that you did.Thanks to Matteo Ortolani, Luca, Alexandro Ligabò, Guissepe, Saliou Diouf, Sergio Setti, Wilma Vaona, Fabrizio, Ken Beryerlein, Melanie, Mahmoud, Yasemine and all colleagues in the materials engineering Department.

The Nangah Family at Trieste (Rose, Spura, Mammy, Rene, Priscilla) and all the special people who helped me during my stay in Italy are duly acknowledged.

Thanks finally to the European Synchrotron Radiation Facility (ESRF, Grenoble, France) for beam time at the ID31 diffraction beamline work station.

David Dodoo-Arhin

Trento, Italy-April 2010

Contents

Contents

List of Figures

List of Tables

CHAPTER 1

1.Introduction

Copper oxides represent a very useful reference systems for the study of complex cuprates, most of which show high-T_c superconductivity. In fact, the discovery of the superconducting mixed-valence copper oxides and the possible role of magnetic interactions which facilitate the high T_c superconductivity have intensified the interest in these binary oxides. Many cuprates during chemical substitutions tend to show phase separation and insulator-to-metal transition. As shown in the literature, the different levels of this transition are usually observed as an increase in the infrared (IR) absorption within the dielectric gap, and the subsequent formation of the low-energy tail due to the itinerant carriers [1].

Cuprous (Cu_2O) and cupric (CuO) oxides (cuprite and tenorite, respectively) are the two most important stochiometric compounds in the copper-oxygen (Cu-O) system. Both materials are intrinsic p-type semiconductors with narrow energy band gaps (2.1 eV for Cu_2O, 1.2 eV for CuO) and exhibit a variety of interesting properties that can be fully exploited is several fields. Applications have been envisaged in solar cells [2], Li-ion battery systems (negative electrode material) [3], superconductors [4], magnetic storage systems [5], gas sensors [6], photothermal [6] and photoconductive systems [7]. Copper oxides are known to be ideal compounds in the study of electron-correlation effects on the electronic structure of transition metal compounds in general and in high T_c superconductors. Changes in the electronic structure of these semiconductor materials at the nanometer scale significantly influence their properties due to quantum confinement effects.

Due to their peculiar properties, cuprite (Cu_2O) and tenorite (CuO) will be the main focus of the present thesis work "*Nanostructured copper oxides: production and applications*": profiting of the properties obtained in nanocrystalline materials and of the intrinsic properties of copper oxides, possible

future applications are envisaged in the field of low-cost solar cells. In particular three features has been identified as currently missing in the literature:

- a way of producing cuprite nanoparticles free of defects
- a way of producing cuprite nanoparticles rich in defects
- a way of producing cuprite films using a cost-effective printing technology based on photonic inks

The need for nanoparticles can be sought in the properties that they would show in solar cells. For randomly generated charge carriers, in fact, the average diffusion time (τ) from the bulk to the surface is given by $\tau = r^2/\pi^2 D$ [8], where r is the radius of the grain and D is the diffusion coefficient of the carrier. Hence, working with nanoparticles versus the currently used micron sized particles can drastically reduce the chances of phonon recombination, thereby improving the efficiencies of photovoltaic devices. The nanoparticles free of defects could serve to this application. The massive presence of defects, on the other hand, could lead to the formation of an intermediate band (in the band gap) that would increase the overall efficiency of the device. This would be an ideal application for nanoparticles full of defects. Being able to produce the corresponding films via a simple ink-based route, could also lead to potential applications of the resulting cells, as the reduced efficiency versus silicon devices would be surpassed by the much lower costs of the material and of the production technique. The same techniques and the same nanoparticles would also be valuable in the field of gas sensing as the specific area would be increased [9 - 11].

The thesis work is structured in a set of chapters that represent extended versions of scientific articles that were produced during the thesis work. Some general features of both oxides and a general introduction of nanostructured materials and the current challenges behind their production will be briefly presented in this introduction.

1.1 Copper oxides: General overview

1.1.1 Cuprous oxide (Cu_2O)

The highly symmetric crystal lattice structure of cuprous oxide Cu_2O (Cubic, space group $Pn\bar{3}m$, ICDD PDF-2 card #05-0667, a = 4.267Å, *figure 1.1*) consists of Cu ions located on the conventional *fcc* lattice at the position (1/4, 1/4, 1/4) and the O^{2-} ions located on the *bcc* lattice at (3/4, 3/4, 3/4). In this structure, copper ions are linearly coordinated (two-fold) and oxygen ions are situated in the centre (four fold) of ideal tetrahedron coordinated with the Cu ions [12]. This structure may be also viewed as consisting of two independent and inter-penetrating O-Cu-O zig-zag frameworks with each one equivalent to the cristobalite structure.

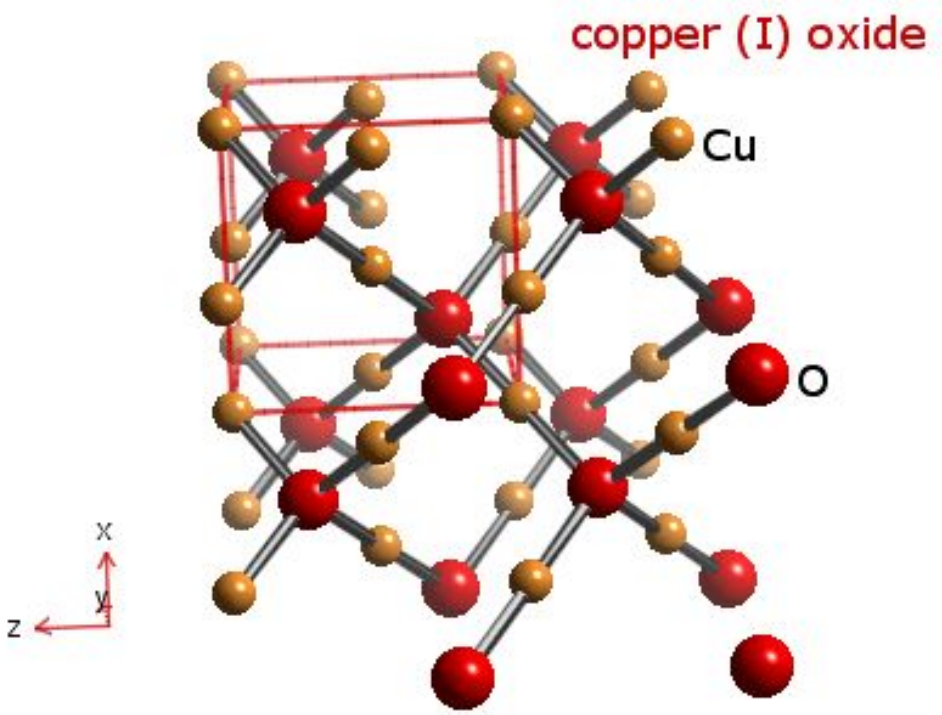

Figure 1. 1. *Schematic representation of the unit cell of Cu_2O. The small spheres (yellow) are the Cu atoms while the large spheres (red) are the oxygen atoms.*

Other physical properties of the material are shown in Table 1.1. As a simple

p-type semiconductor, its direct energy bandgap comprises a lower conduction band and upper valence band, which have the same parity making their electric dipoles forbidden. Furthermore, it exhibits interesting properties such as a rich excitonic structure with a large excitonic binding energy of 140 meV [13] which allows the observation of a well-defined series of excitonic features in the absorption and photoluminescence spectrum of bulk Cu_2O.

Density	6.10 g/cm^3
Molecular Mass	143.092 g/mol
Lattice Constants at room temperature	4.27 Å
Melting point	1235 °C
Relative permittivity	7.5
Conduction band Electron mass	0.98
Valence band Hole mass	0.58
Cu-O bond length	1.85 Å
O-O bond length	3.68 Å
Cu-Cu bond length	3.02 Å
Bandgap energy at room temperature (E_g)	2.09 eV
Specific heat capacity (Cp)	70 J/(K mol)
Thermal conductivity (k)	4.5 W/(K m)
Thermal diffusivity (α)	0.015 cm^2/s

Table 1. 1. ***Physical properties of Cu_2O (partly from [14]).***

Another important feature of Cu_2O is that it is capable of absorbing and adsorbing a relatively large amount of oxygen both in bulk and on the surface. This excess oxygen on the surface or in the bulk leads to p-type semiconducting behaviour and unique oxidation catalysis properties of Cu_2O. When Cu_2O is illuminated with visible light radiation in an aqueous media/moisture, these excess

oxygen species are released making it a unique material for photocatalytic splitting of H_2O into H_2 and O_2 [15].

It is worth stating that, the photovoltaic ability of Cu_2O was heightened by researchers during the mid-seventies due to its high optical absorption properties in the visible region of the electromagnetic spectrum; the material was identified as a possible low cost material for solar cell applications. Cuprite still remains an attractive alternative to silicon and other semiconductors for the fabrication of cheap solar cells for terrestrial applications. The advantage of the materials over others in the photovoltaic field include: (1) abundance, (2) easy preparation and (3) nontoxic nature. Cu_2O based solar cells are known to have a theoretical energy conversion efficiency of 22 % in AM1 (Air Mass 1, i.e. on the Earth surface at the equator) conditions [16, 17]. So far, the highest efficiency obtained for Cu_2O cells is 2% [18]. This inability to reach a high efficiency could be attributed to the fact that light generated charge carriers in the micron-sized grains are not sufficiently transferred to the surface and are lost due to recombination effect.

The literature is not very rich in papers dealing with the production of Cu_2O. For instance, Wei *et al.* [19] synthesized cuprous oxide via a simple solvothermal reduction route, whereas Musa *et al.* [20] produced copper oxide by thermal oxidation and studied its physical and electrical properties. Other synthesis methods include for instance electrochemical deposition [21], sonochemistry [22], sol-gel [23], RF reactive sputtering [24] and chemical vapour deposition (CVD) [25].

1.1.2 Cupric Oxide (CuO)

Studies on tenorite (CuO) have been carried out since the first decade of last century [26]. Cupric oxide (CuO) is a narrow energy bandgap (1.2 - 1.85 eV) p-type semiconductor, with a C2/c monoclinic crystalline structure [27]. The unit cell of CuO (ICDD PDF2 card# 72-0629, a = 4.6837Å, b = 3.4226 Å, c = 5.1288 Å, β = 99.54°), comprises Cu^{2+} ions which are coordinated by four (4) O^{2-} ions in an

approximately square planar configuration (*Figure 1.2*). Some of the physical features of the material are summarised in Table 1.2.

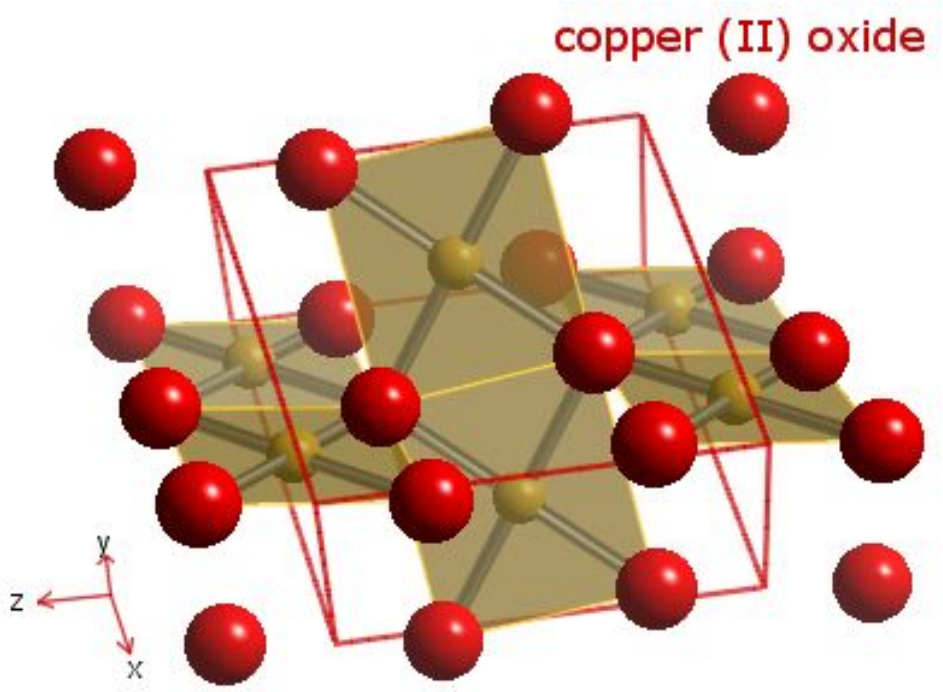

Figure 1. 2. *Crystal structure of CuO. Large spheres (red) are oxygen atoms and small spheres (yellow) are Cu atoms.*

It has been proposed in the literature [28], that a Jahn-Teller distortion in a highly symmetric divalent copper monoxide structure introduces a strong electron-phonon interaction, which causes the high Tc superconductivity in layered cuprates.

Due to its low-symmetry, CuO has been found to exhibit ferroelectric properties [29]. Moreover, the large but almost constant paramagnetic susceptibility at low temperature is attributable to the exchange interaction between Cu^{2+} ions via O^{2-} ions [30]. Bulk- and nano-CuO is thus used in preparation of a wide range of organic–inorganic nanostructured composites that possess unique characteristics such as giant magnetoresistance, high thermal and electrical

conductivities as well as high mechanical strength and high-temperature durability [31]. The ionicity of the Cu-O bonds increases CuO nanoparticles, which is very evident in the change in the optical band gap resulting in a blue shift [32]. The most remarkable envisaged applications of CuO are in gas sensor layers [33] and solar cells. Gas sensors and solar cells based on tenorite are of direct interest to our research. To produce those devices, nanocrystalline CuO structures have been synthesized by techniques such as sol-gel [34], molecular beam epitaxy [35], microemulsions [36] and sputtering [37]. Not just spherical particles but also nanowires [38] and quantum dots [39] have been created.

Density	$\rho = 6.32$ g/cm^3
Molecular Mass	79.55 g/mol
Lattice Constants at room temperature	a = 4.69Å, b = 3.42 Å, c = 5.13 Å, β = 99.54°
Melting point	1134°C
Relative permittivity	12.0
Conduction band Electron mass	0.16-0.46 m_e
Valence band Hole mass	0.54-3.7 m_e
Cu-O bond length	1.95Å
O-O bond length	2.62 Å
Cu-Cu bond length	2.90 Å
Bandgap energy at room temperature (Eg)	1.2eV

Table 1. 2.. ***Physical properties of CuO.***

1.2 The need for nanoparticles

Looking at the envisaged applications and to the main aim of this thesis work, a common need is to work with a nanostructured material. In the recent

decades, nanostructure science and technology has become one of the most interesting, diverse and fast growing research areas in materials science and engineering. Some emerging multidisciplinary fields of applications have appeared such as nanoelectronics, nanostructured sensors (nano-nose) and nanostructured solar cells.

A clear classification and discussion on the use of nanomaterials can be found in the pioneering work of Gleiter and coworkers in the early 1980s [40]. The main idea behind the nanoscience is to control and/or engineer the structural, physical, chemical or biological properties of materials on the nanometer (atomic) scale. It is worth stating that, in some cases the properties of these materials can be very different (most often superior) in comparison to the macroscale (bulk) properties of the same material. Most of the properties of say, a homogeneous bulk spherical solid material with macroscopic dimensions are related to its crystal structure and chemical composition. The surface atoms of this bulk material comprise a negligible proportion of the total number of its constituent atoms and hence play a negligible role in the observed (bulk) properties of the material. However, that surface atoms may play a predominant role in properties involving exchanges at the interface between the material and the surrounding medium such as crystal growth, chemical reactivity and thermal conductivity.

When the size of the particles is reduced to the nanometric scale, the proportion of atoms located at a surface area is considerably high in relation to the total volume of atoms in the material. This has a strong effect on the materials properties. For instance, at 5nm (ca. 8000 atoms) the proportion of surface atoms is estimated to be about 20 % whilst at 2nm (ca. 500 atoms), it stands at 50%. Assuming that the particles are spherical in shape, then the surface area to volume ratio can be given as $S/V = 3/r$ where r is the radius of the particle. Decreasing the particle radius increases the surface area to volume ratio. For instance, a 1 cm^3 of 1 nm sized particles would have an active surface area of about 100 m^2 [41]. From the literature [42], it is known that the effective thermal conductivity of

suspensions containing spherical particles increases with the volume fraction of the solid particles. Since heat transfer takes place at the surface of the particles, it is preferable to use particles with a large surface area to volume ratio. Thus, if nanometer-sized particles could be suspended in traditional heat transfer fluids, a new class of engineered fluids with high thermal conductivity, called "nanofluids" [43-44], and highly sensitive gas sensors such as the nano-nose could be fabricated.

Because of the extremely small size of the grains (domains) of nanomaterials, a large fraction of the atoms in these materials is located in the grain boundaries which impede movement of dislocations, thereby allowing the material to exhibit a superior physical, mechanical, magnetic, electronic and biometric properties in comparison with coarse-grained/bulk (>1 μm) materials. This phenomenon is attributed to the fact that the grain boundary energy of nanocrystalline powders (*see Chapter 3*) is larger than the grain boundary energy of fully equilibrated grain boundary [45].

Furthermore, these materials show increased strength, high hardness, extremely high diffusion rates, and consequently reduced sintering times for powder compaction. This idea has also been considered in the sintering of the photonics inks (*Chapter 5*) produced in this study.

Because of the small size particles, semiconductor nanoparticles may show quantum confinement, a phenomenon, which arises due to the fact that the electronic energy levels do not form a continuous set but rather, discrete in nature [46]. Hence, emissions from excited nanoparticles tend to show size-dependent vibrational frequencies: this property makes most nanoparticles useful in memory storage, sensor and electronics technologies [47, 48]. Most semiconductor and metallic nanoparticles show strong particle size-,-shape-and surrounding media-dependent optical properties.

The synthesis of nanomaterials and the creation of nanostructures are achieved mainly through two complementary approaches identified as top-down

and bottom-up (*see Figure 1.3*).

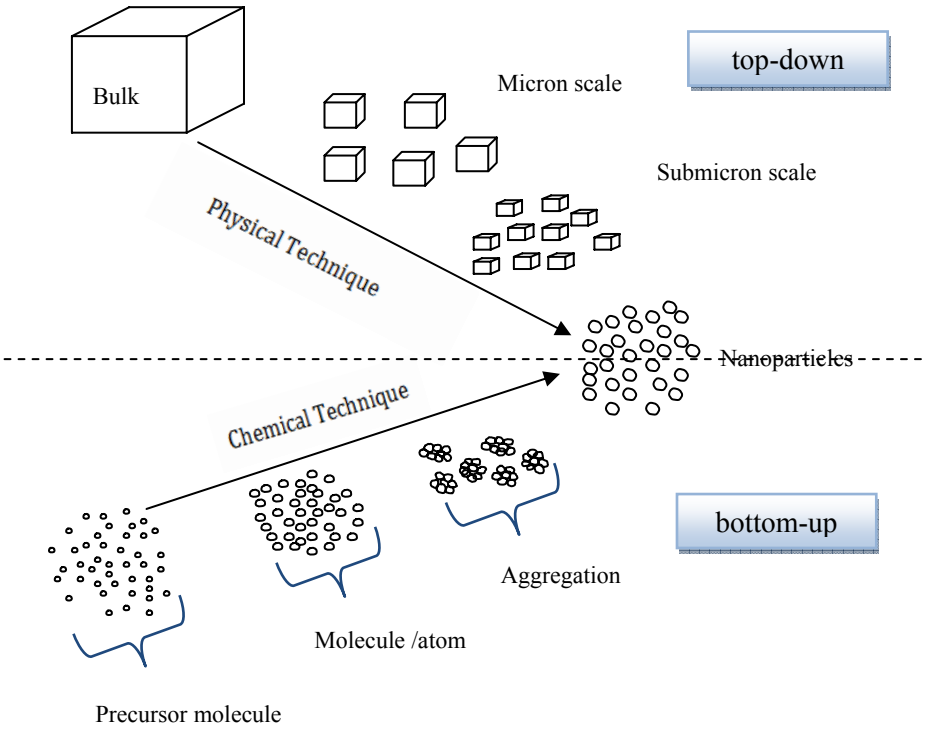

Figure 1. 3. *The two complementary approaches to nanoparticles synthesis.*

The top-down approach involves whittling down the size of materials from the bulk (macroscopic) to the nanometer scale. This approach generally relies on physical processes, or a combination of physical and/or chemical, electrical or thermal processes for their production. Usually the top-down approach is cost-effective but the control over the produced material is poor.

The bottom-up approach, on the contrary, involves assembling atom-by-atom, or molecule-by molecule into structures on the nanometer scale with properties varying according to the number of constituent entities/grain size. Building the system atom by atom or molecule by molecule guarantees the best control over all particles in the system. Colloidal dispersions such as

microemulsions are a good example of the bottom-up concept of nanoparticles synthesis.

Both the top-down and the bottom-up approaches have been employed in this thesis for the synthesis of Cu_2O nanoparticles (Chapter 2), to fabricate nanostructured Cu_2O powders (Chapter 3), for the synthesis of CuO nanorod-like structures (Chapter 4) and to finally produce cuprite-based photonics inks (Chapter 5).

It will be shown that the bottom-up approach is unique to produce nanoparticles free of defects, whereas the top-down approach cannot produce nanoparticles if not full of dislocations. It will also be seen how both techniques can be potentially used for the production of photonics inks and how the top-down approach, providing more “active” particles, could lead to the material with the highest sinterability and therefore the most promising conditions for practical applications.

REFERENCES

1 B A Gizhevskii, Y. P. Sukhorukov, N. N. Loshkareva, A. S. Moskvin, E. V. Zenkov and E. A. Kozlov, "Optical absorption spectra of nanocrystalline cupric oxide: possible effects of nanoscopic phase separation", *J. Phys.: Condens. Matter* **17**, 499–506, (2005) (http://arxiv.org/abs/cond-mat/0312009v1)

2 A. Mittiga, E. Salza, F. Sarto, M. Tucci, and R. Vasanthi. "Heterojunction solar cell with 2% efficiency based on a Cu_2O substrate". *Applied Physics Letters*, **88**, 163502, (2006).

3 D. Zhang, Y. Tang-Hong, Chun-Hua Chen, "Cu nanoparticles derived from CuO electrodes in lithium cells", *Nanotechnology*, **16,** 2338–2341, (2005).

4 J. B Goodenough, "Bond-length fluctuations in the copper oxide superconductors," *Topical Review J. Phys.: Condens. Matter,* **15**, R257–R326, (2003).

5 R.V. Kumar, Y. Diamant, A. Gedanken, "Sonochemical synthesis of cerium oxide nanoparticles effect of additives and quantum size effect", *Chem. Mater.*, 1**2,** 2301, (2000).

6 S.T. Shishiyanu,T S. Shishiyanu and O. I. Lupa, "Novel NO_2 gas sensor based on cuprous oxide thin films", *Sensors and Actuators B: Chemical*, **113,[1]**,468-476,(2006)

7 J. Herion, E.A. Niekisch and G. Scharl, "Investigation of metal oxide/cuprous oxide heterojunction solar cells", *Solar Energy Materials,* **vol. 4, [1]**, 101-112, (1980).

8 G. Rothenberger, J. Moser, M. Gratzel, N. Serpone, and D. K. Sharma, "Charge carrier trapping and recombination dynamics in small semiconductor particles," *J. Am. Chem. Soc.*; **107[26]**, 8054–8059,(1985).

9 S. Saito, M. Maryayama, K. Kaumoto, H. Yanagida, "Gas Sensing Characteristics of Porous ZnO and Pt/ZnO Ceramics", *J. Am. Ceram. Soc.*, **68**, 40-43, (1985).

10 T.S. Şişianu, V.P. Şontea, O.I. Lupan, S.T. Şişianu, S.K. Railean and I.I.

Pocaznoi, “Cuprous oxide films prepared by a low cost chemical deposition and photon annealing technique for sensors applications”, *Proceedings of the Third International Conference on Microelectronics and Computer Science*, **1**, 288–292,(2002).

11 E. Traversa, “Intelligent ceramic materials for chemical sensors,” *J. Intel. Mater. Syst. Struct.*, **6,** 860, (1995).

12 R. Restori, D. Schwarzenbach, “Charge density in cuprite, Cu_2O”, *Acta Crystallogr. B***, 42**, 201, (1986).

13 K. Borgohain, N. Murase, S. Mahamuni, “Synthesis and properties of Cu_2O quantum particles”, *Journal of applied physics,* **92, [3]**, 1292–1297, (2002)

14 F. Biccari, “Defects and Doping in Cu_2O”, *PhD thesis*, Università di Roma Sapienza, (2009).

15 B. J. Wood, H. Wise and R. S. Yolles, “Selectivity and stoichiometry of copper oxide in propylene oxidation”, *J. Catal.*, **15**, 355, (1969).

16 E. Y. Wang, D. Trivich, H. Sawalha and G. Thomas, “Proc. COMPILES Int. Conf., Dhahran, Saudi Arabia, in Heliotech and Dev., **1**, 643,(1976).

17 L. C. Olsen, F. W. Addis, and W. Miller. “Experimental and theoretical studies of Cu_2O solar cells,” *Solar Cells*, **7,** 247, (1982).

18 A. Mittiga, E. Salza, F. Sarto, M. Tucci, and R. Vasanthi, “Heterojunction solar cell with 2% efficiency based on a Cu_2O substrate”, *Applied Physics Letters*, **88,** 163502, (2006).

19 M. Wei, N. Lun, X. Ma and S. Wen, “A simple solvothermal reduction route to copper and cuprous oxide”, *Materials Letters,* **Vol. 61, [11-12]**, 2147-2150, (2007).

20 Musa A.O, Akomolafe T, Carter M.J., “Production of cuprous oxide a solar cell material, by thermal oxidation and study of its physical and electrical properties,” *Solar Energy Mater Solar Cells,* **51,** 305–316, (1998).

21 J.K. Barton, A.A. Vertegel, E.W. Bohannan, J.A. Switzer, “Epitaxial Electrodeposition of Cuprous Oxide onto Single-Crystal Copper,” *Chem.*

Mater., **13**, 952, (2001).

22 R.V. Kumar, Y. Mastai, Y. Diamant, A. Gedanken, "Sonochemical synthesis of amorphous Cu and nanocrystalline Cu_2O embedded in a polyaniline matrix", *J. Mater. Chem.*, **11**, 1209, (2001).

23 L. Armelao, D. Barreca, M. Bertapelle, G. Bottaro, C. Sada, E. Tondello, "A sol-gel approach to nanophasic copper oxide thin films", *Thin Solid Films,* **442**, 48–52, (2003).

24 S. Ghosh, D.K Avasthi, P. Shah, V. Ganesan, A. Gupta, D. Saransgi, R. Bhattacharya, W. Assmann, "Deposition of thin films of different oxides by RF reactive sputtering and their characterization". *Vacuum*, **57**,377–385, (2000).

25 P.R. Markworth, X. Liu, J.Y. Dai, W. Fan, T.J. Marks, R.P.H. Chang, "Coherent island formation of Cu_2O films grown by chemical vapour deposition on MgO(110)", *J. Mater. Res.*, **16**, 2408, (2001).

26 V.W. Klemm and W. Schuth, "Magnetochemical investigations: Magnetic measurements of cupric compound, a contribution to the theory of magnetism of transition elements", *Z. Anorg. Allg. Chem.*, **203**, 104, (1931).

27 S. A. Sbrink and L.-J. Norrby, "A refinement of the crystal structure of copper(II) oxide with a discussion of some exceptional e.s.d.'s," *Acta Crystallogr. B*, **26**, 8, (1970).

28 J. Bednorz and K. Muller, "Perovskite-type oxides-The new approach to high-Tc superconductivity", *Rev. Mod. Phys.,* **60**, 585, (1988).

29 T. Kimura, Y. Sekio, H. Nakamura, T. Siegrist, and A. P. Ramirez, "Cupric oxide as an induced-multiferroic with high-T_c", *Nature Mater.,* **7**, 291 (2008).

30 M. O'Keeffe and F. S. Stone, "The Magnetic Susceptibility of Cupric Oxide", *J. Phys. Chem. Solids*, **23**, 161, (1962).

31 C-L Huang, E. Matijevic´, "Coating of uniform inorganic particles with polymers: III. Polypyrrole on different metal oxides," *Journal of Materials Research*, **vol. 10, [5]**, 1327-1336, (1995).

32 K. Borgohain, J. B. Singh, M. V. Rama Rao, T. Shripathi, S. Mahamuni, "Quantum size effects in CuO nanoparticles", *Phys. Rev. B,* **61**, 11093- 11096 (2000).

33 Q. Wei, W. D. Luo, B. Liao, G.Wang, "Giant capacitance effect and physical model of nano crystalline CuO–$BaTiO_3$ semiconductor as a CO_2 gas sensor", *J. Appl. Phys.*, **88**, 4818, (2000).

34 L. Armelao, D. Barreca, M. Bertapelle, G. Bottaro, C. Sadac and E. Tondello, "A sol–gel approach to nanophasic copper oxide thin films," *Thin Solid Films*, **Vol. 442, [1-2]**, 48-52, (2003).

35 A. Catana, J-P. Locquet, S M. Paik and I.K. Schuller, "Local epitaxial growth of CuO films on MgO", *Phys. Rev. B*, **46**, 15477-15483, (1992).

36 D. Hana, H. Yang, C. Zhu and F. Wang, "Controlled synthesis of CuO nanoparticles using TritonX-100-based water-in-oil reverse micelles," *Powder Technology*, 185, [3], 286-290, (2008).

37 P Samarasekara, N T R N Kumara and N U S Yapa, "Sputtered copper oxide (CuO) thin films for gas sensor devices", *J. Phys.: Condens. Matter*, **18**, 2417–2420, (2006).

38 W. Wang, O.K Varghese, C. Ruan, M. Paulose and C. A Grimes, "Synthesis of CuO and Cu_2O Crystalline Nanowires Using $Cu(OH)_2$ Nanowire Templates", *J. Mater. Res.*, **18[12]**, 2756, (2003).

39 K. Borgohain and S. Mahamuni, "Formation of single-phase CuO quantum particles", *J. Mater., Res.*, **17**, 1219-1223, *DOI: 10.1557/JMR.2002.0180*, (2002).

40 H. Gleiter, "Nanocrystalline Materials", *Progress in Materials Science*, **33**,223–315, (1989).

41 N. Ichinose, Y. Ozaki, and S. Kashu. "Superfine Particle Technology", *Springer-Verlag*, New York, (1988).

42 J. C. Maxwell, "A Treatise on Electricity and Magnetism," 2nd ed., *Oxford University Press*, Cambridge, (1904).

43 U. S Choi, "Development and Applications of Non-Newtonian Flows". Ed. D.

A. Siginer and H. P. Wang. **Vol. 231/MD-Vol. 66.** New York: The ASME, (1995).

44 J. A. Eastman, S. Choi, S. Li, W. Yu, and L. J. Thompson. "Anomalously Increased Effective Thermal Conductivities of Ethylene Glycol-Based Nanofluids Containing Copper Nanoparticles", *Applied Physics Letters*, 78[6], 718-720, (2001).

45 A. Johnson, in: "New Materials by Mechanical Alloying Techniques", (E. Arzt and L. Schults, eds.), *Informationsgesellschaft Verlag*, Calw-Hirsau, 354, (1988).

46 D. Chakravorty, and A. K. Giri. "Chemistry of Advanced Materials". Ed. Rao, C. N. R. Boca Raton, FL: *Blackwell Scientific Publication*, (1993).

47 A.P. Alivisatos, "Semiconductor Clusters, Nanocrystals and Quantum Dots", *Science*, **271**, 933, (1996).

48 X .Wang, and Q. Gao. "Synthesis of Copper Nanoparticles in Nanoporous Nickel Phosphate VSB-1", *Solid State Phenomena,* **121, [123]**, 479-482, (2007).

CHAPTER 2

2. Synthesis, characterisation, and stability of Cu_2O nanoparticles produced via reverse micelles microemulsion[1]

ABSTRACT

Cuprite (Cu_2O) nanoparticles were synthesized at room temperature via reduction of $CuCl_2 \cdot 2H_2O$ by $NaBH_4$ in water/n-heptane microemulsion stabilised by the nonionic Brij-30 surfactant. Whole Powder Pattern Modelling of the X-ray diffraction patterns shows the presence of a bimodal size distribution in the nanopowders, with a fraction of domains in the 10 - 40 nm range and a smaller one below 10 nm. Linear and planar defects are absent.

A relationship between the average size of the larger particles and the quantity of water in the system was obtained. The stability of cuprite under visible light irradiation both during the synthesis and after the preparation was investigated, showing that a self-catalytic conversion of Cu_2O into CuO takes place in water.

2.1. INTRODUCTION

Nanoparticles of metals, semiconductors and oxides keep attracting the attention of the scientific community because of their exceptional and in some cases, unexpected physical and chemical properties coming from the quantum

[1] *Part of the results shown in the present chapter have been published in: D. Dodoo-Arhin, M. Leoni, P. Scardi, E. Garnier, A. Mittiga, "Synthesis, Characterization and stability of Cu_2O nanoparticles produced via reverse micelles microemulsion", Mater.chem. phys.,* doi:10.1016/j.matchemphys.2010.03.053 *(on line).*

confinement at the nano scale.

Synthesis of inorganic nanoparticles still remains a challenging task owing to intrinsic difficulties in the control of composition and morphology [1-3]. Among the proposed synthesis routes, water-in-oil (W/O) microemulsions are promising as they provide nanoreactors where size and morphology of nanoparticles can be well controlled [4-8].

Copper oxides are useful reference systems for the study of complex cuprates, most of which show high-Tc superconductivity. Of particular interest is cuprous oxide (Cu_2O cuprite), a p-type semiconductor due to the presence of Cu vacancies which form an acceptor level 0.4 eV above the valence band [9].

As such, Cu_2O is attracting the current interest owing to the wide range of potential applications. For instance, cuprite is a promising solar cell material (band gap of 2.0 - 2.2 eV [10]), but it can also be used as anode material for lithium ion batteries [11], as a photocatalyst for water splitting under visible light irradiation [12, 13] and as a sensing material in gas detectors [9].

For a wider application of the material, however, it would be necessary to have powders characterised by a nanometric size and free of lattice defects, often required to maximise the efficiency of the corresponding devices. Unfortunately, it is not easy to obtain nanopowders of controlled size and shape, with an intermediate valence (Cu^+ vs. Cu^0 or Cu^{2+}) and free of defects. Cu_2O particles with a controlled shape (e.g. cuboids [14], octahedral [15], or thick-shell hollow spheres [16]) have been synthesised, but they are far too large (few hundred nm) and imperfect to be useful. Yin et al. [17] were able to produce 5 nm cuprite nanoparticles (coated with a thin CuO layer), but their process leads to the presence of stacking defects. More recently, 10-15 nm nanoparticles were produced on multiwall carbon nanotubes [18], but in this case the particles are produced at high temperature and come already with a support, that in most cases is not necessary. The synthesis of cuprite nanoparticles in microemulsions seems promising, but

again a large quantity of defects seems always being present [19].

Furthermore, the analysis of the size of those nanoparticles as well as their structure is, in some cases, quite naive and can lead to severe errors (see e.g. [20] for the description of a common mistake): most authors use simplified diffraction-based techniques (e.g. the Scherrer formula [21]) or Transmission Electron Microscopy for the size analysis. Quoting an average "crystallite size" or obtaining a size distribution from the analysis of a few dozen well visible grains has a limited statistical validity. Simple yet advanced techniques nowadays exists for a complete structural and microstructural characterisation of nanocrystalline powders, based on the analysis of the whole X-ray diffraction (XRD) pattern, either by using the Whole Powder Pattern Modelling (WPPM) technique [22], or by the Debye equation [23]. In WPPM, microstructural parameters such as domain size, shape and distribution, as well as type and quantity of linear and planar defects, are employed to build a computer-generated diffraction pattern of the material under study. The parameters are then varied through a nonlinear least squares routine until the best fit is reached between model and experimental data. This guarantees a self consistent extraction of microstructural information from the measured XRD pattern [22, 24].

In this part of the work we report some results on room-temperature synthesis and characterisation of Cu_2O nanoparticles free of lattice defects. Powders produced via water-in-oil microemulsion and analysed both from the morphological, structural, microstructural and optical point of view, show a clear photoactivity.

2.2. EXPERIMENTAL

2.2.1. Materials and specimens

All experiments were conducted at room temperature (24 ± 2 °C) in a poorly illuminated environment: just in one case (*cf. Table 2.1*), the preparation was conducted under light, to test for photocatalytic effects.

Two sets of five batches (40 ml each) of microemulsion were prepared (identified as SA and SB, plus the batch number). The two batches differ in the quantity of water (*see below and cf. Table 2.1*), i.e. in the parameter ω = nH_2O/nBrij30, defined as the ratio between the number of molecules of water and surfactant in the system.

Sample	Brij30®		n-Heptane		0.2M $CuCl_2$	$NaBH_4$	H_2O	ω	<D>
		equiv.		equiv.			%		nm
	g	ml	g	ml	ml	mg			
SA1	6.287	6.62	22.430	32.99	0.4	31.0	1.0	1.3	16.8
SA2	6.289	6.62	22.158	32.99	0.8	61.0	2.0	2.6	12.1
SA3	6.285	6.62	21.891	32.99	1.2	92.0	3.0	3.8	10.0
SA4	6.286	6.62	21.613	32.99	1.6	122.0	4.0	5.1	15.0
SA5	6.287	6.62	21.345	32.99	2.0	152.0	5.0	6.4	16.1
SB1	6.284	6.62	22.434	32.99	0.4	31.0	1.0	1.3	29.7
SB2	6.286	6.62	22.153	32.99	0.8	61.0	2.0	2.6	14.5
SB3	6.286	6.62	21.886	32.99	1.2	91.0	3.0	3.8	10.0
SB4	6.284	6.62	21.614	32.99	1.6	122.0	4.0	5.1	15.0
SB5	6.286	6.62	21.332	32.99	2.0	152.0	5.0	6.4	16.1

Table 2. 1. ***Experimental parameters for the SA and SB sets. Both Brij30 and n-heptane have been weighted: the corresponding volume is reported for reference and to allow an easier calculation of ω.***

A stable inverse-micelle microemulsion was obtained by mixing oil and surfactant, and subsequently adding water. The oil-surfactant dispersion was created by mixing n-Heptane (Sigma Aldrich, 99% purity) with the non-ionic surfactant Brij30® (Polyoxyethylene 4 Lauryl Ether $(C_2H_4O)_n.C1_2H_{26}O$, n≈4, mean weight M = 362.6, Sigma Aldrich) in a 80.46/16.54 vol/vol ratio. The two components were weighted and mixed in a 200 ml high-density polyethylene graduated bottle, closed with a polypropylene cap (to limit the volatilization of the

hydrocarbon) after each mixing phase of the synthesis. The dispersion was sonicated for 3 min to favour the mixing of the two phases. Sonication was always done in a thermostatic bath (25 °C) at a frequency of 59 kHz and 125 W.

A 0.2 M solution of $CuCl_2.2H_2O$ (Sigma Aldrich, 6174-250GF) was formed by adding the salt to deionised water (<1.8 μS/cm). Variable aliquots of this solution (1 to 5 vol%, according to *Table 2.1*) were added to the dispersion and sonicated for 6 min in order to create a homogeneous microemulsion. At the end of the process a homogeneous and transparent sky-blue microemulsion free from any precipitate was obtained.

Sodium borohydride (Sigma Aldrich, 99% purity, 213462-25G) was used as reducing agent: a 1 wt% (0.400 mg) was added to the emulsion and sonicated for 1s to start the reaction. To limit unwanted products (e.g. CuO), the microemulsion was continuously stirred for 10 mins. The addition of the reducing agent turned the emulsion first to yellow and then to deep brown, with evident evolution of gas and absence of any precipitation.

To break the microemulsion, 20 ml of Acetone (purity 99%, Sigma Aldrich) were added. Breaking the micelles causes the nanoparticles to slowly precipitate, with a powder clearly becoming visible on the bottom of the bottle after 10 min. To remove the organic phase residuals, 40 ml of a 1:1 mixture of Acetone and Ethanol (purity 98%, Sigma Aldrich) was added to the gelatinous precipitate, mildly sonicated and centrifuged at 6000 rpm for 10 mins. Subsequently 20 ml ethanol and 20 ml deionised water were added to the dispersion that was sonicated and centrifuged again at 6000 rpm for 10 mins.

The particles were further washed several times with deionised water. When needed for the analysis, the particles were laid on an h00 silicon wafer and dried under Argon flux.

A commercial Cu_2O powder (Sigma Aldrich, 99% purity), named SC, was employed as a reference for the analyses. The SC powder was heat treated at 850

°C and 9.5 mbar for 40 min to remove any residual Cu.

2.2.2. Characterisation techniques

X-ray powder diffraction (XRD) patterns were collected on a Rigaku PMG-VH Bragg-Brentano diffractometer operating a copper tube at 40 kV and 30 mA. The goniometer is equipped with a high resolution set up (1° divergence slit, 2° incident and diffracted beam Soller slits, 0.15 mm receiving slit) and a curved-crystal graphite analyser, providing a narrow and symmetrical instrumental profile over the investigated angular range.

The instrumental resolution function was characterised with the NIST SRM 660a (LaB_6) standard [25]: all peak profiles were simultaneously fitted with symmetrical pseudo-Voigt functions whose width and shape were constrained according to the Caglioti *et al.* formulae [26]. The XRD patterns of all specimens were recorded in the 25°-85° 2θ range with a step size of 0.05° and a counting time of 60 s per step.

Microstructural analysis was performed using the Whole Powder Pattern Modelling (WPPM) method [22], using the PM2K software [27].

A Jeol JSM 5500 LV microscope operated at 20 kV was employed for the morphological characterisation: prior to investigation, specimens were sputtered with Au/Pd.

Spectrophotometry was performed on an UV-Vis-NIR V570 Jasco (Japan Spectroscopic Co. Ltd., Tokyo, Japan) spectrophotometer in air in the 200-1200 nm range. Transmission FTIR spectra were recorded on an Avatar 550 (Thermo Optics) instrument in the 4000-400 cm^{-1} range with 2 cm^{-1} resolution; the Spectrum v5.3.0 software was employed for the FTIR analysis.

2.3. RESULUTS AND DISCUSSION

2.3.1 Synthesis

The redox potential for the Cu^{2+}/Cu^{+} couple ($Cu^{2+}(aq) + e^{-}(aq) \rightarrow Cu^{+}(aq)$) is +0.153 V, i.e. less than half of the +0.34 V needed to fully reduce Cu^{2+} to Cu^{0} [28].

The water pools in reverse micellar solutions provide a large number of reaction sites which are separated from each other by the non-aqueous medium (oil/heptane) [29]. In aqueous solution, $CuCl_2$ dissociates into $[Cu(H_2O)_6]^{2+}$ ions (responsible of the sky blue colouring) and Cl^{-} anions, that can partially coordinate with the copper ions. In $[Cu(H_2O)_6]^{2+}$, the six water molecules completely surround the Cu^{2+} ion, shielding it. The addition of $NaBH_4$ to the microemulsion causes the following reaction (occurring in the water pools):

$$NaBH_4(s) + 2H_2O \longrightarrow NaBO_2(aq) + 4H_2(g) + heat \qquad (0.1)$$

Hydrogen, interacting with the hydroxyl ions, causes the production of solvated electrons:

$$H_2(g) + 2OH^{-} \rightarrow 2H_2O + 2e^{-}(aq) \qquad (0.2)$$

that can penetrate the hexaaquacopper(II) ion reducing it to $Cu^{+}(H_2O)_x$ (x=1-4) ions. The accessibility of the copper ion in those complexes is highly favoured, as the coordination with water is less strong [30]. The reduced Cu^{+} ion can lead to the formation of cuprite via the following reaction chain (*see e.g. [31]*):

$$Cu^{+}(aq) + H_2O \rightarrow CuOH(aq) + H^{+}(aq) \qquad (0.3)$$

$$2CuOH(aq) \longrightarrow Cu_2O(s) + H_2O \qquad (0.4)$$

The need to control the reaction, and in particular to control the H^{+}/OH^{-} ratio and the homogeneity of the OH^{-} distribution, is a requirement for the production of pure Cu_2O. In fact, in excess of OH^{-} and at temperature higher than room

temperature, CuO can also form through the following scheme [31]:

$$Cu^{+}(aq)+2OH^{-}(aq) \rightarrow Cu(OH)_2(aq) \quad (0.5)$$

$$Cu(OH)_2(aq) + 2OH^{-}(aq) \rightarrow Cu(OH)_4^{2-}(aq) \longleftrightarrow CuO(s) + 2OH^{-}(aq) + H_2O \quad (0.6)$$

The disproportionation of Cu+ can also lead to the full reduction of the copper ions to metallic copper as:

$$2Cu^{+}(aq) \rightarrow Cu^{2+}(aq)+Cu^{0}(aq) \quad (0.7)$$

Nanoparticles formed inside reverse micelles may undergo further growth or aggregation yielding particles larger than their initial nanodroplets, which may result in a bimodal size distribution.

2.3.2. X-ray diffraction analysis and transmission electron microscopy

The XRD patterns of the various specimens show a predominant presence of Cu_2O with traces of CuO and Cu appearing for increasing ω (*see Figure 2.1*)

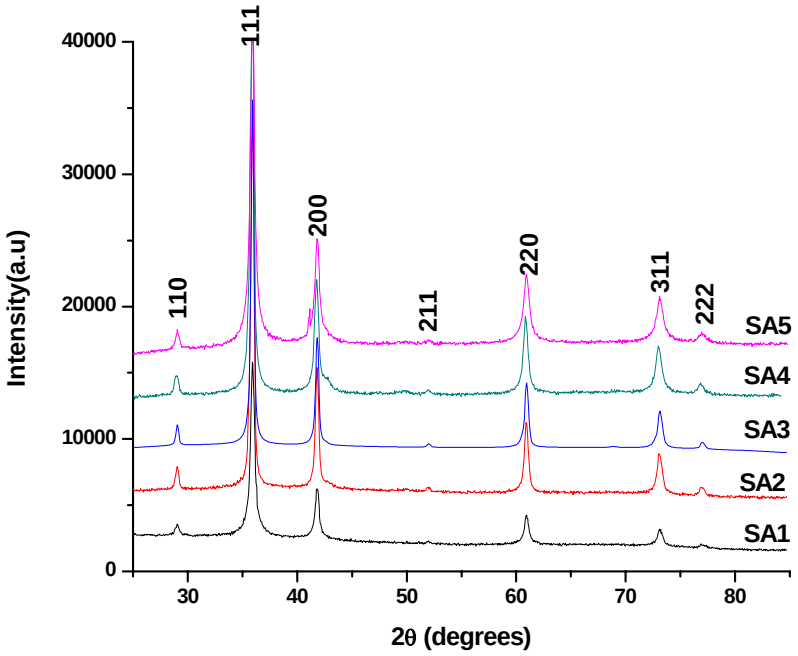

Figure 2 1. *Diffraction pattern of the SA set of specimens. For better clarity, the remaining data are not shown.*

The broadening of the line profiles decreases with the increase of ω this may indicate an increase in the size of the particles, as defects contribution to line profiles is expected to be negligible in a slow bottom-up synthesis such as the one investigated here. Quantitative microstructural information was obtained from XRD data by means of the recently developed WPPM approach [22], a physically-sound alternative to traditional Line Profile Analysis based on the Scherrer formula, Williamson-Hall or Warren-Averbach methods [21, 32, 33]. WPPM directly connects a physical model for the microstructure with the diffraction pattern, allowing an extraction of microstructure parameters without recurring to arbitrary peak shapes to fit diffraction peak profiles.

The WPPM results obtained assuming the presence of a single Cu_2O phase with a lognormal distribution of spherical domains are proposed in *Table 2.2*. The

analysis leads to the conclusions that: (i) there is no evidence of additional contributions due to line defects, and in general no contributions to line broadening other than those from the small size of the crystalline domains; (ii) mean domain sizes range between a few nanometres (SA1) to nearly 20 nm (SA3) (*see Figure 2.2*), although standard deviations change quite significantly. Apparently, there is no evident correlation between mean domain size and ω when we assume a single mode distribution.

Sample	(A) One Phase				(B) Two Phases							
	ω	<D> nm	σ nm	GoF	*k*	a_0 Å	<D> nm	ω nm	a_0 Å	<D> nm	σ nm	GoF
SA1	1.3	2.6	2.9	1.22	0.459	4.2644	17.6	8.6	4.2961	1.2	0.69	1.25
SA2	2.6	15	7.8	1.71	0.667	4.2623	25.6	11.4	4.2867	1.4	1.28	1.18
SA3	3.8	19	8.8	1.56	0.748	4.2637	34.4	5.9	4.2815	1.5	1.56	1.43
SA4	5.1	4.8	4.6	1.21	0.384	4.2602	37.5	11.7	4.2691	1.5	1.81	1.10
SA5	6.4	4.8	4.5	1.22	0.358	4.2589	41.9	4.2	4.2685	1.6	1.91	1.17

Table 2 2. *Results of WPPM on the SA set of specimens. Data are reported with significant figures only. The column report the water/surfactant ratio ω, mean domain size <D> (calculated as first moment of the size distribution), variance of the distribution σ, cell parameter a_0, scale parameter k and Goodness of Fit (GoF).*

Apart from SA1, the modelling result is not entirely satisfactory. Residuals (difference between model and data) are not completely flat and featureless, as it would be expected in case of good match. As an example, *Figure 2.3* shows some peak-like structures in the residual for specimen SA3. The problems in modelling may be due to the non-ideal conditions of the XRD measurements, for which one would need larger quantities of crystals, whereas the yield of each sample preparation was definitely too low to allow for a proper mount. However, also in consideration of the large standard deviation, the unsatisfactory modelling may originate form a more complex size distribution.

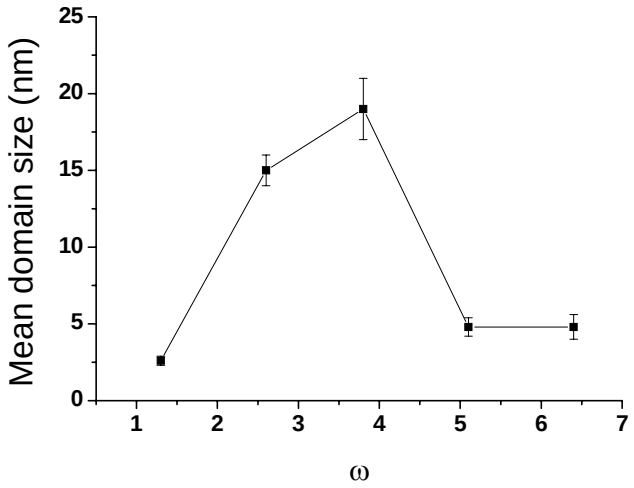

Figure 2.2 *Trend of the mean domain size (first moment of the lognormal distribution) versus ω.*

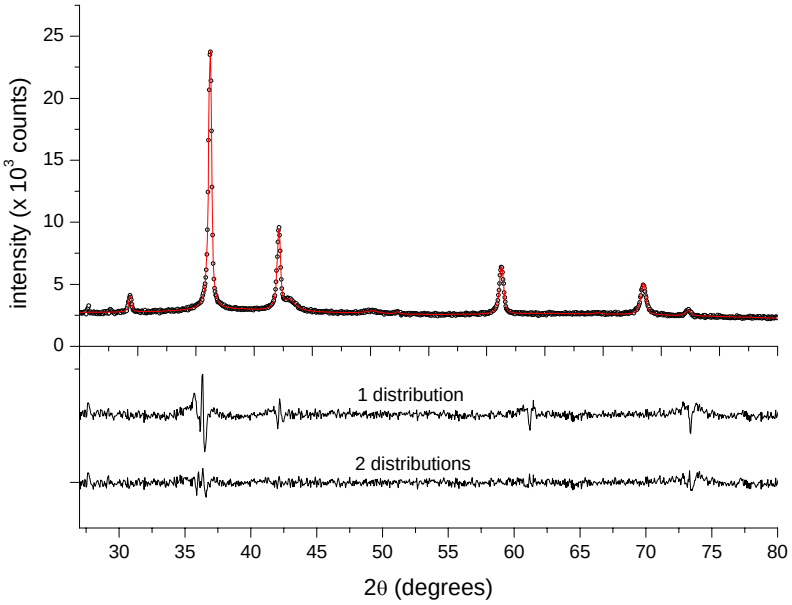

Figure 2.3. *WPPM modelling of the SA3 data using two size distributions (dots - raw data, line - model). For comparison purposes, the difference between data and model (residual)*

is proposed both for the case of 2 distributions and 1 distribution. Residuals are drawn with a x3 magnification factor to highlight differences.

WPPM was thus tested by including a second independent domain size distribution (*see Table 2.2*), considering a different unit cell parameter (as if in a second cuprite phase) to account for possible surface relaxation effects frequently observed in nanocrystalline powders [34, 35]. It is worth underlining that, in the general case, the WPPM approach considers peak intensities as free parameters. Hence, to reduce parameter correlations and to allow for a more robust modelling, relative intensities were constrained to be the same in the two fractional components, and a scale parameter (k) was refined to determine the volume fractions of the two fractional components.

Although micellar systems are usually thought to provide a single and narrow distribution of domains [36, 37], bimodal distributions (sharp XRD peaks and quite broad tails) have been observed theoretically [38] and experimentally [39]. From this point of view, the use of a method such as WPPM, which considers fine features of the diffraction pattern, is important: Scherrer formula or Williamson-Hall method, so far extensively used by the scientific community and based on the estimation of the sole line-profile breadth, easily miss the presence of small domains, related to features hidden in the tails of the diffraction peaks.

As shown by the Goodness of Fit (GoF) in *Table 2.2*, the quality of the modelling improves significantly when adding a second phase. As an example, *Figure 2.2* shows a comparison of the residuals for SA3 obtained by using single and bimodal distributions in WPPM: the improvement when using two phases is quite evident. *Figure 2.4(a)* shows the size distributions for specimen SA1, SA3 and SA5. Distributions are multiplied by crystallite volume, so that the area under each distribution is directly equal to the volume fraction.

According to the literature (*see e.g. [40, 41]*), a monomodal distribution is mostly expected from syntheses done in micellar systems. In most practical cases,

however, it is possible that a multimodal distribution is obtained, but the minority fraction is not taken into account or not thoroughly studied. For instance, a bimodal distribution has been observed in the micellar production of silver nanodisks by Maillard *et al.* [42]: the presence of large domains with a definite shape (discoidal in this case) plus a fraction of spherical nanometric domains is clear in the cited literature.

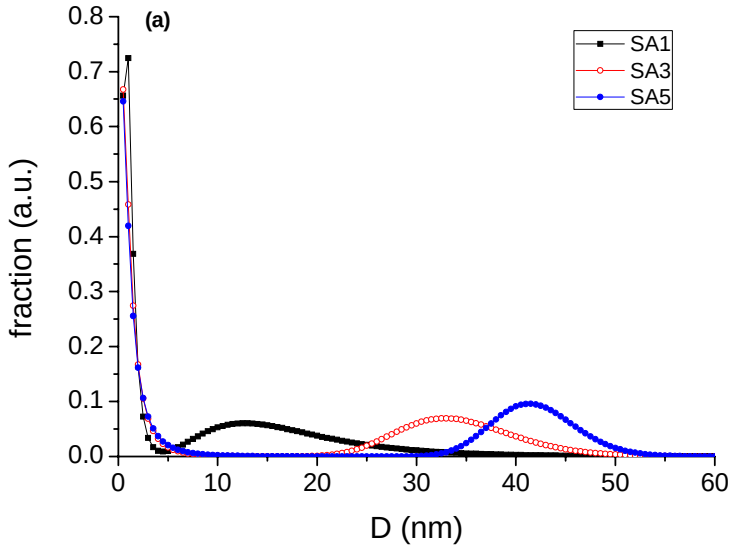

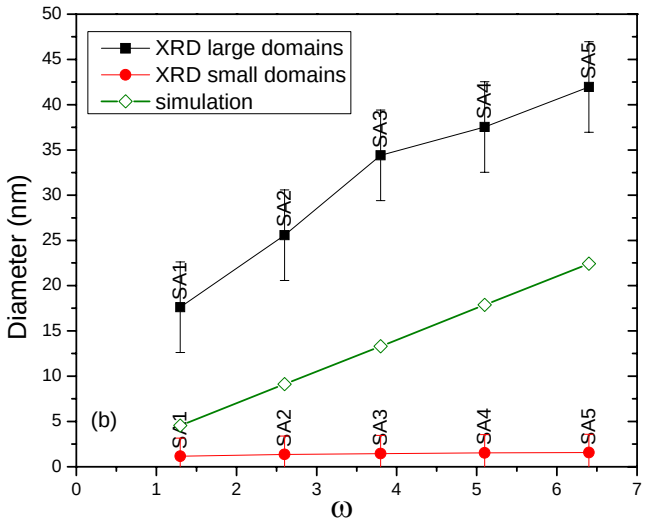

Figure 2. 4. ***(a) Bimodal particle size distribution for three representative specimens: SA1 (square), SA3 (circle) and SA5 (dot). In (b) the trends of average diameter versus ω. Diffraction data (larger domains, square; smaller domains, circle) are shown with results of the simulation (as of Eq. (3), diamond).***

For a further validation and comparison with the cited literature, the morphology of the nanocrystals was observed using Transmission and Scanning Electron Microscopy (TEM & SEM). *Figures 2.5 (a) and (b)* shows the TEM micrograph of a cluster of Cu_2O nanocrystals (specimen SA3), statistically well representing the specimen.

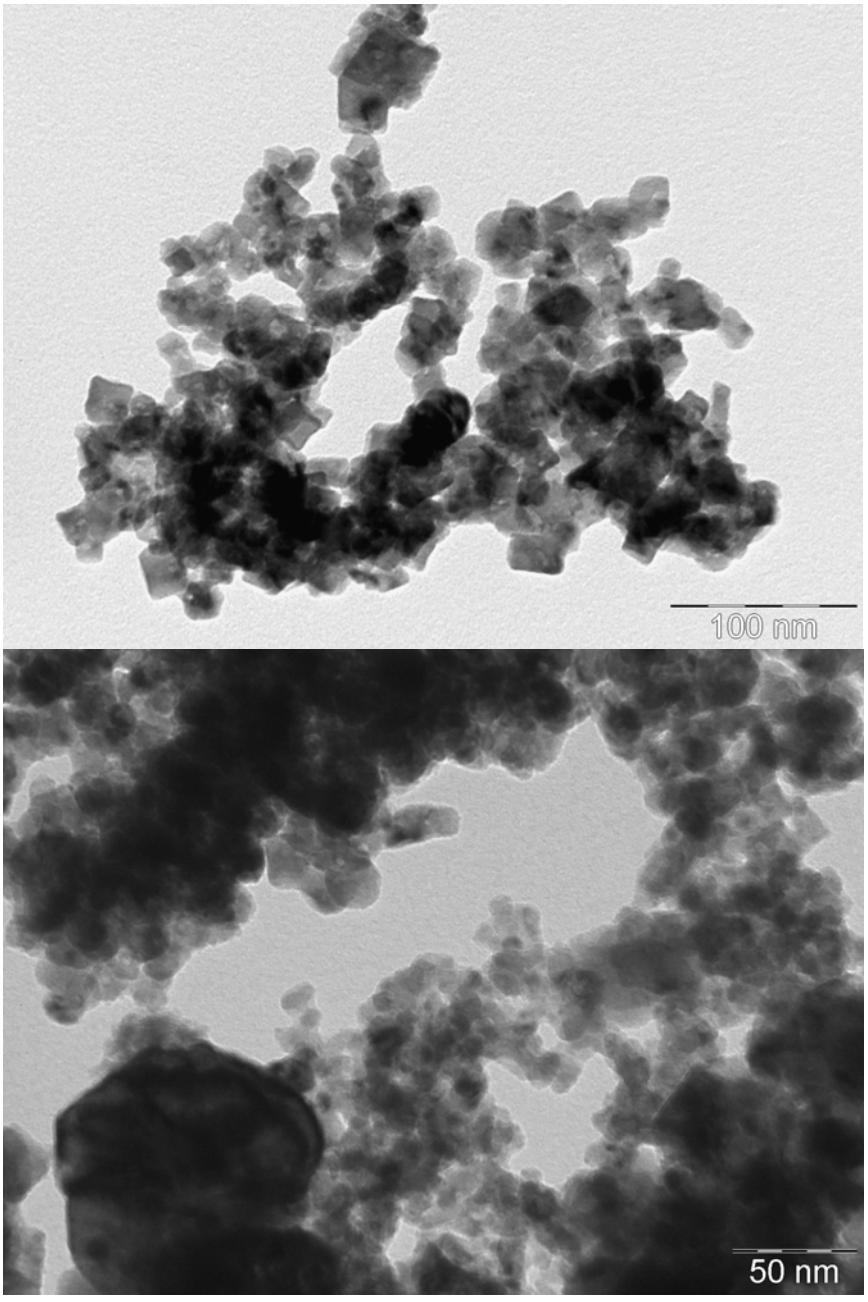

Figure 2. 5. ***TEM micrograph of sample SA3 showing the presence of both large and small domains.***

A multimodal size distribution is evident, whose features are very similar to those observed in the cited paper [42]. The particles in the powder show also a wide size distribution: the SEM micrograph proposed as an example in *Figure 2.6*, shows a high degree of aggregation and the simultaneous presence of large and small particles in the system, particles that are large than the expected micelle size (a few nm).

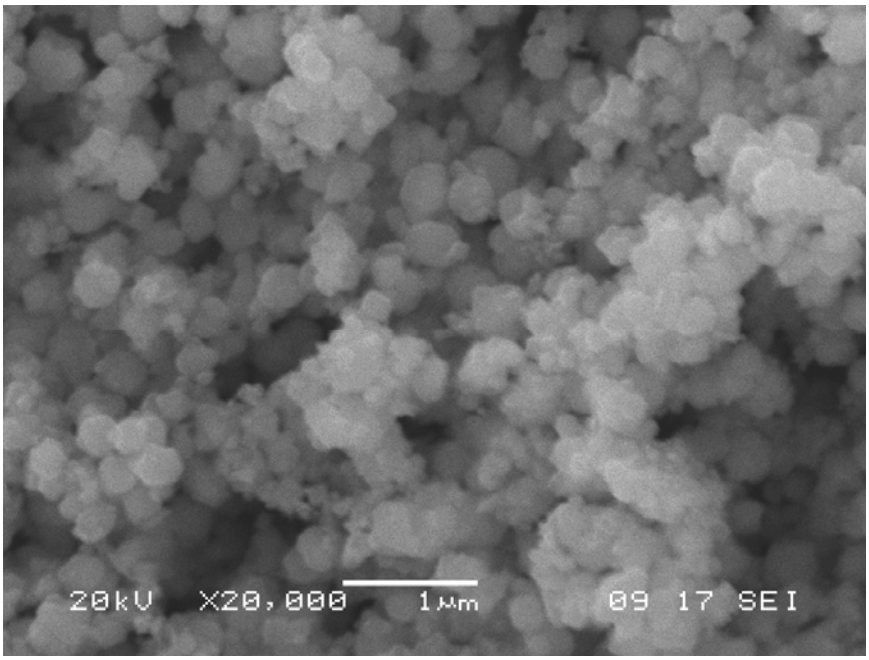

Figure 2. 6. ***SEM micrograph of sample SA3 showing the presence of both large and small particles.***

The growth above the spherical micelle size limit can be attributed to an interplay between micelles in the microemulsion. In fact, in a dynamical condition like that of a microemulsion, micelles will not be static isolated objects, but will move and eventually collide [41, 43]. Collisions lead to intermicellar exchange and therefore growth of the nanoparticles through mechanisms involving autocatalysis and ripening [41, 43]. When an empty micelle impinges a filled one, the reactant

can be transferred and support the growth of the existing particle (autocatalysis). The larger the particle, the larger the area available for further growth. On the other hand, collisions between filled micelles can lead to growth of the larger particle due to phenomena such as Ostwald ripening, that would again favour larger particles with respect to smaller ones [41, 43]. The incidence of those phenomena is related to the rate of micelle encounter and to the rigidity of the surfactant protective layer. The more rigid the layer, the lower the exchange rate and, consequently, the lower the particle growth. Conversely, a less rigid layer would allow the micelles to be easily deformed: the exchange can then occur in completely filled micelles, allowing growth above the micelle size limit.

Ultrasonication employed to evenly distribute the reducing agent in the micelles may be responsible for the presence of the small particles: the excess energy introduced in the system by ultrasonication may promote an initial formation of an excess of nuclei that remained till the point of emulsion breaking [44]. The absence of ultrasonication, on the other hand, would not allow a uniform nucleation in the system, whereas an excess ultrasonication may aid in weakening the surfactant film rigidity, thus promoting an excessive growth.

It is to exclude that growth occurred after the microemulsion was broken: breaking the surface tension using acetone just allows for precipitation of the particles under the influence of gravity. The surfactant is still protecting the surfaces at this stage: the subsequent removal of the organic phase using ethanol and water, also removes the possible reactants remained in the system, thus effectively limiting the possibility of further growth [45]. At this stage we would expect to see the formation of the nanoparticles aggregates observed under the TEM, more than the coalescence of existing domains.

The fraction of large crystal versus ω is shown in *Table 2.2:* SA3 has a larger fraction of large crystals (74.8%) with respect to the other samples. *Figure 2.2(b)* illustrates the trend of the average domain size of the two size distributions:

the average size of the larger fraction clearly increases with increasing ω. An increase in the water content reduces the interaction between the surfactant headgroups in the micelles and further weakens the surfactant layer rigidity. This shifts the nucleation mechanism from intramicellar to intermicellar, with a tendency to lower the nucleation rate, which favours an overall growth of larger particles [46].

Just for completeness, we report that the unit cell parameter of the two distributions is slightly decreasing with ω (*cf. Table 2.2*): this decrease is compatible with a surface relaxation effect, albeit a certain degree of correlation between cell parameter and specimen displacement (due to the non ideal specimen mount in the powder diffractometer) exists.

2.3.3 Modelling of the microemulsion system

In order to understand the correlation between the observed domain size (both in terms of sizes and appearance of a bimodal distribution), a deeper understanding of the micellar system and the modelling of its features are necessary.

2.3.3.1 Surfactant and Colloidal Science

Surfactants are low to moderate molecular weight compounds which modify the physico-chemical properties surfaces or interfaces of the media in which they are contained. Because of these features, they are referred to as Surface-active agents.

A surfactant molecule is made up of a hydrophobic part (non polar “tail”), which is generally readily soluble in oil but sparingly soluble or insoluble in water, and a hydrophilic (or polar “head”) part, which is sparingly soluble or insoluble in

oil but readily soluble in water. *Figure 2.7* shows a schematic representation of a surfactant molecule.

Due to the coexistence of polarities (polar head and non polar tail) in the molecule, surfactants are also referred to as amphiphilic compounds or amphiphiles. The amphiphilic nature of surfactants makes it possible to stabilize an immiscible water-oil mixture by reducing the interfacial tension between the two phases.

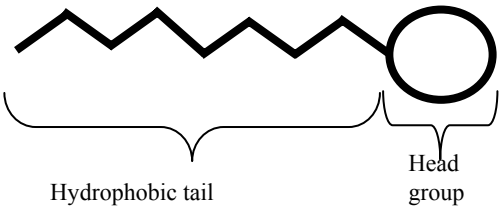

Figure 2. 7: ***Schematic representation of a surfactant molecule.***

Short hydrocarbon (hydrophobic) chain surfactants are soluble in water while long chain surfactants are insoluble. The ability of surfactants to modify the physico-chemical properties of emulsions or colloidal dispersions make them very important in industrial applications such as asphalt emulsions, the paper industry laundering, industrial hard surface cleaning, inhibitor of corrosion, enhanced of oil recovery, personal care (cosmetics) products and coal transport [47, 48]. Owing to their varied applications, it is important to identify the specific type and/or class of surfactant for a specific application.

Surfactants can be classified based on their physical properties or functionalities. Accordingly, the following are some classification based on the nature of charge present on the hydrophilic group:

- **Ionic (anionic and cationic) surfactant:** Their solubilisation in water involves the ionization of the polar head. The charged polar head reacts with

ions in the solution. Sub-groups of this class are: *anionic,* which exhibits a negative charge, like as alkylbenzenesulfonate ($RC_6H_4SO_3^-Na^+$), *cationic,* which bears positive charge, for example a salts of a long-chain amine, like as quaternary ammonium chloride ($RN(CH_3)_3^+Cl^-$) and *zwitterionic (or amphoteric),* which carries a combination of the anion and cation characters. Examples are the derivatives of phospholipids or amino-acids as sulfobetaine ($RN^-(CH_3)_2CH_2CH_2SO_3^-$). Their charge and property depend on the pH of the system which determines the dominating character of the molecule: anion with basic pH, cation with acid pH, and at their isoelectric point. They usually carry the two functions simultaneously.

- **<u>Nonionic Surfactants</u>:** They contain non-charged polar groups of which the affinity for water is due to the strong dipole-dipole interactions resulting from the hydrogen bonds. The function of this class of surfactant is modulated by the number of EO units which comprises the hydrophilic (polar) head and the length of its hydrophobic (hydrocarbon) tail. Brij30® (Polyoxyethylene 4 Lauryl Ether-$(C_2H_4O)_nC_{12}H_{26}O$, n≈4) is an example of this class: the structure of Brij30® is shown in *Figure 2.8*.

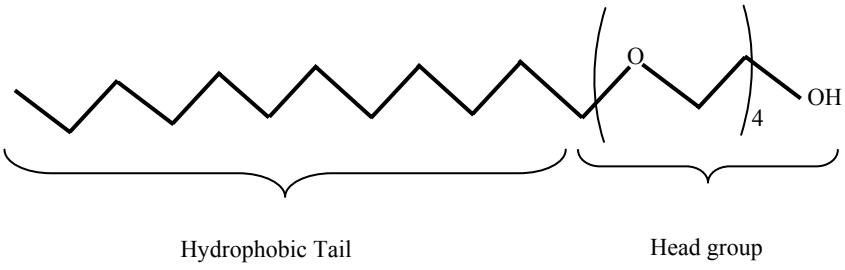

Figure 2. 8. ***Structure of the nonionic Brij 30 surfactant.***

Research interest has been heightened in the use of non-ionic surfactants for reverse micelles for nanoparticles growth applications especially due to the unfavourable interactions between ionic reactants and surfactant groups.

Among the many unique properties that nonionic surfactants have over those of ionic surfactants with comparable hydrophobic groups:

- low critical micelle concentrations [49, 50]
- high efficiency in reducing surface tension [51],
- better solubilising properties, which make them potentially useful in a wide variety of industrial applications,
- a significantly lower sensitivity to the presence of electrolytes in the system,
- lessened effect of solution pH [52] and
- synthetic flexibility of being able to design the required degree of solubility into the molecule by careful control of the size of the hydrophilic group.

A unique advantage of the nonionic surfactants is that their use does not involve the introduction of potentially undesirable counterions; moreover, the ability to alter the size of the hydrophilic oxyethylene groups and the hydrophobic alkyl groups provides additional flexibility in surfactant selections [53].

Surfactants in solution preferentially accumulate at the solution-gas, or solution-liquid, or solution-solid interface. At the interface, the molecules arrange themselves such that the hydrophilic heads are in contact with the aqueous phase whiles the hydrophobic tails are in contact with the non polar phase. This phenomenon aids micellar microemulsions formation [54].

Depending on the applications to which the surfactant will be used, factors such as the Hydrophilic - Lipophilic Balance (HLB), micellisation mechanism and the Critical Micelle Concentration (CMC) are of considerable importance.

2.3.3.2 Hydrophile- Lipophile Balance

The hydrophilic-lipophilic balance number is an empirical expression for the relationship between the hydrophilic and hydrophobic groups of a surfactant. This HLB value provides a semi-quantitative description of the effectiveness of surfactants with respect to emulsification of oil-water systems. This scale introduced by Griffin [55, 56] is used to characterize nonionic surfactants using oxyethylene oligomer as hydrophilic group. The HLB number for nonionic surfactants can be calculated through the following equation:

$$HLB = 20\left(1 - M_{hl}/M_T\right) \qquad (0.8)$$

where M_{hl} is the formula weight of the Hydrocarbon (hydrophobic) chain of the molecule and M_T is the total formula weight of the surfactant molecule. The ranges of performance of surfactants based on their HLB values are illustrated in *Table 2.3*.

HLB Value	**Property**
>10	Water soluble
<10	Oil soluble
4-8	Antifoaming agent
7-11	W/O-Emulsifier
11-14	Wetting agent
12-15	Detergent
12-16	O/W-Emulsifier
16-20	Stabilizer

Table 2. 3. ***Hydrophilic-Lipophilic Balance (HLB)***

2.3.3.3 Micellisation

Surfactants molecules dispersed in water, will preferentially move (adsorb) towards the air-water interface. This phenomenon at interfaces depends on the surfactant concentration. Formation of surfactant aggregates called micelles

(micellisation) initiates as the surfactant molecules start to occupy the bulk of the solution when saturation of the interface takes place due to increasing solute concentration.

The minimum concentration of surfactants necessary to saturate the interface and start the formation of micelles is known as critical micelle concentration (CMC), which primarily depends on several factors like as hydrophobic group, hydrophilic group, and temperature, functional groups in the structure, salts and type organic solvents used [57].

For nonionic surfactants, micelles are formed below a temperature known as the turbidity (or cloud) point, according to the concentration of the solution. For ionic surfactants, formation of micelles only occurs above a minimum temperature known as the Krafft temperature.

In fact the critical micelle concentration and the Krafft point (KP) both define the monomer activity with regard to aggregation and formation of micelles. Mathematically, the variation of the critical micelle concentration with the surfactant molecular structure is given by:

$$\log(cmc) = A - Bn_C \qquad (0.9)$$

where A and B are constants and n_c is the number of hydrocarbon groups in the alkyl chain.

The correlation between the Krafft point and the CMC is given by:

$$KP = -\left(k_C / B\log(cmc) + k_C A - k_i\right) \qquad (0.10)$$

A phase diagram (curve) relating surfactant concentration to temperature is shown in *Figure 2.9* where the point (T_K; C) is the Krafft temperature associated with the corresponding surfactant concentration.

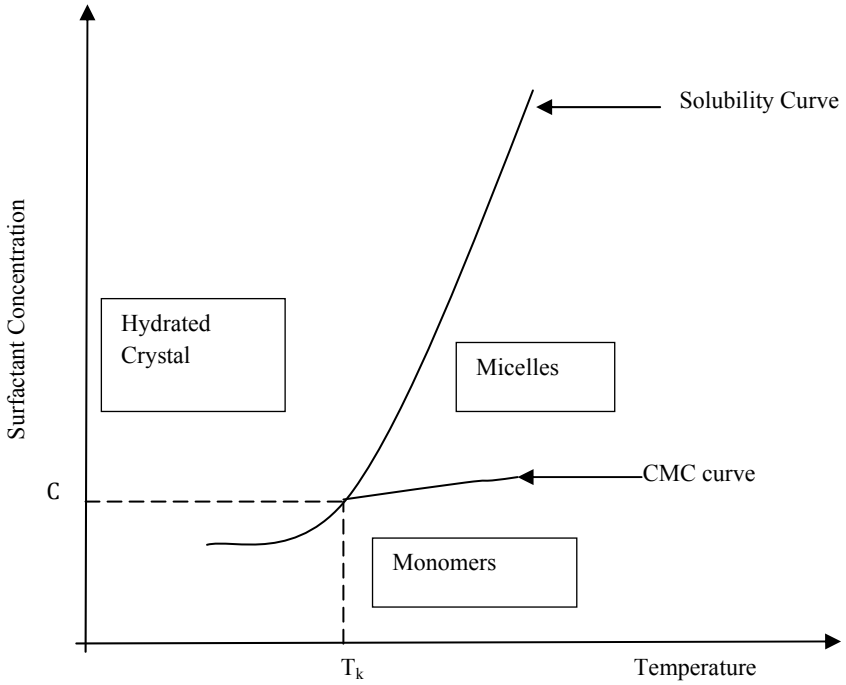

Figure 2. 9. ***Phase diagram for an ionic surfactant in aqueous solution.***

A phase diagram of a nonionic surfactant in water is shown in *Figure 2.10*, in which for each concentration, a turbidity temperature is defined. The point (C; T_c) corresponds to the critical micelle concentration and the critical turbidity temperature. Above the turbidity line (solid line) a two-phase system is obtained while below the turbidity line at sufficiently low temperatures, a clear, single phase system is formed.

Some of the techniques used to determine CMC include surface tension, turbidity, self diffusion, conductivity, osmotic, UV-Vis-IR spectroscopy, fluorescence spectroscopy, nuclear magnetic resonance spectroscopy and solubilisation, where a plot is made of the measurement parameter as a function of the logarithm of the surfactant concentration. The breakpoint in the plot represents

the CMC. Table 2.4 shows typical CMC values for low electrolyte surfactant concentrations at room temperature.

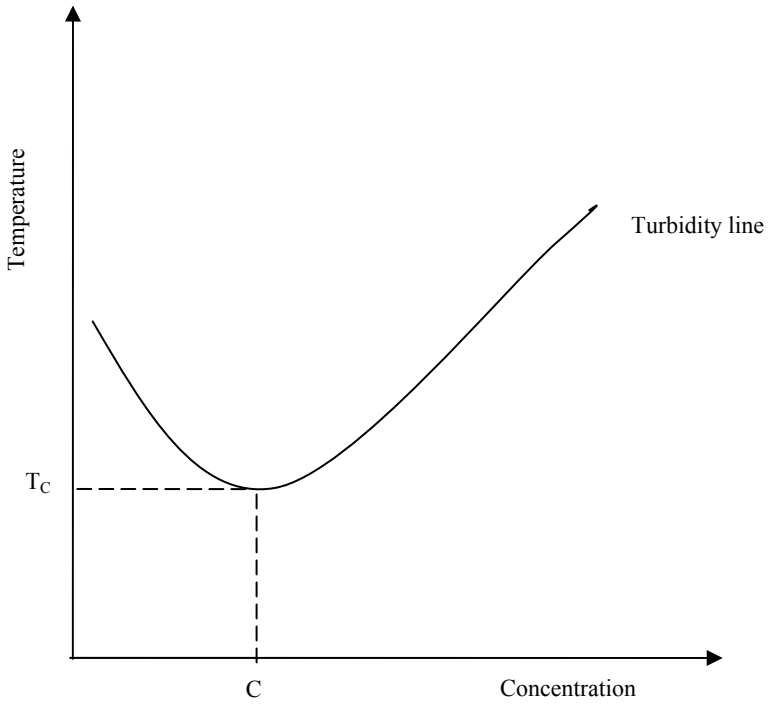

Figure 2. 10. ***Phase diagram of a nonionic surfactant in aqueous solution.***

Surfactant	**CMC value**
Nonionic	10^{-5}-10^{-4} M
Amphoteric	10^{-3}-10^{-1} M
Anionic	10^{-3}-10^{-2} M
Cationic	10^{-3}-10^{-2} M

Table 2. 4 ***Critical Micelle Concentration values of common surfactants***

It is worth noting that, at concentrations above the CMC, surfactant molecules continuously leave and return to the solution-interface forming a

constant dynamic exchange cycle between the interface and the solution. The polarity of the solvent determines how the molecules will be arranged in the solution after the CMC is reached. According to Tanford [58], hydrophobic effects in an aqueous medium, are responsible for the micellisation, when there is an increase in the overall entropy of the system. This is a result of the minimisation of the interactions between the surfactant's nonpolar tails and the solvent. Hence, the hydrophobic (hydrocarbon) tails of the surfactant molecules are directed towards the core of the micelle, in order to avoid contact with water, whereas the polar head-groups are oriented towards the aqueous medium, leading to a normal micelle formation.

In nonpolar solvents (oils), no hydrophobic effects are present, and the micellisation process is driven by enthalpy changes originated from Coulombic interactions between the polar head-groups of the surfactants. In this case, there is a decrease in the overall entropy of the system, which allows the nonpolar chains to be oriented in apolar dispersing medium whereas the polar head-groups occupy the core of the aggregate, thus forming reversed micelles.

The number of molecules present in each micelle defines the aggregation number for the surfactant in solution, as well as the type of micelle formed. Generally, micelles with a low aggregation number tend to present a reasonably spherical form [59]. However, at higher concentrations, the aggregation number for many amphiphiles increases and the micelles tend to acquire a disk-like or rod-like configuration, or evolve to hexagonal or lamellar aggregates, and even vesicles [60]. A key feature that distinguishes ionic and nonionic surfactants is in the difference in their head-groups response to solubility temperatures in water.

2.3.3.4. The Geometric Packing Parameter

When dissolved at concentrations above their CMCs, surfactant molecules tend to assume specific configurations that are directly related to their shape and geometry.

This is complementary to the concept of HLB, introduced above and useful to provide a preliminary indication to the final use of the surfactants. However, the way by which surfactant structure controls the orientation of the molecules at interfaces is more quantitatively expressed by the dimensionless *geometric packing parameter* (P_c) [60]. This parameter it is defined by equation (0.11), where v is the volume of the hydrocarbon chain which is assumed to be fluid and incompressible, a_0 is the effective head-group area and L_c is the effective (critical) hydrocarbon chain length, chiefly between 80% and 90% of the fully extended hydrocarbon chain.

$$P_C = v \Big/ \left(a_0 L_C \right) \tag{0.11}$$

The chain length is a semi-empirical cut-off parameter which sets a limit on how far the chains can extend to still remain fluid since extensions beyond this length is not allowed due to a sharp rise in the interaction energy.

The packing parameter is essentially a measure of the ratio between the effective areas occupied by the hydrophobic (v/L_c) and hydrophilic (a_o) parts of the surfactant.

Depending on the surfactant structure, P_c assumes specific values and the packing constraints in the medium allow for the formation of a preferred aggregate shape configuration such as spherical micelles, non spherical micelles, vesicles or bilayers or inverted micelles. Each of these structures corresponds to the minimum size aggregates in which the hydrophobic parts will have a minimum free energy. For example, surfactants with large P_c (large hydrocarbon chain volume, for instance) prefer to aggregate as reversed micelles in oil instead of forming normal micelles in water.

For surfactant molecules to form spherical micelles, their optimal surface area “a”, must be sufficiently large and their hydrocarbon chain volume sufficiently small so that the radius of the micelle R will not exceed the critical chain length L_c

[61]. When we consider a spherical micelle, its mean aggregation number M and radius R, relates to the surfactant head group area a_0 by the relation:

$$M = \frac{4\pi R^2}{a_O} = \frac{4\pi R^3}{3v} \tag{0.12}$$

$$R = 3v/a_O \tag{0.13}$$

When $P_c \leq 1/3$ spherical micelles form, whereas spherical reverse micelles are formed when $P_c > 2$. Cylindrical micelles are formed when $1/3 < P_c < 1/2$, while bilayers, discs or vesicles are formed when $½ < P_c < 1$ [61].

The geometric packing parameter, however, may be affected by a number of system parameters, which causes changes in the system configuration. It increases with chain branching, ionic strength (for ionic surfactants) and temperature (primarily for nonionic surfactants). On the other hand, P_c decreases as the size of the head-group increases or when surfactants with shorter chain length are added to the system.

The geometric packing parameter can be related to the type of microemulsion by considering that;

- if $a_o > v/L_c$, then an oil-in-water microemulsion forms
- if $a_o < v/L_c$, then a water-in-oil microemulsion forms
- if $a_o \approx v/L_c$, then a middle-phase microemulsion is the preferred structure.

Although micelles have various shapes, they are usually spherical in shape and typically contain 50-200 surfactant monomers. As already discussed, the size and shape of micelles are primarily determined by geometric and energetic factors. It is worth stating that, since reverse micelles are useful nanoreactors for the synthesis of nanoparticles, further mention of micelles in this thesis will refer specifically to spherical reverse micelles.

2.3.3.5. Microemulsions

Microemulsions are thermodynamically stable, transparent, isotropic liquid mixtures of oil (usually hydrocarbon/olefins), water and surfactants [62]. The surfactant may be pure, a mixture, or in combination with a cosurfactant such as a medium-chain alcohol (e.g. ethanol, butanol, pentanol). These homogeneous systems, which are all fluids of low viscosity, can be prepared over a wide range of surfactant concentrations and oil to water ratios.

Microemulsions have particular properties that allow their exploitation in many commercial and industrial applications. Their high stability, low interfacial tension at low surfactant concentration, ability to stabilise large amounts of two immiscible liquids in a single macroscopically homogeneous phase, and large interfacial area between the microheterogeneous phases are basic properties that are exploited in the design of such applications.

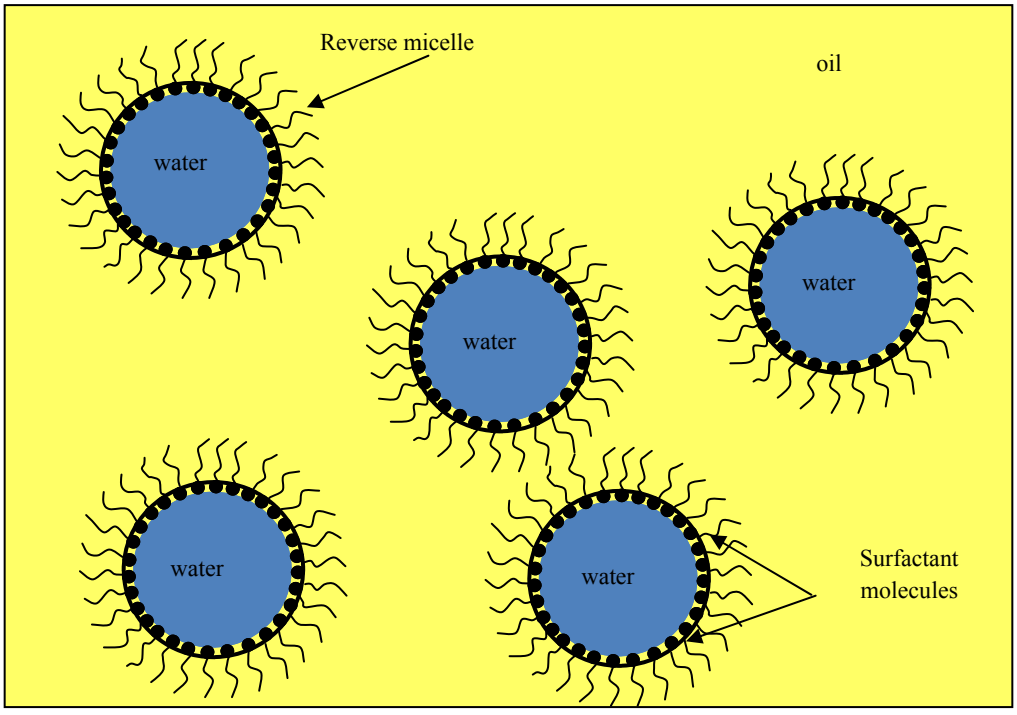

Figure 2. 11 ***Structure of water in oil microemulsion.***

The main idea behind this technique is that by appropriate control of the synthesis parameters one can use these nanoreactors to produce tailored products down to a nanoscale level with new and special properties.

In oil-rich microemulsions, water is solubilised as small droplets (≈ 2 – 50 nm) surrounded by a membrane of surfactant (and cosurfactants) molecules. These structures are known as water-in-oil (w/o) microemulsions, where the lypophilic parts of the surfactants are directed towards the oil phase and their polar head-groups are directed towards the water phase. In *Figure 2.11,* an idealized schematic representation of this type of microemulsion is shown.

2.3.3.6. Microemulsion Phase Diagrams

A ternary phase diagram – under the form of a triangle - is an easy way to graphically represent microemulsion systems. Sections at given temperature and pressure are usually provided. The vertices of the triangle correspond to pure components, and each of its sides represents to possible compositions of binary mixtures, including micelles and reversed micelles. Any point inside the triangle represents a ternary mixture in specific proportions for each component. Figure 2.12 shows a hypothetical ternary phase diagram for an ideal three-component system, in which some possible aggregates are shown. These aggregates include micelles (o/w), inverse micelles (w/o), liquid crystals (Lamellar) and irregular structures in the bicontinuous regions.

At high water concentrations, microemulsions consist of small oil droplets dispersed in water (o/w microemulsion), while at lower water concentrations the system comprises water droplets dispersed in oil (w/o microemulsions) which is of particular interest in this research study.

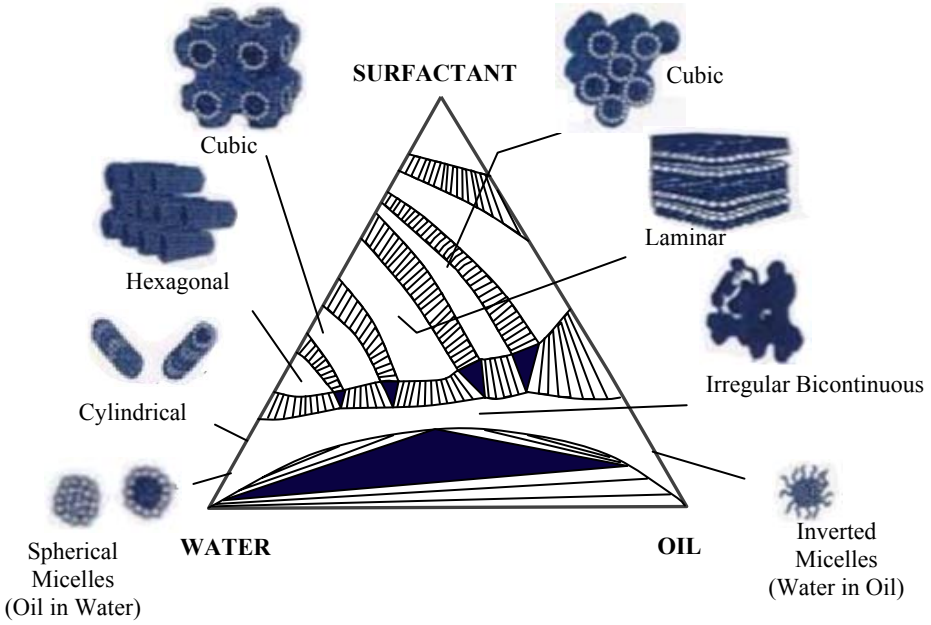

Figure 2. 12.***Ternary phase diagram of microemulsions [63].***

In each phase, the oil and water droplets are separated by a surfactant-rich film whose molecules may form a monolayer at the interface between the oil and water, with the hydrophobic tails of the surfactant molecules dissolved in the oil phase and the hydrophilic head groups in the aqueous phase. The interfacial tension between the two phases is usually extremely low due to the surfactant. Hence, a reverse micellar solution is referred to as w/o microemulsion while the reverse micelles are referred to as the droplets. The aqueous phase usually contains salt(s) and/or other constituents.

The water–surfactant molar ratio (ω) usually determines the size of reverse micelles which are on the nanometer scale. However, the droplets are kinetically unstable (*Brownian motion*) and a dynamic exchange process normally occurs between colliding droplets. This phenomenon is discussed at the section on nanoparticles formation in reverse micellar systems.

In fact, different types of microemulsion phases can coexist under thermodynamic equilibrium conditions with bulk aqueous or oil phase. These types of microemulsions can be classified based on the Winsor equilibria model [64] which identifies four classical types of phase diagrams in a water - oil - amphiphile mixture as:

- Winsor I: An o/w microemulsion coexists with an excess oil phase. No surfactant aggregates are found in the oil phase, but only a small concentration of surfactant monomer may be present.
- Winsor II: A w/o microemulsion coexists with an excess water phase which is almost pure (a small concentration of surfactant monomer may be present).
- Winsor III: This corresponds to the equilibrium between three phases: a middle microemulsified phase, either of the bicontinuous or lamellar type, containing oil, water and most of the surfactant, in contact with excess oil and water phases.
- Winsor IV: This is a single-phase system, with surfactant, water, and oil homogeneously mixed.

A schematic representation *(Figure 2.12)* of the Winsor classification is shown below.

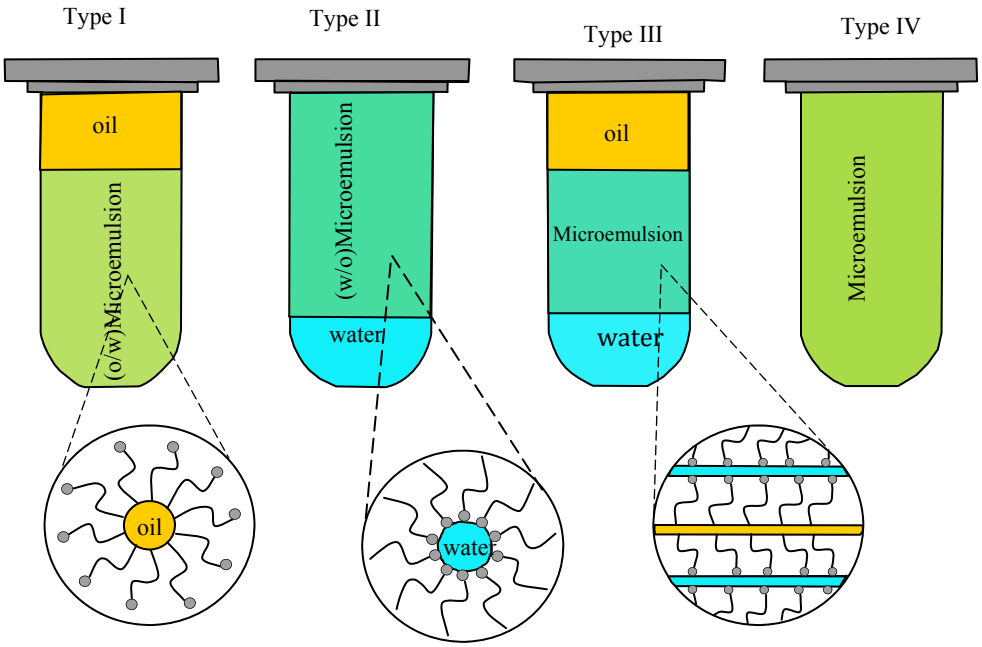

Figure 2. 13. ***Winsor's classification of microemulsion systems.***

More complicated systems are often used in practical applications, but as the complexity increases, so does the difficulty of representing the systems in simple graphic form. Four-component systems require a three dimensional representation. To overcome this problem, two components are usually considered as one, according to their weight or volume ratio, thus generating a single pseudo-component. Two types of fixed ratios are usually employed: the [water]/[surfactant] ratio and the [cosurfactant]/[surfactant] ratio. The former is more used in structural studies of aggregated systems, whiles the latter is more commonly used when characterising the phase behaviour of microemulsions.

2.3.3.7 Synthesis of inorganic nanocrystals in reverse micelle systems

Among the proposed synthesis routes, water-in-oil (W/O) microemulsions are the most promising as they provide nanoreactors where size and morphology of

nanoparticles can be well controlled [65-69]. The technique involves two distinct mixing approaches: single and double microemulsion.

The single microemulsion approach, which was used in this thesis work, involves sequential addition of reactants and reducing agents to the same microemulsion allowing for *intramicellar* nucleation and particle growth. This approach requires the use of lesser microemulsion volumes but produces more particles.

Double microemulsion involves mixing two equal volumes of microemulsion one containing reactants and the other containing the reducing agent. Quantity of final particles obtained is low.

In this section, an overview of the controlled synthesis of inorganic nanostructures in reverse micellar system is given. Particle formation mechanisms are explained with particular emphasis on formation in single microemulsion scheme which is of interest to this thesis work.

It is worth stating that in this thesis, nanocrystals and nanoparticles are synonymous to nanocrystalline structures. Moreover, particle shapes, sizes, and size distribution of the structures formed in micelles are refer to nanocrystallites (domains) shape, crystallite size and crystallite size distribution respectively. As most of the microstructure analysis are based on x-ray diffraction techniques, discussion, on the final products are based on the crystalline domains. Particle agglomeration are not observed in XRD but accounted for herein using electron microscopy

Spectroscopic studies [70, 71] have shown that three kinds of water layers *(Figure 2.13)* may exist at the interior of a reverse micelle in a microemulsion:

- the core layer located in the interior of the “water pool” which has properties as bulk water.

- The intermediate layer consisting of "trapped" water molecules that can exchange their state with the interfacial layer during the formation of monomers or dimers.
- The interfacial layer consist of "bound" water molecules which directly interacts with the polar head groups of the surfactant molecules

It is worth noting that the quantity of water in the micelles usually influences the size of the reverse micelles. Depending on the size of reverse micelles, available water may have significantly different solvent properties, ranging from highly structured interiors with little molecular mobility [72, 73] to free water cores that show approximately the same characteristics as solvents in bulk water. Moreover, due to surface induced structuring, the behaviour of the water molecules confined in the nano-size space differs significantly from that of the bulk water. The chemical reactions take place in the water pools of the reverse micelles.

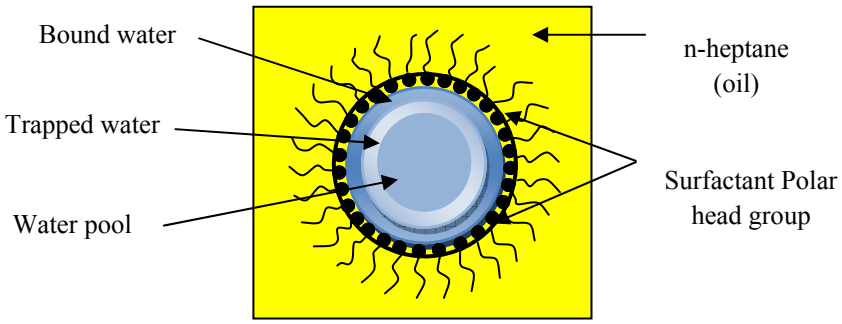

Figure 2. 14 ***Schematic representation of spherical reverse micelle.***

The dynamics of chemical reactions undertaken within micellar aggregates (reverse micelles) include the effects of Brownian diffusion of reverse micelles, droplet collision, complete or partial merging of micelles, diffusion of reactants and their chemical reaction, as well as fragmentation of transient dimers or multimers [74] , ranging from the order of magnitude of nanoseconds for diffusion

controlled intermicellar reaction to an order of milliseconds for intermicellar exchange of reactants [75]. Further explanation of the above effects has been elucidated in the nanoparticle formation mechanism.

Micelle formation is influenced by both kinetic and thermodynamics factors. While the formation of large micelles is thermodynamically favoured, many small micelles formation is kinetically favoured (i.e., they nucleate more easily). Hence, kinetically, it is easier to nucleate many small micelles than large ones. However, small micelles have a larger surface area (of surfactant) to volume (of water) ratio than large micelles. Large micelles, with their greater volume to surface area ratio, represent a lower energy state. Thus, many small micelles will attain a lower energy state if transformed into large micelles. For these reasons, the molar ratio of water to surfactant (ω) could play an important role in determining the size of reverse micelles and was therefore investigated in this thesis work.

In the area of reverse-micellar synthesis of nanoparticles, a picturesque representation of nanocrystallites formation inside "nano-reactors" (i.e. "water pools") of reverse micelles indicates that in general, the size of the final particle (crystallite) is equal to the size of the micelles that encapsulated and limited the growth of the individual crystallization nuclei.

This idea can be considered as an oversimplification, since in a number of cases no correlation has been obtained between final particle sizes and sizes of the reverse micelles [76, 77].

The size of the micellar units of the system can be considered as dependent not upon any single internal variable, but on the complex interactions that are conditional for their existence.

The correlation between morphology of the surfactant aggregates and the resulting particle structure in most surfactant-mediated nanoparticles syntheses techniques, is a more complex phenomenon (than simply relating the average size and shape of the micelles to size and shapes of the precipitated particles) and is

affected by almost irreducible conditions that exist in the local microenvironments surrounding the growing particles [78]. Some of the experimental factors that influence the local environments of the particles include concentration of the reactants, temperature, chemical composition, pH and ionic strength of electrolytes.

The interaction among the aggregates is generally considered as the most important factor that influences the morphology and the properties of the final reaction products [75].

Heinse, has shown that slight changes in micellar dispersity towards wider polydisperse distributions is capable of triggering the processes of Ostwald ripening of particles that result in complete phase segregation [79]. The dynamics of solvation effects can drastically change with an interfacial distance, which may prove to be a significant effect in the cases of chemical reactions performed within micellar aggregates. These factors are discussed in the section on particles formation in reverse micelle microemulsions.

2.3.3.8 Nanoparticles (crystallites) formation mechanism

The chemical reaction leading to formation of nanocrystallites/nanoparticles in single microemulsions can be activated by directly adding one of the reactants (e.g. the reducing agent) in the form of a solid (eg. $NaBH_4$), liquid (eg. N_2H_2) or gas (e.g. NH_3) or temperature (*see chapter 4*) to the microemulsion containing the other reactants. In this thesis work, the latter approach was employed in the synthesis of Cu_2O nanocrystals.

In a microemulsion containing all the reactants the chemical reaction can be initiated by means of temperature, ultrasonication, microwave radiation, and pulse radiolysis. Temperature, as it can be seen e.g. in the synthesis of CuO (*see chapter 4*), has a strong influence on the type and morphology of the final product.

The reaction takes place inside the nanodroplets, and is followed by nucleation, growth, ripening, and coagulation of primary particles, resulting in the

formation of the final nanoparticles surrounded by water and/or stabilized by surfactants.

In the microemulsion, the reverse micelles usually move by means of Brownian motion and can rapidly (in millisecond) exchange their water contents through collision, fusion and fission of dimer molecules. The dynamics of intermicellar exchange can be considered thorough a second-order chemical rate constant (k_{ex}), expressed in terms of the droplet concentration in the continuous oil medium. The fission rate constant (k_{fiss}) of fused dimers can be considered as a first-order reaction. The mechanism of nanoparticle formation in reverse micelles via intermicellar exchange is shown in *Figure 2.14*.

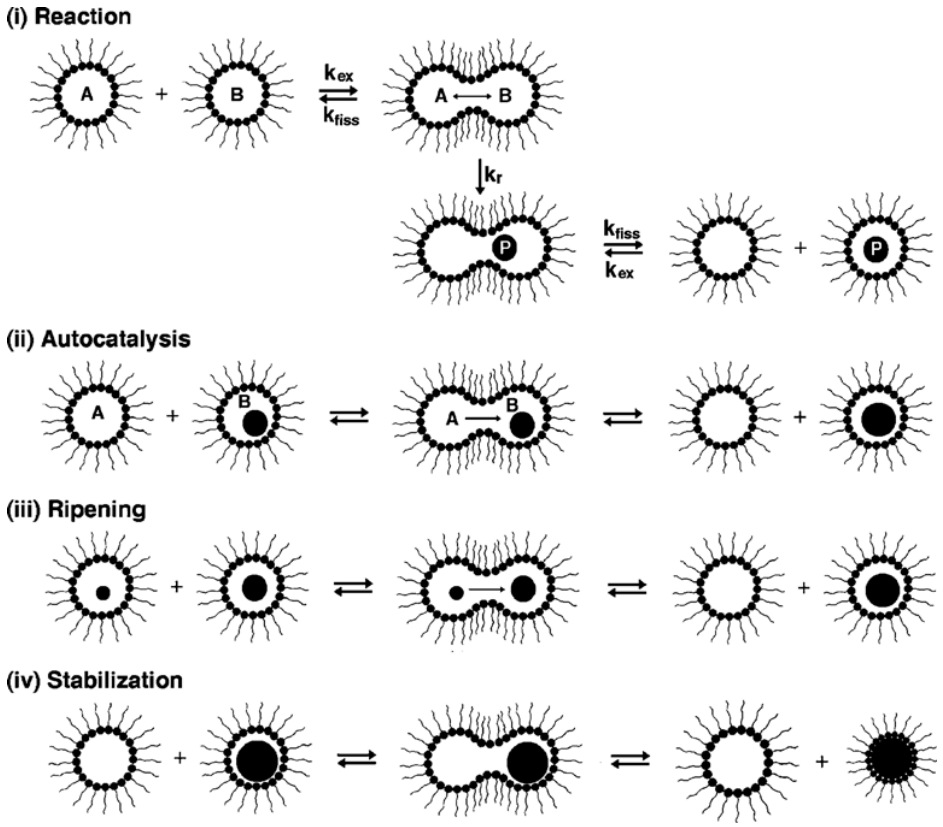

Figure 2. 15. ***Mechanisms of nanoparticle formation in reverse micelles via intermicellar exchange [67].***

For slow reactions, particle formation is dependent on the statistical distribution of the reacting species among the reverse micelles. This negatively impacts the ability to control particle size. In the single microemulsions technique, the role of *intramicellar* nucleation is promoted while that of intermicellar nucleation can be minimized. It is worth noting that, during the reaction period in the reverse micelles, many droplets could contain reactants and products at the same time. For fast reactions, particles (products) formation is determined by intramicellar and/or intermicellar nucleation and growth. When the particles are formed, their size and polydispersity are controlled by reaction kinetics, intramicellar nucleation and growth or intermicellar nucleation and growth as well as particle aggregation. The mechanism of nanocrystallites formation (*see Figure 2.14*) is governed by the chemical reaction rate constant, (k_{chem}), intermicellar exchange rate constant, (k_{ex}), nucleation rate constant (k_n) and the crystallite growth rate constant (k_n).

In a cases of reverse micellar synthesis (as in our case), final nanocrystallites tend to exhibit bimodal or multimodal size distributions in contradiction with to the idea that sizes of the final products should be monodispersed and have the same size as the parent nanodroplets (reverse micelle).

Two growth mechanism, autocatalysis and Ostwald ripening which depend on the reactants exchange and products exchange respectively (*see Figure 2.15*) are said to be contributing factors to this phenomenon [80].

Under autocatalysis, exchange between two colliding micelles which contain product particles results in the growth of the particles.

According to the Ostwald ripening theory, larger particles grow preferentially by fusion of smaller particles which are easily solubilized. Hence reaction-product formation occurs preferentially on the large particles as a result of their large surface area. Small crystallites formed by fusion of dimers inside a droplet can be transferred to another droplet carrying a larger crystallite by

collision. This is made possible only when the protective surfactant film rigidity is very low since the interdroplet exchange of the growing crystallites is repressed by the curvature of the fused molecules.

When the final products are formed (most cases with the water core), the surfactant molecules may be attached directly to the surface of the particles thus preventing further growth. Precipitation and collection of final products is achieved by breaking the surface tension of the microemulsions.

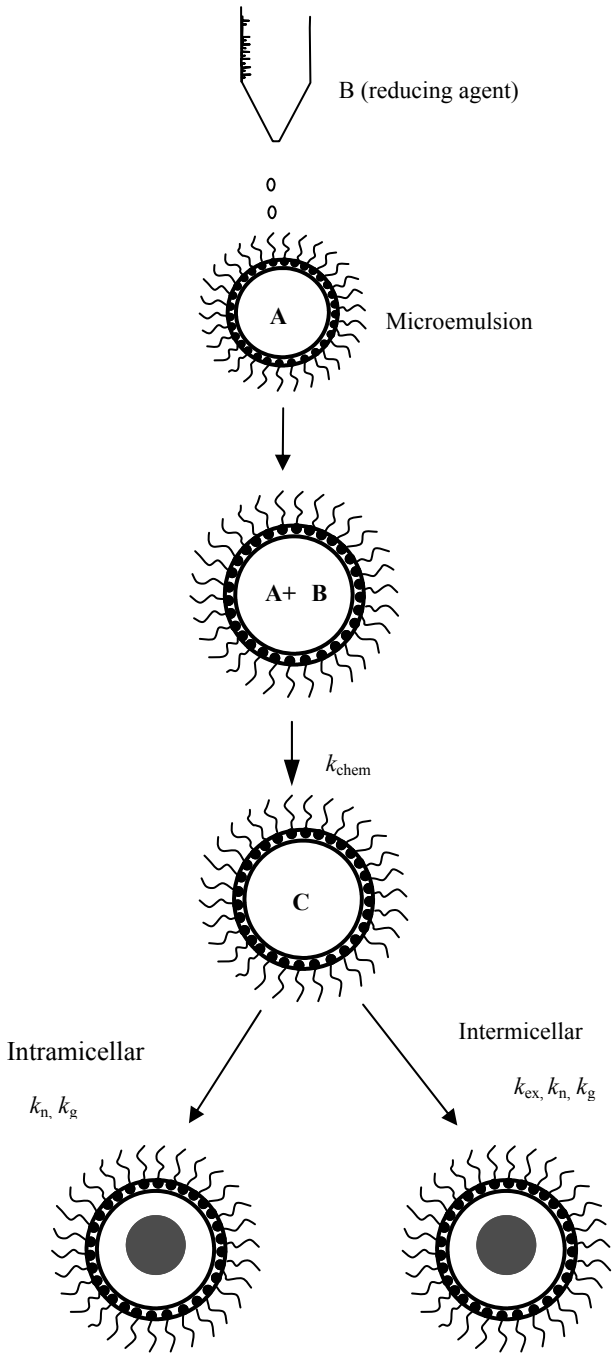

Figure 2. 16 ***Nanocrystallites formation steps in single microemulsion.***

2.3.3.9 Predicting the size of the particles obtained in reverse micelles

There is a rich literature dealing with the correlation between parameters of the reverse micelles (such as size or ω) and the size of the final nanoparticles. The results, however, are discordant: in certain cases a linear relationship between grain size and ω is observed [81], but in a number of technologically important cases (e.g. Pt or Ag), the correlation is not easily spotted out, and a levelling is observed starting from a certain diameter [82].

As already pointed out in the previous sections, reverse micelles formation is determined largely by the molecular packing of the surfactant P_c (cf. eq.(0.11)) [60]. The value of P_c can be calculated on the basis of the geometry of the system. The terms to be used in equation (0.11) for our surfactant (Brij 30) are, respectively the volume of the hydrocarbon (hydrophobic) chain v = (27.4+26.9 nc) $Å^3$ and L_c = (1.54+1.265 nc) Å where nc is the number of carbons. The terms entering those expressions are the volume of CH_3- group (27.4 $Å^3$), the volume of a CH_2 group (26.9 $Å^3$), Van der Waals radius of the terminal CH_3 (1.54 Å) and C-C bond length (1.265 Å). As pointed out previously, spherical reverse micelles are formed when P_c>2 [61].

It is possible, using simple thermodynamic arguments, to find a relationship between micelle size and ω [60]. The specific interface area between surfactant and water can be defined on the basis of a_0 as $\Sigma = nBrij \cdot a_0$. This area can be correlated with ω, noting that:

$$\Sigma = nBrij \cdot a_0 = \frac{Va_0}{v_0} \cdot \frac{\alpha}{\omega} \qquad (0.14)$$

where V is the total volume of the system, $\alpha = V_{H2O}/V$ is the volume fraction of water and v_0=29.2$Å^3$/mol is the effective volume of a water molecule.

Critical parameter is a_0, determined by the balance of the attractive forces between the surfactant heads caused by the interface free energy per unit area γ (of

the order of ca. 20-50 mJ/m^2) and the repulsive forces due to steric hindrance. The latter can be considered, in a first order approximation, as inversely proportional to the surface area "a" occupied by the head group. Thus, the chemical potential can be written as:

$$\left(\mu_N^0\right)_{surf} = \gamma a + B/a \qquad (0.15)$$

where B is a proportionality constant. The minimum of the chemical potential, leading to the optimal head group area is, $a_0 = \sqrt{B/\gamma}$. From the surface to volume ratio of a sphere the average micelle diameter can be expressed as:

$$D = \frac{6v_0}{a_0}\omega \qquad \text{from which } \Sigma = 6\frac{V}{D}\alpha \qquad (0.16)$$

The total number of micelles in the solution can then be found as the ratio between the available interfacial area and the area of a single micelle of radius R:

$$N_m = \frac{\Sigma}{\pi D^2} = \frac{\Sigma a_0^2}{36\pi v_0^2}.\frac{1}{\omega^2} \qquad (0.17)$$

whereas the number of surfactant aggregates is obtained as:

$$K = \frac{\pi D^2}{a_0} = \frac{36\pi v_0^2}{a_0^3}.\omega^2 \qquad (0.18)$$

Equation (0.16) predicts a linear relationship between the diameter of the particles and ω. Figure 2.4(b) shows the trend of the predicted diameter superimposed with the results of XRD -WPPM investigation: calculations were done considering a_0 = 50 Å for Brij30 [36]. The slope of the curve agrees with the large fraction of domains, but the actual values differ. This can be a further indication that the synthesis was not entirely conducted inside the micelles or that, in the solution, the micelles dynamically aggregate to form larger ones. In the literature [36] it is reported that micelles of $C_{12}E_4$/hydrocarbon systems may tend to assume non-

spherical shapes beyond ω = 4; it is therefore possible that for Brij 30 this threshold is lower. This is further supported by the fact that the size of the small fraction is in good agreement with the literature data for the employed microemulsion [36, 83].

2.3.4. Fourier-Transform Infrared (FTIR) spectroscopy

A check for the presence of the organic surfactant on the surface of the as-obtained nanoparticles was done via infrared spectroscopy.

Figure 2.16 shows the FT-IR spectra of the SA set of specimens (the SB set is analogous). All spectra show a prominent band at around 1300-1000 cm^{-1} due to C-O stretching from the surfactant, possibly adhered to the surface of the Cu_2O particles. Two bands are relative to Cu-O modes: the first one, around 625 cm^{-1}, is the signature for Cu_2O as it corresponds to Cu(I) - O stretching. The second one, around 512 cm^{-1}, results from Cu(II)-O stretching and is the marker for the presence of CuO in the system. Traces of CuO are possibly present in all patterns, as the band can be hidden under the tail of the stronger Cu_2O signal. In the SA5 specimen, the quantity of CuO seems higher. The peak at ca. 1632 cm^{-1} is due to the bending vibrations of physically adsorbed water [84] while OH in-plane bending is at 1260 cm^{-1}. All other peaks are due to organic phases. The peak at 1470 cm^{-1} is attributed to CH_2 in-plane bending while that at 725-720 cm^{-1} is due to CH_2 in-plane rocking. The broad band between 1200 cm^{-1} and 1050 cm^{-1} is due to C-O stretching (Polyoxyethylene bond, present in the head group of Brij-30) and the peak around 668 cm^{-1} is the bending of CO_2. All those signals are compatible with the presence of the Brij 30 surfactant. The high-wavenumber region of the spectra is not shown for clarity, but is characterised by the sole presence of the strong O-H stretching band around 3500-3200 cm^{-1}, mainly due to water and ethanol residues.

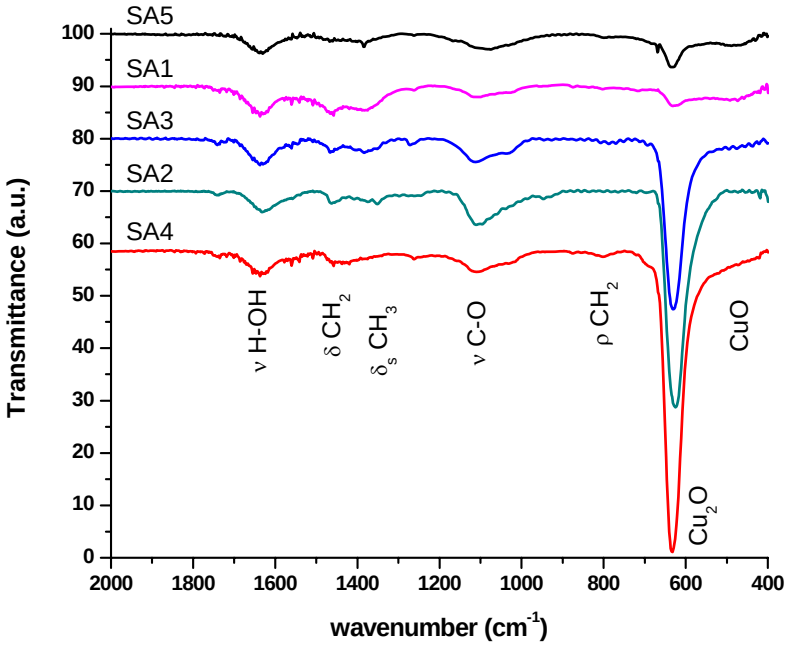

Figure 2. 17. ***FTIR spectra of the SA set of specimens. Data have been shifted for clarity.***

It is worth noting that the FT-IR features attributed to the organics phase increase with ω: this is compatible with the observed increase in the domain/particle size.

2.3.5. UV-Visible-NIR spectroscopy

Figure 2.17 shows the absorption spectra of the as-prepared Cu_2O nanoparticles of set SA: absorption features are present in both the visible range (between 484-615 nm) and in the UV range (in the 264-364 nm region).

The blue shift observed for both peaks with increasing ω is attributed to quantum confinement effects. The general broadening and lack of sharpness in the

absorption spectra may be the result of increasing light scattering caused by the decrease in grain size and widening of the nanocrystal size distribution.

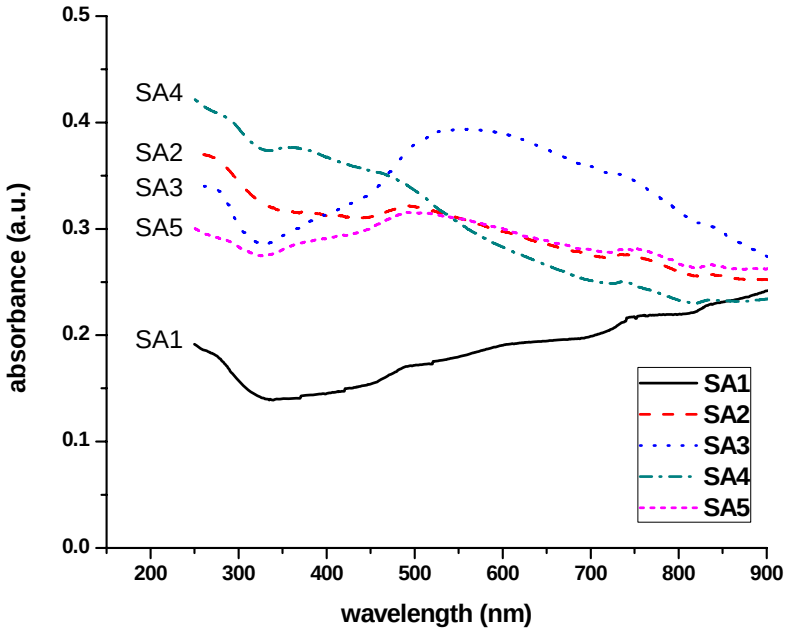

Figure 2. 18. ***UV-Vis-NIR spectra of the SA set.***

A similar effect in the visible range for Cu_2O has been observed by other authors [85, 86]. All observations give a further indication of the nanometric nature of the particles. The effects seem related to the quantity of nanocrystalline domains, as the sharpest feature is observed for SA3, the specimen showing the maximum fraction of larger domains.

2.3.6. Photoluminescence

Two major bands are present in a standard photoluminescence spectrum of

Cu_2O, caused by the recombination of the copper orthoexciton at the fundamental state: in particular, they correspond to the direct (band at ca. 627 nm) and the phonon-mediated (at ca. 633 nm) recombinations. Extra bands seen at lower energy are due to the presence of a large number of copper and oxygen vacancies [87].

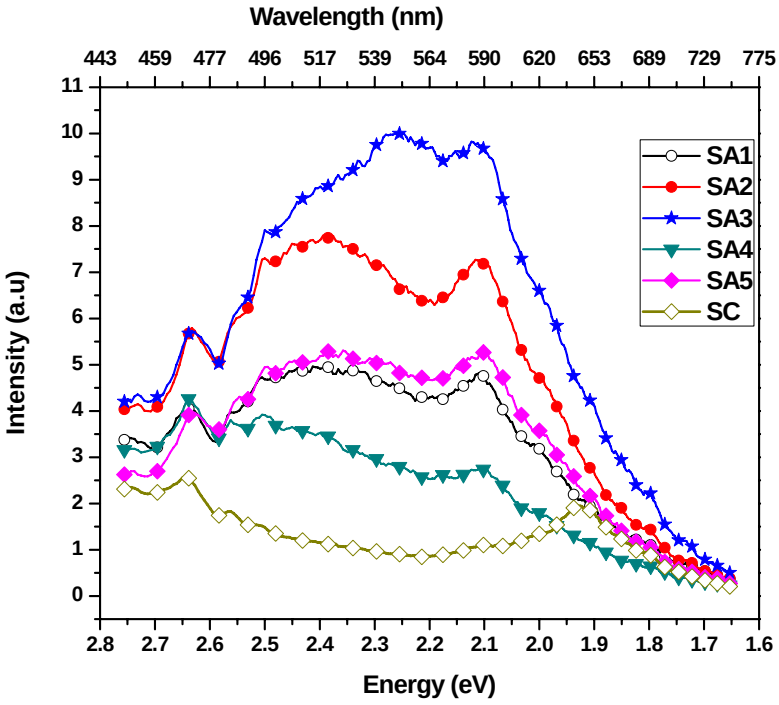

Figure 2. 19. *Photoluminescence spectra of the various specimens (open spheres - SA1, full spheres -SA2, star - SA3, triangles - SA4, Solid Square - SA5, open square - SC)*

The spectra shown in *Figure 2.18* do not match the expected behaviour. Already in the commercial powder, a redshift is evident, with the main spectral peak appearing at 645nm (1.92eV). The redshift can be explained considering that the powder was heat treated to remove copper, therefore grains could be quite large.

The energy bandgaps peaks decrease with increasing quantity of water which is attributed to the size of the particles. The blueshift peaks also show an

apparent decrease with increase in ω which could be attributed to quantum confinement in the nanocrystals. The general reduction of FWHM of the peaks in the blue region is in relation with the size of the particles.

In the SA specimens, the luminescence peaks are located at wavelengths lower than 600nm, due to the confinement of wavefunctions caused by the small size of the domains. It cannot be excluded that the main luminescence signal is due to the smaller fraction of particles (little dependence is observed with ω), whereas the other features, more largely dependent on ω are due to the still nanometric but larger fraction of particles, closer to the behaviour of the commercial powder SC.

2.3.7. Stability of the Cu_2O nanoparticles dispersed in water

As Cu_2O is known to have photocatalytic activity, it was argued whether the cleaned Cu_2O particles dispersed in water would be stable under light irradiation. Aliquots of the same dispersion (SB3 specimen) were thus kept under daylight illumination (SB3I) and in the dark (SB3D) for a maximum time of 3 months. Every month, a couple of specimens (one from the SB3I and the other from the SB3D sets) were analysed by X-ray diffraction. The specimens kept in the dark did not undergo any visible transformation. On the contrary, *(cf. Figure 2.19)*, a large fraction of Cu_2O transformed into CuO after two months illumination.

The degradation mechanism can be simply described by the following set of chain reactions:

$$\begin{aligned} &2hv \rightarrow 2e^- + 2hole^+ \\ &2hole^+ + H_2O_{(l)} \rightarrow \tfrac{1}{2}O_{2(g)} + 2H^+ \\ &2H^+ + 2e^- \rightarrow H_2 \\ &Cu_2O + 2OH^- + h^+ \rightarrow 2CuO + H_2O_{(l)} \end{aligned} \qquad (0.19)$$

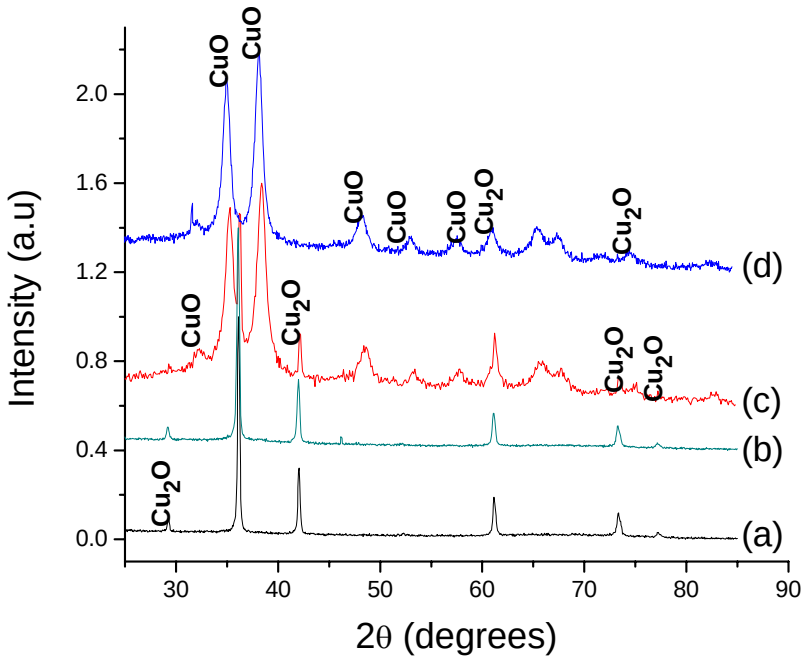

Figure 2. 20. ***Phase transformation under visible light. As produced specimen (a) and specimen kept under daylight illumination for 1 month (b), 3 months (c) and 5 months (d). Data are shifted and rescaled for clarity.***

This suggests the existence on an incubation time for the transformation to start: as it is a self-catalytic reaction, presumably CuO forming on the surface of Cu_2O particles slows the transformation down, acting as a shield for the light. Once a critical size of the nucleus is reached, the transformation starts again with a much higher thermodynamic driving force.

The result of a quantification of CuO done via the Rietveld method is shown in *Table 2.5*. It cannot be excluded that an analogous mechanism is involved in the generation of CuO during the synthesis, even if the time scale is certainly shorter.

	Cu_2O	CuO
As prepared	100	0
1 month	98.1(5) %	1.9(5) %
2 months	9.6(5) %	90.4(5) %
5 months	2.0(3) %	98.0(3) %

Table 2. 5. ***Quantitative phase analysis (% wt) in aged cuprite nanostructured powders kept under illumination.***

However this is a further proof of the self-catalytic transformation of Cu_2O into CuO activated by light irradiation in the presence of water.

2.4. CONCLUSIONS

Nanocrystalline Cu_2O was synthesized in a reverse micelle microemulsion. The domains are defect free and show a tendency to develop a bimodal size distribution, as evidenced by an advanced XRD line profile analysis carried out by Whole Powder Pattern Modelling and validated by electron microscopy observation.

Both Photoluminescence and XRD results indicate that there is no evidence of line defects, and in general line broadening is due to the small sizes of the crystalline domains, which range from 2nm - 20 nm.

The effect of light on the stability of Cuprite in a water-based environment was also studied: Cu2O particles left under daylight illumination start transforming into CuO after about 1 month, with the whole conversion being completed in a few months time.

REFERENCES

1 C. Burda, X.B. Chen, R. Narayanan, M.A. El-Sayed, "Chemistry and Properties of Nanocrystals of Different Shapes", *Chem. Rev.*, **105**, 1025, (2005).

2 A. Roucoux, J. Schulz, H. Patin, "Reduced Transition Metal Colloids: A Novel Family of Reusable Catalysts", *Chem. Rev*. **102**, 3757, (2002).

3 A.P. Alivisatos, "Semiconductor Clusters, Nanocrystals and Quantum Dots", *Science*, **271**,933, (1996).

4 V. Pillai, P. Kumar, M.J. Hou, P. Ayyub, D.O. Shah, "Preparation of nanoparticles of silver halides, superconductors and magnetic materials using water-in-oil microemulsions as nano-reactors", *Adv. Colloid Interface Sci.*, **55,** 241,(1995).

5 J. Eastoe, B. Warne, "Nanoparticle and Polymer Synthesis in Microemulsions", *Curr. Opin. Colloid Interface Sci.*, **1**, 800-805, (1996).

6 L.M. Qi, J.M. Ma, H.M. Cheng, Z.G. Zhao, "Reversed Micelle based formation of $BaCO_3$ nanowires", *J. Phys. Chem.,* **B 101**, 3460,(1997).

7 M.P. Pileni, in: J.H. Fendler (Ed.), "Nanoparticles and Nanostructured Films: Preparation, Characterization and Applications", *Wiley–VCH,* Weinheim, pp.71, (1998).

8 L.M. Qi, J.M. Ma, H.M. Cheng, Z.G. Zhao, "Preparation of $BaSO_4$ nanoparticles in non-ionic w/o microemulsions", *Colloids Surf.,* **A 108,** 117, (1996).

9 S.T. Shishiyanu, T.S. Shishiyanu, O.I. Lupan, "Novel NO_2 gas sensor based on cuprous oxide thin films", *Sensors & Actuators*, **B113,** 468,(2006).

10 A. Mittiga, E. Salza, F. Sarto, M. Tucci, R. Vasanthi, "Heterojunction solar cell with 2% efficiency based on a Cu_2O substrate", *Appl. Phys. Lett.,* **88**,

163502,(2006).

11 P. Poizot, S. Laruelle, S. Grugeon, L. Dupont, J.M. Taracon, "Nano-sized transition-metal oxides as negative-electrode materials for lithium-ion batteries", *Nature*, **407,** 496,(2000).

12 M. Hara, T. Kondo, M. Komoda, S. Ikeda, K. Shinohara, A. Tanaka, J.N. Kondo, K. Domen, "Cu_2O as a Photocatalyst for Overall Water Splitting under Visible Light Irradiation", *Chem. Commun.,* **3**, 357,(1998).

13 P.E. de Jongh, D. Vanmaekelbergh, J.J. Kelly, "Cu_2O: A catalyst for the photochemical decomposition of water?", *Chem. Commun.,* **12,** 1069,(1999).

14 L. Gou, C.J. Murphy, "Solution-Phase Synthesis of Cu_2O Nanocubes", *Nano Letters*, **3 [2],** 231, (2003).

15 P. He, X. Shen, H. Gao, "Size-controlled preparation of Cu_2O octahedron nanocrystals and studies on their optical absorption", *J. Colloid Interf. Sci.,* **284,** 510, (2005).

16 J. Gao, Q. Li, H. Zhao, L. Li, C. Liu, Q. Gong, L. Qi, "One-Pot Synthesis of Uniform Cu_2O and CuS Hollow Spheres and Their Optical Limiting Properties", *Chem. Mater.* , **20,** 6263, (2008).

17 M. Yin, C.-K. Wu, Y. Lou, C. Burda, J.T. Koberstein, Y. Zhu, S. O'Brien, "Copper Oxide Nanocrystals", *J. Am. Chem. Soc.*, **127 [26]**,9506,(2005).

18 A. Martínez-Ruiz, G. Alonso-Nuñez, "New synthesis of Cu_2O and Cu nanoparticles on multi-wall carbon nanotubes", *Materials Research Bulletin,* **43 [6]**, 1492, (2008).

19 C. Salzemann, I. Lisiecki, A. Brioude, J. Urban, M.-P. Pileni, "Collections of Copper Nanocrystals Characterized by Different Sizes and Shapes: Optical Response of These Nanoobjects", *J. Phys. Chem. B*, **108**, 13242, (2004).

20 P. Scardi, M. Leoni, "On the crystal structure on nanocrystalline Cu_2O", *Mat.*

Sci. Eng. A, **393** 396, (2005).

21 P. Scherrer, "Nachr. Ges. Wiss. Göttingen", *Math.-Phys., Kl*., **2**, 98, (1918).

22 P. Scardi, M. Leoni, "Whole Powder Pattern Modelling", *Acta Cryst.,* **A58,** 190, (2002).

23 A. Cervellino, C. Giannini, A. Guagliardi, M. Ladisa, "Nanoparticle size distribution estimation by a full-pattern powder diffraction analysis", *Phys. Rev. B,* **72,** 035412, (2005).

24 P. Scardi, M. Leoni, "Line profile analysis: pattern modelling versus profile fitting", *J. Appl. Cryst.,* **39**, 24-31, (2006).

25 J.P. Cline, R.D. Deslattes, J.-L. Staudenmann, E.G. Kessler, L.T. Hudson, A. Hennins, R.W. Cheary, "NIST Certificate, SRM 660a Line Position and Line Shape Standard for Power Diffraction", Gaithersburg USA, *NIST Standard Reference Materials Program, NIST*, USA, (2000).

26 G. Caglioti, A. Paoletti, F.P. Ricci, "Choice of collimators for a crystal spectrometer for neutron diffraction", *Nucl. Instr. and Meth*., **3**, 223, (1958)

27 M. Leoni, T. Confente, P. Scardi, "PM2K: a flexible program implementing Whole Powder Pattern Modelling", *Z. Kristallogr. Suppl.,* **23,** 249, (2006).

28 Y. Gao-Qing, H-F. Jiang, C. Lin, S.-J. Liao, "Shape- and size-controlled electrochemical synthesis of cupric oxide nanocrystals", *Journal of Crystal Growth*, **303,** 400, (2007).

29 M.P. Pileni, Ed. "Reactivity in Reverse Micelles", *Elsevier*: New York, (1989).

30 T. Iino, K. Ohashi, Y. Mune, Y. Inokuchi, K. Judai, N. Nishi, H. Sekiya, "Infrared photodissociation spectra and solvation structures of $Cu^{+}(H_2O)n$ (n = 1–4)", *Chemical Physics Letters*, **427 [1-3],** 24, (2006)

31 C. Qingde, X. Shen, H. Gao, "Formation of nanoparticles in water-in-oil

microemulsions controlled by the yield of hydrated electron: The controlled reduction of Cu^{2+}", *Journal of Colloid and Interface Science,* **308**, 491–499, (2007).

32 B. E.Warren, "X-ray Diffraction", *Addison-Wesley* - Reading MS, (1969).

33 E.J. Mittemeijer, P. Scardi (eds.) "Diffraction Analysis of the Microstructure of Materials", Springer Verlag - Berlin, (2004).

34 A.C. Nunes, D. Lin, "Effects of Surface Relaxation on Powder Diffraction Patterns of Very Fine Particles", *J. Appl. Cryst.*, **28**, 274, (1995).

35 M. Leoni, P. Scardi, "Grain Surface Relaxation Effects in Nanocrystalline Powders in: Diffraction Analysis of the Microstructure of Materials", Ed. E.J. Mittemeijer & P. Scardi, *Springer Verlag - Berlin*, pp. 413-454, (2004).

36 M. Vasilescu, A. Caragheorgheopol, M. Almgren, W. Brown, J. Alsins, R. Johannsson, "Structure and dynamics of nonionic polyoxyethylenic reverse micelles by time-resolved fluorescence quenching", *Langmuir* ,**11,** 2893,(1995).

37 P. Angshuman, S. Shah, S. Devi, "Preparation of silver, gold and silver–gold bimetallic nanoparticles in w/o microemulsion containing TritonX-100", *Colloids and Surfaces A: Physicochem. Eng. Aspects,* **302,** 483, (2007).

38 C. Tojo, M.C. Blanco, M.A. López-Quintela, "Preparation of Nanoparticles in Microemulsions: A Monte Carlo Study of the Influence of the Synthesis Variables". *Langmuir,* **13 [17],** 4527, (1997).

39 M.P. Pileni, "Reverse micelles as microreactors", *J. Phys. Chem.,* **97 [27]**, 6961, (1993).

40 M. Fanun (ed.), "Microemulsions: Properties and Applications", *Taylor & Francis Group*, Boca Raton, FL, (2009).

41 L. Qi, "Synthesis of Inorganic Nanostructures in Reverse Micelles in

Encyclopaedia of Surface and Colloid science", eds. P. Somasundaran, A. Hubbard, *Taylor and Francis*, pp. 6183-6207,(2006).

42 M. Maillard, S. Giorgio, M. P. Pileni, "Silver Nanodisks", *Adv. Mat.* **14**, 15, (2002).

43 M. de Dios, F. Barroso, C. Tojo, "Nanoparticle Formation in Microemulsions: Mechanism and Monte Carlo Simulations, in Microemulsion properties and applications" vol. 14, M. Fanun (editor), CRC Press, Taylor & Francis Group, Boca Raton, FL., pp. 455-463,(2009).

44 P. Barnickel, A. Wokaun, "Synthesis of metal colloids in inverse microemulsions", *Molecular Physics,* **69 [1]**, (1990).

45 A. Manna, T. Imae, T. Yogo, K. Aoi, M. Okazaki, "Synthesis of Gold Nanoparticles in a Winsor II Type Microemulsion and Their Characterization", *J. Colloid and Interface Sci.,* **256** 297, (2002).

46 M.M. Husein, E. Rodil, E., J.H. Vera, "A novel approach for the preparation of AgBr nanoparticles from their bulk solid precursor using CTAB microemulsions", *Langmuir*, **22 [5]** 2264, (2006).

47 K. R. Lange. "Surfactant: A Practical Handbook," *Hanser Gardner Publications*, Inc., 6915 Valley Avenue, Cincinnati, Ohio, 45244-3029, (1999)

48 M. J. Rosen, "Surfactants and Interfacial Phenomena", *Wiley-Interscience*, 111 River Street, Hoboken, New Jersey 07030, third edition, (2004).

49 N. Moumen, M. P Pileni, "New Syntheses of Cobalt Ferrite Particles in the Range 2−5 nm: Comparison of the Magnetic Properties of the Nanosized Particles in Dispersed Fluid or in Powder Form," *Chem. Mater.,* **8**, 1128-1134. (1996).

50 M. Zulauf, H.F. Eicke, "Inverted Micelles and Microemulsions in the Ternary-System H_2O-Aerosol-OT-Isooctane as Studied by Photon Correlation

Spectroscopy", *Journal of Physical Chemistry*, **83,** [4], 480-486, (1979).

51 M. V. Flores, E. C. Voutsas, N. Spiliotis, G. M. Eccleston, G. Bell, D. P Tassios, P. J Halling, "Critical Micelle Concentrations of Nonionic Surfactants in Organic Solvents: Approximate Prediction with UNIFAC", *Journal of Colloid and Interface Science*,**240**,277-283, (2001).

52 D. Meyers, "Surfactant Science and Technology". 2nd ed.; VCH Publishers: New York, (1992).

53 H. Lange, "Surface films. In: nonionic surfactants", New York: Marcel Dekker, **v. 1**, cap. 14,443-477, (1966).

54 M. Bourrel, R. S. Schechter, "Microemulsions and related systems: formulation, solvency and physical properties"; *surfactant science series*, V. 30, New York: Marcel Dekker, (1988).

55 W. C. Griffin. "Calculation of HLB values of non-ionic surfactants", *J. Soc. Cosmetic Chem.,* **5**,259, (1954).

56 W. C. Griffin., "Classification of surface-active agent by HLB". *J. Soc. Cosmetic Chem.,* **1,**311, (1949).

57 M. J Schick, (editor), "Nonionic Surfactants, Physical Chemistry", **vol. 23**, *Marcel Dekker.Inc., 270 Madison Avenue*, New York, 10016, (1987).

58 C. Tanford, "The hydrophobic effect: formation of micelles and biological membranes", 2nd ed., *New York*: Wiley & Sons, (1980).

59 B. Jönsson, B.Lindman, K.; Holmberg, B. Kornberg, "Surfactants and polymers in aqueous solution", *Chichester:* John Wiley & Sons, (1998).

60 J.N Israelachvili, "Intermolecular and Surface Forces", 2nd Ed., *Academic press*, USA, (1994)

61 D.J Mitchell, B.W. Ninham, "Micelles, vesicles and microemulsions", *J. Chem. Soc. Faraday Trans.,* **2 [77]**, 601, (1981).

62 J. H Clint, “Surfactant aggregation”, *Chapman and Hall*, New York, (1992).

63 J. Solla Gullon, “Caracterizacion y comportamiento electroquimico de nanoparticulas metalicas preparadas en microemulsion”. *Universidad de Alicante*. (2003).

64 P.A. Winsor, “Hydrotropy, solubilisation and related emulsification processes”, *Trans. Faraday Soc.*, **44**, 376, (1948).

65 V. Pillai, P. Kumar, M.J. Hou, P. Ayyub, D.O. Shah, “Preparation of nanoparticles of silver halides, superconductors and magnetic materials using water-in-oil microemulsions as nano-reactors”, *Adv. Colloid Interface Sci.,* **55**, 241,(1995).

66 J. Eastoe, B.Warne, “Nanoparticle and Polymer Synthesis in Microemulsions”, *Curr. Opin. Colloid Interface Sci.,* **1,** 800, (1996)

67 L.M. Qi, J.M. Ma, H.M. Cheng, Z.G. Zhao, “Reversed Micelle based formation of $BaCO_3$ nanowires”, *J. Phys. Chem. B*, **101**, 3460,(1997).

68 M.P. Pileni, in: J.H. Fendler (Ed.), “Nanoparticles and Nanostructured Films: Preparation, Characterization and Applications”, *Wiley–VCH, Weinheim*, 71, (1998).

69 L.M. Qi, J.M. Ma, H.M. Cheng, Z.G. Zhao, “Preparation of $BaSO_4$ nanoparticles in non-ionic w/o microemulsions”, *Colloids Surf. A,* **108**, 117, (1996).

70 T.K. Jain, M.Varshney, and A. Maitra, “Structural studies of Aerosol-OT reverse micellar aggregates by FT-IR spectroscopy”, *J. Phys. Chem.*, **93**, 7409, (1989).

71 Q Zhong, D.A Steinhurst, E.E Carpenter, J.C Owrutsky, “Fourier transform infrared spectroscopy of azide ion in reverse micelles”, *Langmuir*,**18**,7401–7408,(2002).

72 J.C Linehan, J.L Fulton, R.M Bean, "Process of Forming Compounds Using Reverse Micelle or Reverse Microemulsion Systems". *US Patent*, **5**, [770], 172, (1998).

73 R Zana, J Lang, "Dynamics of microemulsions". In S.E Friberg, P Bothorel, editors. "Microemulsions: structure and dynamics". *Boca Raton: CRC Press*; 153–172, (1987)

74 R.P Bagwe, K.C Khilar, "Effects of intermicellar exchange rate on the formation of silver nanoparticles in reverse microemulsions of AOT", *Langmuir*; **16**,905–10, (2000).

75 U Natarajan, K Handique, A Mehra, J.R Bellare, K.C Khilar, "Ultrafine metal particle formation in reverse micellar systems: effects of intermicellar exchange on the formation of particles", *Langmuir*; **12**, 2670–2678, (1996).

76 R Hua, C Zang, C Shao, D Xie, C Shi, "Synthesis of barium fluoride nanoparticles from microemulsion", *Nanotechnology*, **14**,588–91, (2003).

77 J.C Lin, J.T Dipre, M.Z Yates. "Microemulsion-directed synthesis of molecular sieve fibers," *Chem Mater;* **15,** 2764–2773, (2003).

78 D Roux, A.M Bellocq, P Bothorel., "Effect of the molecular structure of components on micellar interactions in microemulsions," *Progress in Colloid and Polymer Science,* **69,**1–11, (1984).

79 J.D Hines., "Theoretical aspects of micellisation in surfactant mixtures", *Curr Opin Colloid Interface Sci.,* **6,350**–356, (2001)

80 M.A. Lopez-Quintela, "Synthesis of nanomaterials in microemulsions: formation mechanisms and growth control", *Curr. Opin. Colloid Interface Sci.,***8,** 137–144,(2003).

81 M.P. Pileni, "The role of soft colloidal templates in controlling the size and shape of inorganic nanocrystals", *Nature Mater.,* **2**,145, (2003).

82 J. Tothova, M. Richterova, V. Lisy, “On two direct methods for measurement of interfacial tension at microdroplet surfaces”, *Institute of Physics,* **Paper deposited on arXiv**, P.J. Safarik University, Slovakia.

83 F. Luo, D Wu, L. Gao, S. Lian, E. Wang, Z. Kang,Y. Lan, and L. Xu ,”Shape-controlled synthesis of Cu_2O nanocrystals assisted by Triton X-100,”*Journal of Crystal Growth*, **285,** 534,(2005).

84 A.S. Arico, V.Baglio, A. Di Blasi, V. Antonucci, “FTIR spectroscopic investigation of inorganic fillers for composite DMFC membranes”, *Electrochemical communications*, **5**, 862, (2003).

85 M. Yang, J. Zhu, “Spherical hollow assembly composed of Cu_2O nanoparticles”, *J. Crystal Growth*, **256**,134, (2003).

86 K Borgohain, N. Murase, S. Mahamuni, “Synthesis and properties of Cu_2O quantum particles”, *J. Appl. Phys.,* **92 [3],** 1292, (2002).

87 J Bloem “Optical and electrical properties of cuprous oxide,” *Philips Research Reports,* **13**, 167-93, (1958).

CHAPTER 3

3. High Energy Milling of Bulk Cu_2O powder[2]

ABSTRACT

X-ray diffraction line profile analysis based on the recently developed Whole Powder Pattern Modelling was used to investigate the microstructure changes in Cu_2O powders milled in a vibrating cup mill. The reduction in the average size of coherently scattering domains - and simultaneous narrowing of the size distribution - occurs in the first minutes. An asymptotic limit of ca. 10 nm is obtained. The reduction in size is obtained at the expenses of introducing a massive quantity of dislocations in the system, reaching a limit of ca. 4×10^{-16} m^{-2}. A proper nanocrystalline microstructure can be obtained for a milling of ca. 20 min.

3.1. INTRODUCTION

Nano-sized particles keep attracting the attention of many researchers worldwide because of their peculiar chemical properties arising from the high surface/volume ratio and possible quantum confinement effects. Several chemical, physical, mechanical and mechano-chemical methods have been proposed in the literature for the synthesis of nanostructured materials. Among them, high energy milling has an undoubted technological importance as it allows producing large quantities of nanostructured powder in short time and at competitive prices.

Among the various types of mill available on the market, the vibrating cup mill, composed of a massive cylinder wobbling at high speed inside an hermetic cup, is perhaps the most energetic one. In order to remove the excess energy

[2] *Part of the results shown in the present chapter has been published in: Scardi P., Leoni M., Dodoo-Arhin D., "Advancements in the modelling of diffraction line profiles from nanocrystalline materials". XXI Conference on Applied Crystallography, Zakopane, Poland - 20-24 September, 2009. Solid State Phenomena, 163, 19-26, (2010.)* doi:10.4028/www.scientific.net/SSP.163.19. *A further manuscript has been submitted for publication in: D. Dodoo-Arhin, G. Vettori, M. D'Incau, M. Leoni, P. Scardi, "High Energy Milling of Bulk Cu_2O powder", Z. Krist Suppl., 2010.*

transformed in heat, the mill can be modified by the addition of a suitable cooling circuit [1, 2].

The microstructure of the nanostructured materials resulting from milling can be investigated both by microscopy (Scanning Electron Microscopy (SEM) and Transmission Electron Microscopy (TEM)) and by X-ray diffraction (XRD). Albeit providing indirect information, XRD of nanocrystalline powders guarantees a better statistical significance of the result, as the information is collected on a much larger quantity of grains (millions versus tens analyzed under the microscope).

Line Profile Analysis (LPA) is the group of techniques employed for microstructure analysis from diffraction data, as they are based on the analysis of the broadening of the diffraction peaks. It should be recalled that the broadening of the X-ray diffraction line profiles is determined by instrumental features but also by the small size of the coherently scattering domains (aka crystallites) and by lattice distortions (dislocations, stacking faults, etc). The most widespread technique for the analysis of XRD data is certainly the Scherrer formula [3,4], even if it provides just an estimate of the domain size. The state of the art alternative is offered by methods that analyse the whole diffraction pattern. Among them, Whole Powder Pattern Modelling (WPPM) [5] provides for an interpretation of the whole diffraction pattern in terms of physical models for the broadening sources. The WPPM allows a proper quantitative analysis of the microstructure of finely divided materials both from laboratory and synchrotron radiation data.

Cuprite (Cu_2O, space group $Pn\bar{3}m$, ICDD PDF2 card #05-0667, a = 4.267Å) is a wide bandgap (2.0–2.2eV) p-type semiconductor that finds important technological applications e.g. in solar cells [6], gas sensors [7] chemical refinement catalysis [8] and water splitting [9]. The possibility of producing nanostructured Cu_2O could led to an increased activity of the material [10].

Traditionally, nanostructured Cu_2O is produced via chemical synthesis as shown in *Chapter 2* of this thesis. We report here the successful reduction in size of

a commercial cuprite powder and its detailed microstructural characterisation via WPPM of synchrotron radiation data and microscopy.

3.2. EXPERIMENTAL

3.2.1. Milling process

Commercial Cu_2O (99.99+%, Sigma Aldrich - 566284-25G) was employed as starting material. Preliminary X-ray characterization of the powder evidenced the presence of a large quantity of metallic Cu and a small quantity of CuO. The powder was then subjected to thermal oxidation at 850 °C in a tubular furnace at a pressure of 9.5 mbar for 1 h and subsequently stored in sealed containers under Ar atmosphere.

The removal of metallic copper and CuO impurities to obtain pure starting Cu_2O powders is fundamental to this work; the comprehension of the theoretical basis of the thermodynamic stability regions of metallic oxides under conditions of temperature and pressure can be investigated using the concept of Ellingham diagrams [11]. The conversion of metallic copper into copper oxides (Cu_2O and CuO) is an oxidation reaction governed by a chemical equilibrium between the reactants and products, represented by the reactions (0.20) and (0.21):

$$4Cu(s)+O_2(g)\longrightarrow 2Cu_2O(s) \qquad (0.20)$$

$$2Cu_2O(s)+O_2(g)\longrightarrow 4CuO(s) \qquad (0.21)$$

The equilibrium of each of those reactions is represented via suitable reaction constants. It is possible to demonstrate that in this type of oxidation reactions, the reaction constant is inversely proportional to the partial oxygen pressure. This allows writing, for each reaction:

$$\ln p_{O_2} = \frac{\Delta G}{RT} \quad \Rightarrow \quad p_{O_2} = \exp\left(\frac{\Delta G}{RT}\right) \qquad (0.22)$$

where ΔG is the variation of the Gibbs free energy, R is the ideal gas constant

(8.3145 J mol^{-1} K^{-1}) and T is the temperature (K).

The reaction (0.20) implies that an oxygen partial pressure in excess of the equilibrium pressure favours the formation of Cu_2O, whereas an oxygen partial pressure below the equilibrium value would move the reaction towards metallic copper. An analogous reasoning applies to (0.21).

Furthermore, it is known that, for a chemical reaction, the Gibbs free energy change at a temperature is the sum of the Gibbs energies of formation of the products, minus the sum of the Gibbs free energies of formation of the reactants at the same temperature, which is usually determined from the values of enthalpy change (ΔH_T) and entropy change (ΔS_T).

Assuming that there are no phase transformations between room temperature 298K and a final temperature T:

$$\Delta G_T = \Delta H_T - T\Delta S_T \qquad (0.23)$$

For the systems investigated here, the following applies [11]:

$$\Delta G_T\ (Cu_2O) = -338904 + (-14.24\ T\ lnT) + (246.86\ T)\ (Joule) \qquad (0.24)$$

$$\Delta G_T\ (CuO) = -292461.6 + (-22.16\ T\ lnT) + (370.70\ T)\ (Joule). \qquad (0.25)$$

According to those equations, the stability range of Cu, Cu_2O and CuO are illustrated in *Figure (5.1)*.

Based on the above theoretical considerations, the thermal treatments were performed in a tube furnace (1000° C maximum temperature; heating by radiation). The furnace is equipped with a two-open-end quartz tube capable of gas fluxing treatments connected to a vacuum pump system whose minimum pressure is $5x10^{-3}$ mbar *(see Figure 5.2)*.

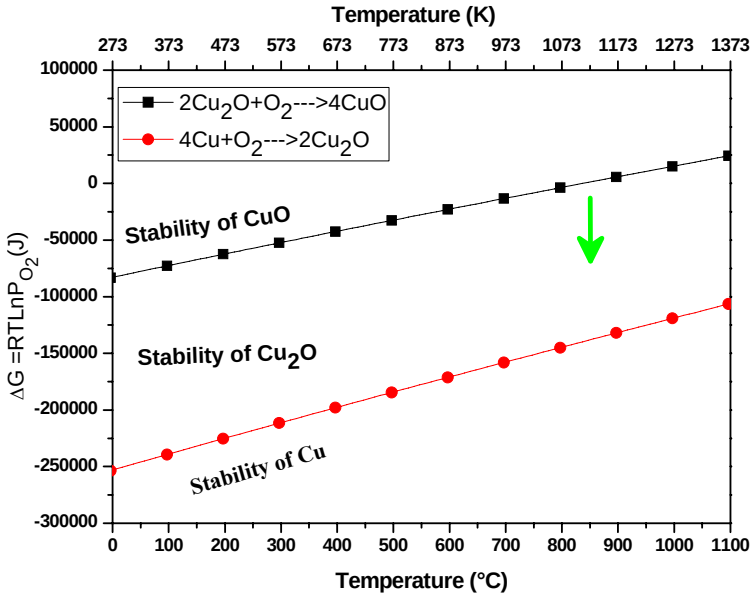

Figure 3. 1. *Variation of Gibbs free energy with Temperature. Arrowed region is the Cu_2O stability zone. The black line (square) represents the equilibrium between the Cu_2O and CuO phases, while the red line (spheres) represents the equilibrium between Cu and Cu_2O.*

Figure 3.2

Figure 3. 2.. *Tubular furnace used for the thermal treatment.*

The powder is placed in an alumina crucible and inserted into the furnace. The quartz tube is closed and the pressure pump is started at its minimum pressure of about $3x10^{-3}$ mbar to prevent any oxidation at the early stages. To eliminate the small quantity of CuO phase in the powder, about one hour of isothermal heating at 850°C was performed. The pressure is then increased to 9.5 mbar under isothermal conditions for one hour to ensure a complete oxidation of all the residual metallic copper.

After treatment, the closed tube is allowed to cool down at low pressure, equivalent to the initial pressure, so as to prevent the re-oxidation of the formed Cu_2O into CuO. It is worth stating that, in view of the absence of pure oxygen, relative oxygen concentration in air (atmospheric air intake) was used with the assumption that, other gases such as carbon dioxide, water vapour etc., do not react with metallic copper. Therefore a scale factor of 0.21 was employed being 21% the concentration of oxygen in the atmosphere.

The heat treated powder was milled on a Fristch Pulverisette 9 Vibromill using a ferritic steel grinding set *(figure 3.3)*. A cup of 120ml (nominal volume) and a 662.20 g crushing cylinder were used. Approximately the same amount of Cu_2O powder (≈ 3.0 g) with 4 %wt ethanol were milled in static Ar atmosphere respectively for 1, 5, 7.5, 10, 20 and 40 min. The corresponding specimens are named P9-1 through P9-40. The given time represents the actual milling time: the process time, however was much longer. In fact, to limit possible effects of heating - leading e.g. to recrystallization - the milling was done in batch cycles consisting of a 1 minute milling followed by 5 minutes pause.

To further dissipate the large fraction of energy converted into heat in the mill, the mill was customised to allow temperature control of the cup. A special cup was designed, allowing for the outer circulation of a suitable refrigerant. A Huber cooling system (Huber Technik, Peter Huber Kältemaschinenbau GmbH, Germany) *(figure 3.3)* providing a constant circulation of water-ethylene glycol

mixture at about -20°C was employed [1, 2].

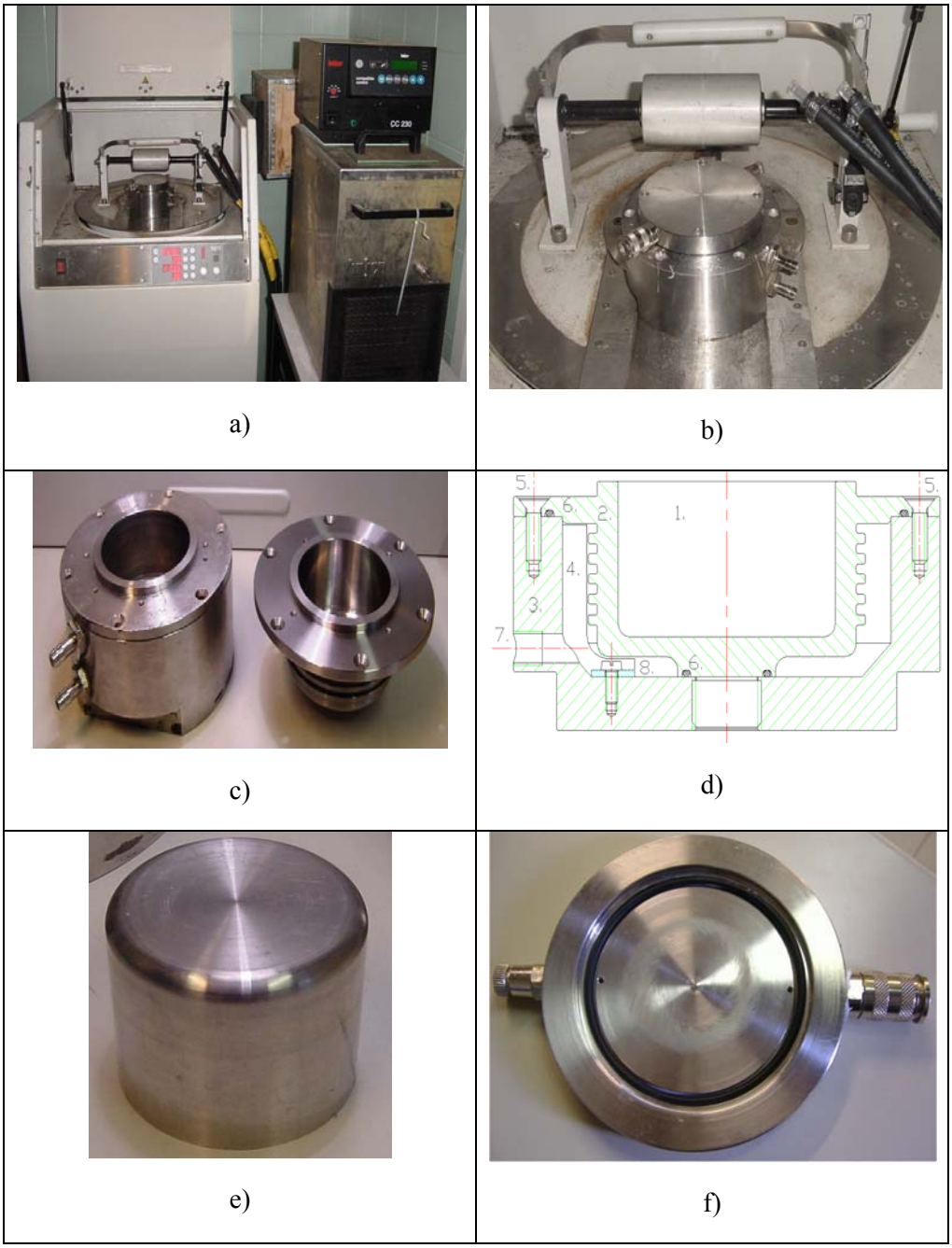

Figure 3. 3. ***Modified Fritsch Pulverisette 9 mill.***

Loading, unloading, collection and storage of the powder was done under Argon atmosphere, to avoid any destabilization of Cu_2O.

3.2.2 Thermal Equilibrium stability of the Cu_2O-CuO-Cu system

To investigate the thermal stability of the milled copper oxide, samples were studied by DTA/TG in static air under atmospheric conditions. Approximately equal aliquots of ca. 23 mg of powder were placed in Al_2O_3 crucibles (100 mg capacity), subjected to a linear heating ramp between 20°C and 1300°C at a rate of 10°C/min and a cooling rate of 50°C/min, using a Setaram TG-DTA apparatus equipped with a LABSYS TG-ATD 1600°C rod *(see Figure 3.4)*. The test measurements were made for the mass variation of the sample as a function of the temperature and the phase changes by the adsorption or the emission of energy (heat flow) against temperature. Analyses of the peaks were conducted using the Setaram proprietary software.

Figure 3. 4. ***DSC-DTA-TG apparatus employed in this work.***

3.2.3 XRD measurements and WPPM

Synchrotron X-ray diffraction data were collected on the ID31 high-resolution powder diffraction beamline at the European Synchrotron Radiation Facility (ESRF) in Grenoble - France.

A high data throughput is obtained on ID31 through the use of a particular detector system consisting of a series of nine detectors *(Figure 3.5),* each with an angular separation of 2° and preceded by a Si (111) analyzer crystal. In our case, the information collected every 15ms from the nine detectors was suitably mixed and re-binned to provide diffraction patterns in the 2.0° - 65.0° 2θ range with an angular increment of 0.005°.

A wavelength of 39.99284 pm was chosen, calibrated with the NIST SRM 640b (Si) standard. In order to obtain the best pattern quality (no specimen holder effects), the powder was mounted free standing in a 5x5 mm silicon frame (500 μm thickness) obtained by removing the 500nm Si_3N_4 membrane from the specimen

holder. A θ/2θ scanning mode (parallel-beam transmission geometry) was employed.

The diffraction pattern of the NIST SRM 660a line profile standard (LaB_6) [12] was also collected under the same experimental conditions, in order to characterize the instrumental effects (Instrumental Profile - IP) on the diffraction line profiles. A set of 20 evenly spaced line profiles was simultaneously fitted with symmetrical pseudo-Voigt functions whose width and shape was constrained according to the Caglioti *et al.* formulae [13]. The PM2K software [14] was employed.

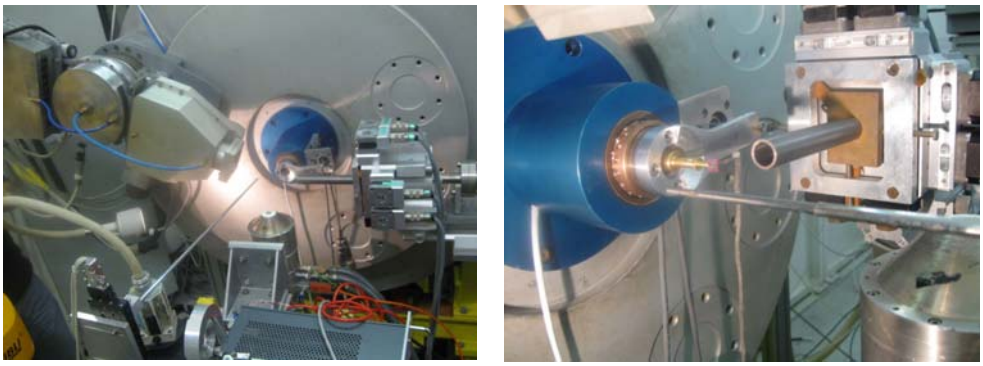

Figure 3. 5. ***Diffractometer running on the ID31 beamline at the European Synchrotron Radiation Facility.***

X-ray powder diffraction data of the same specimens were also collected on a laboratory PMG-VH (Rigaku, Japan) horizontal powder diffractometer *(Figure 3.6)* in Bragg-Brentano geometry, operated at 40Kv and 30mA using a Cu tube. The goniometer set up includes narrow slits (1° divergence, 1° incident beam Soller, 1° diffracted beam Soller, 0.15 mm receiving) and a secondary curved graphite analyser crystal, providing narrow and symmetrical instrumental profiles over the required angular range. The XRD specimens were prepared by compacting each of the milled powders into a 2x2 cm aluminium frame sample holder. All XRD patterns of samples were recorded in the 25° - 145°, 2θ° range using a step

size of 0.1° and a counting time of 20 s per step without moving the sample. Again, the instrumental profile was obtained experimentally by collecting diffraction data of a standard LaB_6 powder [12], fitting all visible peaks with pseudo-Voigt functions and parameterizing the trends of the FWHM and shape parameters according to the Caglioti *et al.* relationships [13].

Qualitative phase analysis (search match) was done using the PANAlytical X'pert Highscore software. The ICDD PDF-4+ database was employed. Quantitative phase analysis was obtained via the Rietveld method [14] using the Bruker Diffracplus TOPAS 4.2 software [15].

The Whole Powder Pattern Modelling (WPPM) method [5] implemented in the PM2K software [16] was employed for the microstructure analysis.

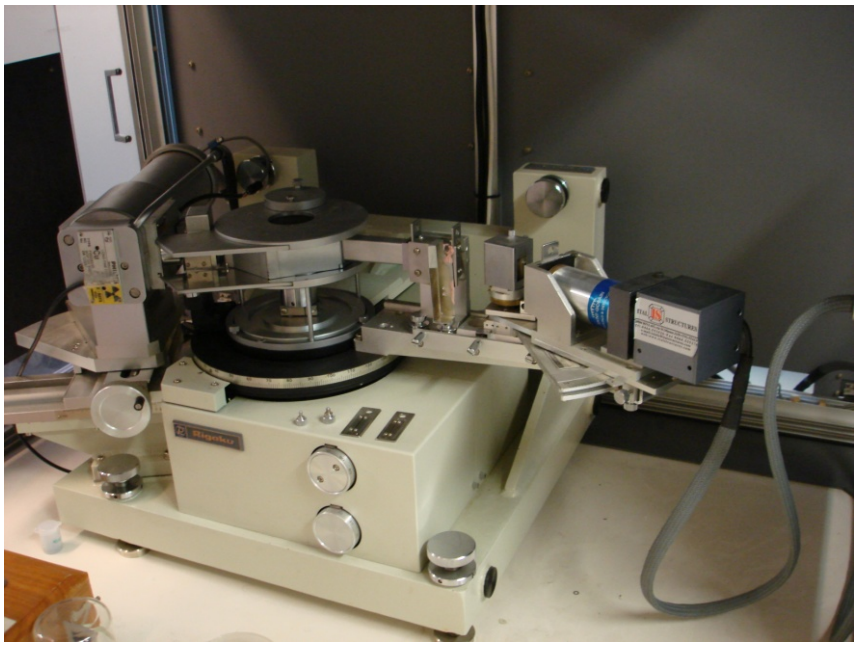

Figure 3. 6. ***Rigaku PMG-VH laboratory diffractometer employed in the present work.***

The fundamental theory and expressions of the approach is herein briefly described, following the ideas proposed in [4, 16-25]. The X- ray diffraction line

profile is a convolution of the influence of the microstructure of the analysed sample and that of the diffraction instrument. Mathematically, these effects can be expressed using a Fourier Transform as:

$$I_{hkl}(s) = k(s)\int T^{IP}(L)\,A^{S}(L)\,A^{D}_{hkl}(L)\,e^{2\pi iLs}\,dL \qquad (0.26)$$

In the formula, L is the Fourier (integration) variable and s is the reciprocal space variable conjugate to L, defined as:

$$s = d^{*} - d^{*}_{B} = \frac{2}{\lambda}(\sin\theta - \sin\theta_{B}) \qquad (0.27)$$

whereλ is the wavelength, whereas θ and θ_{B} are running angle and Bragg angle, respectively.

The term $k(s)$ in *(0.26)* includes the Lorentz-polarisation factor and known functions of s such as the square modulus of the structure factor and the absorption terms. The integrands in *(0.26)* are the Fourier transforms of the broadening contributions. In particular, T^{IP} is the Fourier Transform of the instrumental profile, whereas A^{S} and A^{D}_{hkl} are the terms accounting, respectively, for the finite size of the coherently diffracting domains and for the presence of dislocations.

A monodisperse (i.e. single-valued) distribution is considered in traditional analyses. It is however possible, as shown in [17], to include a distribution in the analysis. In the present case, a lognormal distribution of spherical domains was considered. The lognormal distribution is defined as:

$$g_{h}(D) = \frac{1}{D\sigma\sqrt{2\pi}}\exp\left[-\frac{1}{2}\left(\frac{\ln D - \mu}{\sigma}\right)^{2}\right] \qquad (0.28)$$

where μ is the lognormal mean and σ is the standard deviation (square root of the lognormal variance). The Fourier term corresponding to the size broadening can be written as [17]:

$$A^S(L) = \frac{\int_L^\infty D^3 A^S_{sphere}(L,D)\, g_h(D)\, dD}{\int_0^\infty D^3 g_h(D)\, dD} \tag{0.29}$$

where

$$A^S_{sphere}(L,D) = 1 - \frac{3}{2}\frac{L}{D} + \frac{L}{2}\left(\frac{L}{D}\right)^3 \tag{0.30}$$

is the Fourier Transform for a sphere of diameter D.

Dislocation effects are considered according to the Krivoglaz-Wilkens theory [18-25]. The Fourier transform term $A^D_{hkl}(L)$ obtained when assuming a random distribution of dislocations reads:

$$A^D_{hkl}(L) = \exp\left[-\frac{1}{2}\pi |b|^2 \bar{C}_{hkl} \rho d^{*2}_B L^2 f^*(L/R_e)\right] \tag{0.31}$$

where ρ is the average dislocation density, R_e is the effective outer cut-off radius, f^* is a known function proposed by Wilkens [20] and b is Burgers vector modulus. The line broadening anisotropy resulting from the presence of the dislocations is condensed in the average contrast factor $\bar{C}_{hkl}$ term [21, 22]. In the case of cubic materials, the contrast factor can be written as [5, 22]:

$$\bar{C}_{hkl} = A + B \cdot H \tag{0.32}$$

where

$$H = \left(h^2k^2 + k^2l^2 + l^2h^2\right) \Big/ \left(h^2 + k^2 + l^2\right)^2 \tag{0.33}$$

The constants A and B can be determined from the elastic constants and slip system of the material under consideration using the general formalism provided in [24].

Due to their different structure, copper, CuO and Cu_2O show distinct responses to the presence of dislocations. The primary slip system for Cu_2O is

<001>{100} [24]; simple expressions for the contrast factor can be obtained in this case [24] and calculation is analytical once the elastic constants are provided. Single crystal elastic constants for Cu_2O are c_{11}=121, c_{12}=105 and c_{44}=12.1 GPa [26, 27]. Dislocations in copper are expected on the ½<1-10>{111} slip system, the primary one for *fcc* metals. Several publications deal with the calculation of the contrast factor of copper. For tenorite, the approach presented in [25] and based on the use of the Laue group invariant was used and the coefficients of the invariant were refined. The approach is the generalization of the idea presented above, where the average contrast factor is parameterised according to a suitable expression in *h*,*k*,*l*. The 4th order invariant for tenorite reads [25, 28]:

$$d_{hkl}^{*4}\overline{C}hkl = E_1h^4 + E_2k^4 + E_3l^4 + 2E_4h^2k^2 + 2E_5k^2l^2 + 2E_6h^2l^2 + 4E_7h^3k + 4E_8hk^3 + 4E_9hkl^2 \quad (0.34)$$

It is worth saying, however, that the anisotropy in tenorite is quite limited and can be neglected given the small quantity found here.

Summarising, in addition to the peak intensities, unit cell parameter and coefficients of a Chebyshev polynomial background, the microstructure parameters refined are the lognormal standard deviation σ, lognormal mean μ, dislocation density ρ and effective outer cutoff radius R_e. Wilkens parameter $W = Re\sqrt{\rho}$ is calculated from those parameters, providing information on dislocation interaction.

3.2.3 Electron Microscopy

The morphology of the powders was studied with a FEI XL30 Environmental Scanning Electron Microscope (ESEM) equipped with an Energy Dispersive X-ray Spectroscopy system (EDAX FALCON) based on a nitrogen-cooled Si-Li detector (*see Figure 3.7*). Initial observations were made on the samples without metallization at 20 kV and 51 µA. To improve the resolution, specimens were subsequently metalized and analyzed at 30 kV and 93 µA. All observations were made in ESEM mode at a water pressure of 0.7 Torr.

High Resolution Transmission Electron microscopy was carried out on a JEOL 2100 URP microscope operated at 200 kV. The microscope is equipped with a Gatan "Ultrascan" 2k x 2k CCD camera and has a point and line resolution of 0.19 nm and 0.14 nm respectively, scaled with Au(100).

Figure 3. 7. ***FEI XL30 ESEM employed in the present study.***

3.3. RESULTS AND DISCUSSION

Figure 3.8 proposes an interesting comparison between the synchrotron radiation and laboratory diffraction data. It is clear that synchrotron data are superior in terms of extended reciprocal space accessibility regions, improved count statistics (better signal/noise ratio) and higher resolution (narrower instrumental profile). Whenever possible, the analyses will be conducted on the synchrotron data, and those conducted on the laboratory data will be used for comparison.

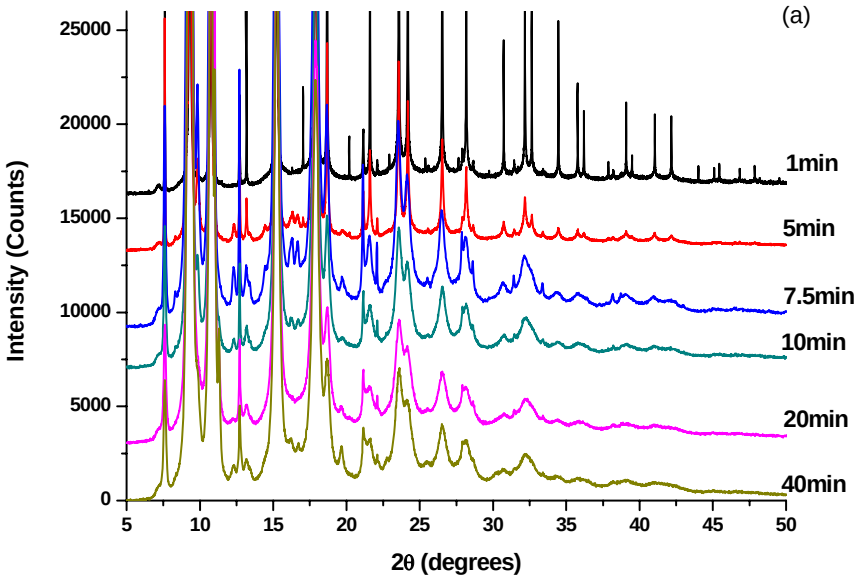

Figure 3. 8. ***(a) Synchrotron radiation XRD data of ball milled samples (patterns have been shifted for clarity).***

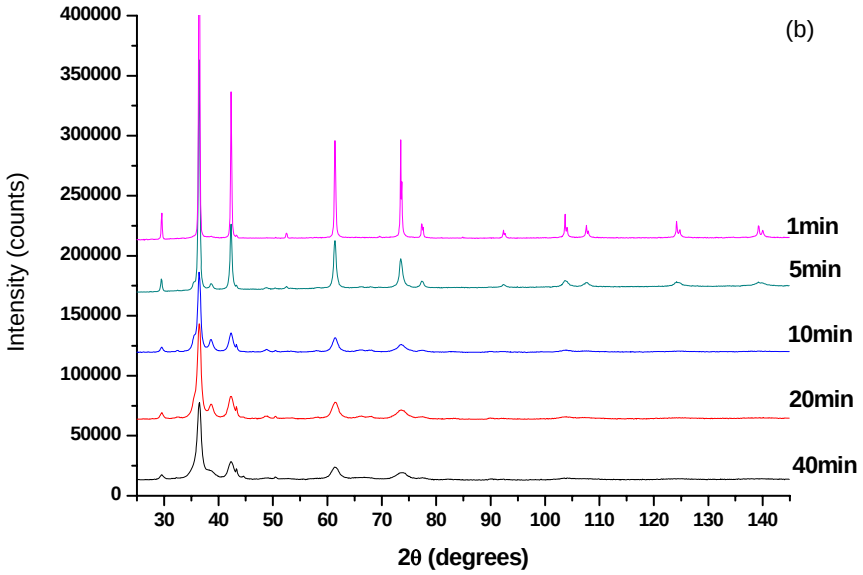

Figure 3.8. *(b) laboratory XRD patterns of ball milled samples (patterns have been shifted for clarity).*

3.3.1 Quantitative Phase Analysis

According to the Ellingham diagram, cuprite should be the stable phase obtained from the annealing treatment performed on the commercial powder. The analyses conducted with the X'Pert HighScore software reveal the presence of Cu_2O, CuO and Cu, in clearly different proportions among the various specimens.

All three phases could be quantified using the Rietveld method: the results of the analysis of synchrotron data are proposed in *Table 3.1*. The presence of the three phases, and in particular of tenorite (CuO), has to be attributed to the milling process, as the starting heat treated powder is pure Cu_2O (within the limits of detection of XRD). The Rietveld fit is good but not perfect: there is still a certain degree of anisotropic broadening not completely taken into account by our isotropic model, but this should be within the errors presented in *Table 3.1*.

It can be seen a clear increase in the content of Cu with the milling time. It cannot be excluded that the phase identified as Cu is a mixed Cu/Fe phase. Contamination from the mill is certainly possible; some deposition of a metallic copper film has been observed on the surface of the cup and cylinder. However, the milling was done in static Ar atmosphere, so the quantity of oxygen available in the cup is very limited. Part of the metallic copper, however, can come from the cuprite - tenorite - copper transformation.

Milling time (min)	**wt% Cu_2O**	**wt% CuO**	**wt% Cu**
1.0	93.5(1)	3.9(1)	2.6(9)
5.0	89.4(3)	6.9(5)	3.7(4)
7.5	90.2(1)	5.1(1)	4.7(2)
10.0	92.5(1)	1.7(5)	5.8(8)
20.0	88.0(1)	6.0(3)	6.0(4)
40.0	86.7(1)	6.5(1)	6.8(3)

Table 3. 1. ***Quantitative Phase Analysis Results obtained from synchrotron data.***

Assuming that the transformation occurs in the absence of oxygen, we can see that up to 7wt% Cu could be produced if all CuO comes from Cu_2O.

3.3.2 Microstructural analysis via WPPM

Several tests were made on both the SR data and the LXRD data, to identify the best models to be used in the analysis. The best results were obtained using the WPPM approach in which domains are assumed as being spherical and their diameters distributed according to a lognormal distribution. Dislocations were identified as the main cause of strain broadening.

The main WPPM results are shown in *Tables 3.2* and *3.3* for the synchrotron

and laboratory data, respectively.

Specimen	Milling Time (min)	a_0 (nm)	<D> (nm)	σ (nm)	ρ (10^{15} m^{-2})	R_e (nm)	Wilkens parameter
P9-1	1.0	4.2673(1)	45(1)		0.3(2)	11(1)	0.1(1)
P9-5	5.0	4.2682(6)	20(1)	67(7)	7(1)	9.0(6)	0.74(1)
P9-7.5	7.5	4.2709(5)	16(1)	42(13)	21 (1)	5.0(2)	0.72(1)
P9-10	10.0	4.2744(1)	11.9(9)	21 (3)	30(1)	3.0(1)	0.52(2)
P9-20	20.0	4.2736(2)	9.3(4)	10 (1)	39(1)	2.3(1)	0.45(2)
P9-40	40.0	4.2736(2)	9.8(5)	11(1)	42(1)	2.4(1)	0.48(3)

Table 3. 2. ***WPPM results from the analysis of synchrotron radiation XRD data: unit cell parameter a_0, average domain size <D>, lognormal variance σ, dislocation density ρ, effective outer cut-off radius R_e and Wilkens' parameter $W = Re\ \rho^{1/2}$.***

Specimen	Milling Time (min)	a_0 (nm)	<D> (nm)	σ (nm)	ρ (10^{15} m^{-2})	R_e (nm)	Wilkens parameter
P9-1	1.0	4.2680(2)	55.9(6)	122(2)	3.9(2)	1.1(5)	0.07(6)
P9-5	5.0	4.2696(5)	17.7(3)	49(3)	10.3(1)	1.2(4)	0.12(4)
P9-10	10.0	4.2697(3)	10.4(4)	15(3)	31.4(5)	0.04(6)	0.17(1)
P9-20	20.0	4.2733(1)	9.5(2)	10.3(1)	64.2(1)	1(2)	0.25(4)
P9-40	40.0	4.2759(2)	8.5(2)	10.4(2)	61(1)	1.6(6)	0.39(3)

Table 3. 3 ***WPPM results from the analysis of laboratory XRD data: unit cell parameter a_0, average domain size <D>, lognormal variance σ, dislocation density ρ, effective outer cut-off radius R_e and Wilkens' parameter $W = Re\ \rho^{1/2}$.***

All other specimens but the P9-1 give an excellent fit. In the case of the shortest milling time (P9-1) proper and reliable modelling was not achieved using any simple combination of the broadening models. This may indicate a high

inhomogeneity in the grain size. In fact the larger grains (large scattering power) tend to shadow the smaller grains (smaller volume, i.e. smaller overall scattering power), thereby leading to incorrect grain statistics evaluation.

As an example, *Figures 3.8* and *3.9* proposes the experimental diffraction patterns and the corresponding WPPM (model) results for the P9-40 specimen. Both the synchrotron and laboratory data are well modelled via WPPM.

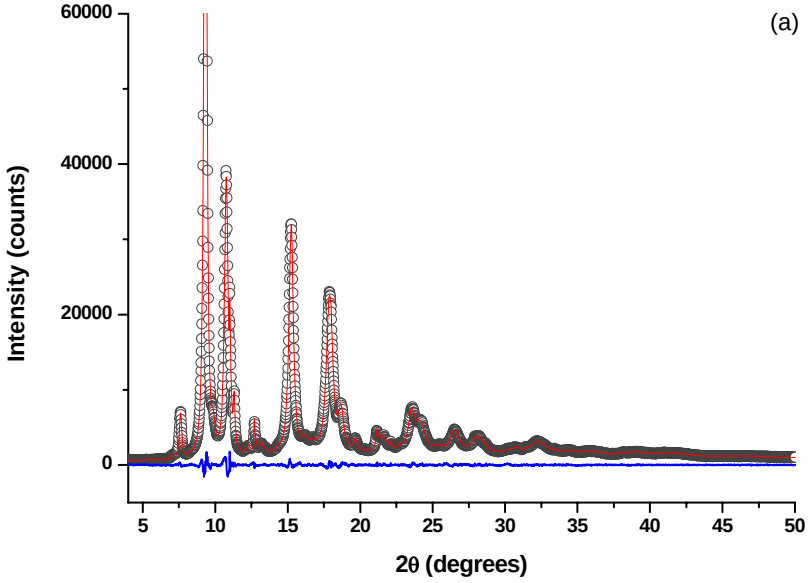

Figure 3. 9 *Synchrotron X-ray data for the P9-40 specimen modelled by WPPM. Data (circle), model (line) and difference between the two (residual, line below).*

The almost flat nature of the residual indicates that all features of the profile have been correctly reproduced. Analogous plots were obtained for all other specimens investigated here.

As expected, milling causes a reduction in the average size of the coherently diffracting domains and a corresponding increase in the quantity of defects (dislocation density). It can be observed a steep variation of those parameters for short milling times (*cf. Figure 3.11*), with a levelling (saturation) of the values starting at 20 min milling time.

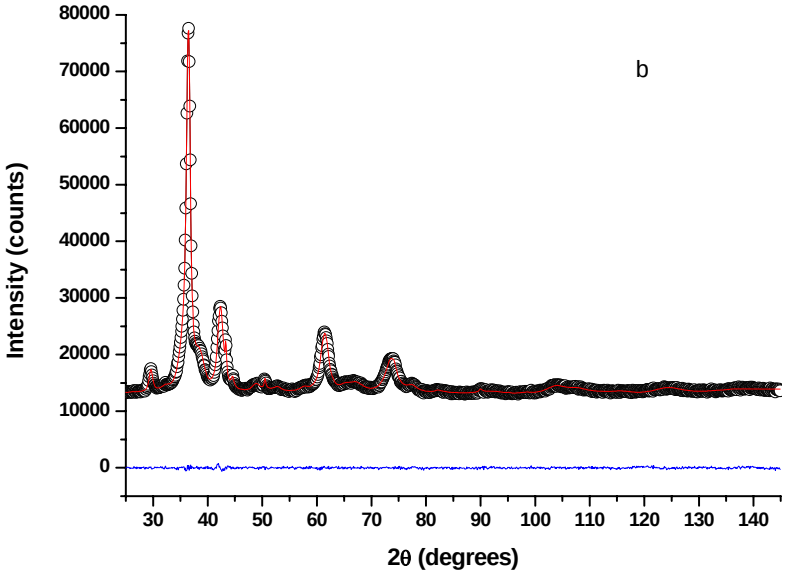

Figure 3. 10. ***Laboratory X-ray data for the P9-40 specimen modelled by WPPM. Data (circle), model (line) and difference between the two (residual, line below).***

It is plausible that the observed phenomenon for shorter milling times corresponds to the formation of dislocation cells (*see Figure 3.12*) as it happens during conventional plastic deformation.

The corresponding increase in the cell parameter (*cf. Figure 3.13*) indicates a pumping of excess volume inside the structure: the levelling after 20 min milling is a clear indicator that a proper nanostructure has been reached.

More informative than the mere average size is certainly the size distribution, shown in *Figure 3.14* for the whole set of powder milled for increasing times. It can be observed a progressive narrowing of the distribution, the variation again saturating at 20 min. This trend is consistent with both SR and Lab

XRD data.

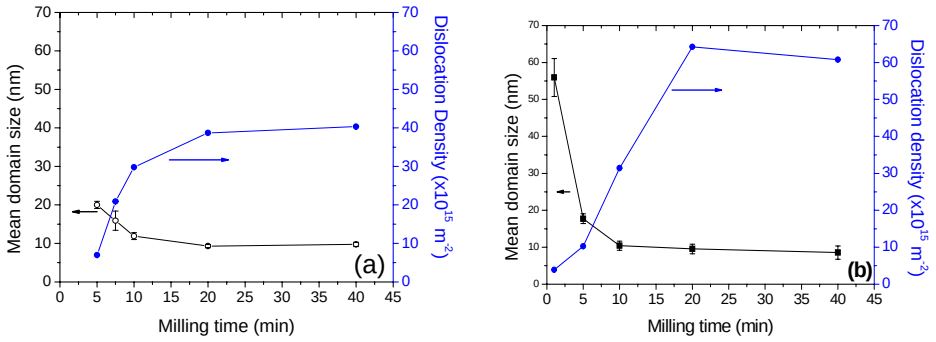

Figure 3. 11. ***Variation of mean domain sizes and dislocation density with milling time. (a) synchrotron radiation XRD data, (b) laboratory XRD data.***

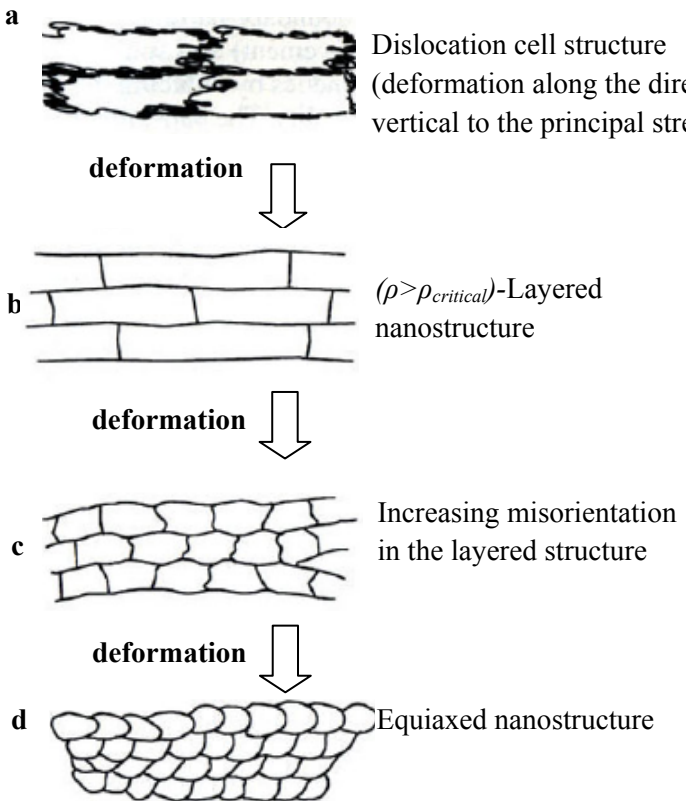

Figure 3. 12. *Schematic drawing of nanocrystalline material formation process by ball milling* [29].

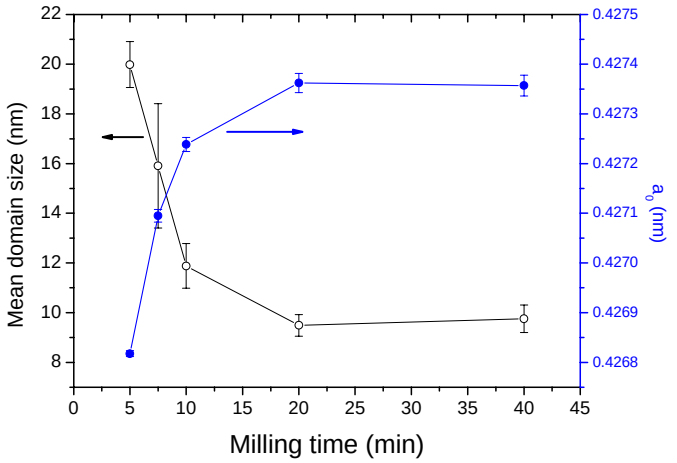

Figure 3. 13. *Variation of cell parameter and mean domain size with milling time.*

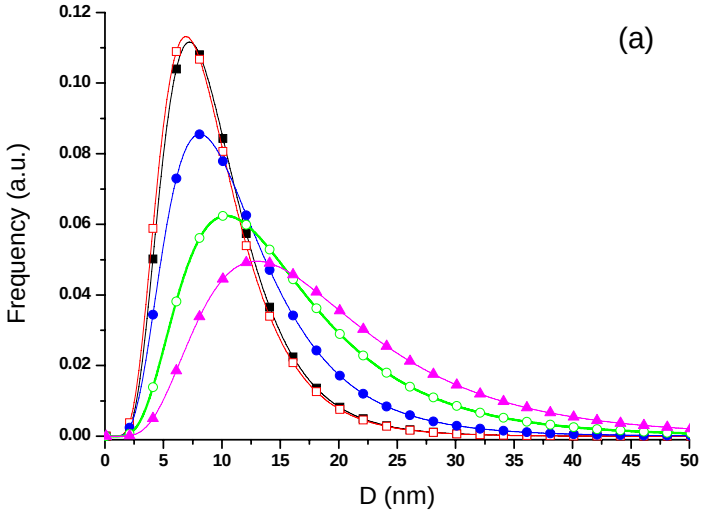

Figure 3. 14. *(a) Lognormal distribution of spherical domains for the various specimens obtained from the WPPM analysis of synchrotron XRD data. Curves correspond to P9-5 (triangles), P9-7.5 (circles), P9-10 (dots), P9-20 (squares), and P9-40 (diamonds).*

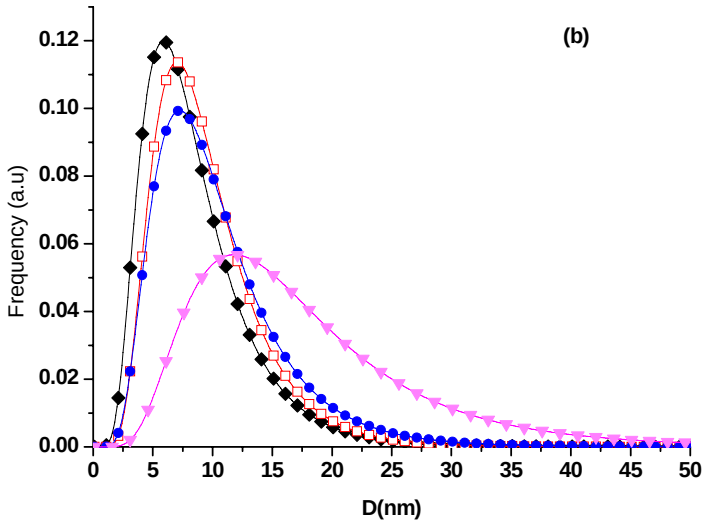

Figure 3.14. *(b) Lognormal distribution of spherical domains for the various specimens obtained from the WPPM analysis of laboratory XRD data. Curves correspond to P9-5 (triangles), P9-7.5 (circles), P9-10 (dots), P9-20 (squares), and P9-40 (diamonds).*

It is interesting to observe also the trend of Wilkens parameter $W = Re\sqrt{\rho}$, related to the dipole character of dislocations. The higher the value of W, the weaker the dipole character and the screening of the displacement fields of dislocations. Lower values of W, (below unity) gives an indication of enhanced interactions of a high density of dislocations at the grain boundaries leading to nanocrystallinity conditions [19, 23]. *Tables 3.2* and *3.3* show again that W saturates for P9-20, further validating the hypothesis that after 20 mins milling time the nanostructure is reached in the powder.

3.3.3 Scanning and Transmission Electron Microscopy

A clear evolution of the powder morphology can be observed by ESEM (*Figure 3.15*). The initial powder is characterized by the presence of sharp fragments of various shapes and sizes.

After a short milling time (e.g., 1 min) it can be clearly observed the coexistence of fine and coarse particles. This can explain the impossibility of getting a proper fit of the XRD data for the P9-1 powder. It is possible that some of the large particles are monocrystalline or composed of a small number of very large domains. Already after 5 minutes of milling, the sharp edges disappear and the small particles start agglomerating over the larger ones. For increasing milling time, a progressive homogenisation of the size and shape of the small particles is observed, with the larger aggregates progressively being formed by large sets of small particles. All morphological observations are compatible with the XRD results. A direct comparison is however not possible, and in any case the observed particle size of the order of 100 nm or more is far larger than the domain size estimated via XRD. This is a clear indication that most of the particles are made of several domains: the milling process contributes to reduce the size of the particles, but also the domain size, with possible introduction of internal grain boundaries.

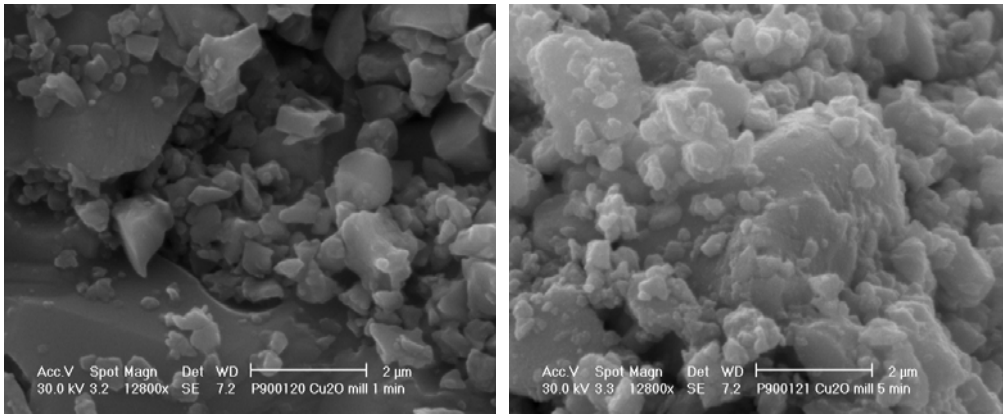

(a) (b)

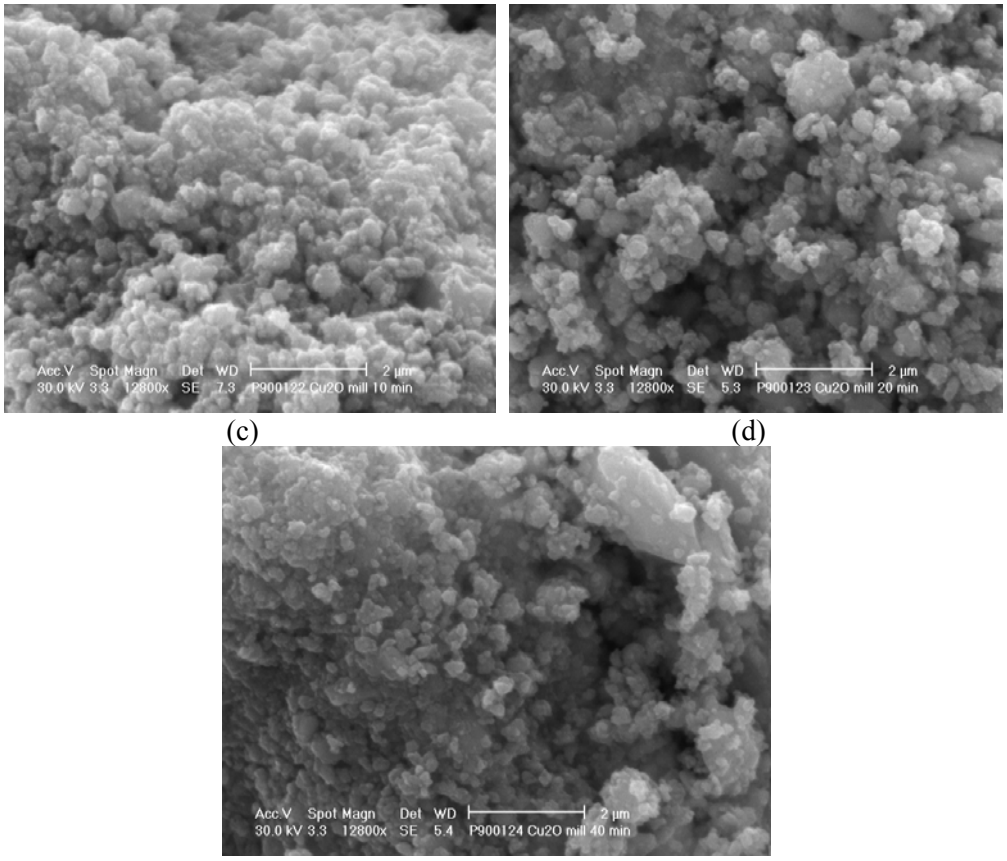

(c) (d)

(e)

Figure 3. 15. ***ESEM micrographs of the powder milled for: (a) 1 min, (b) 5 min, (c) 10 min, (d) 20 min, and (e) 40 min.***

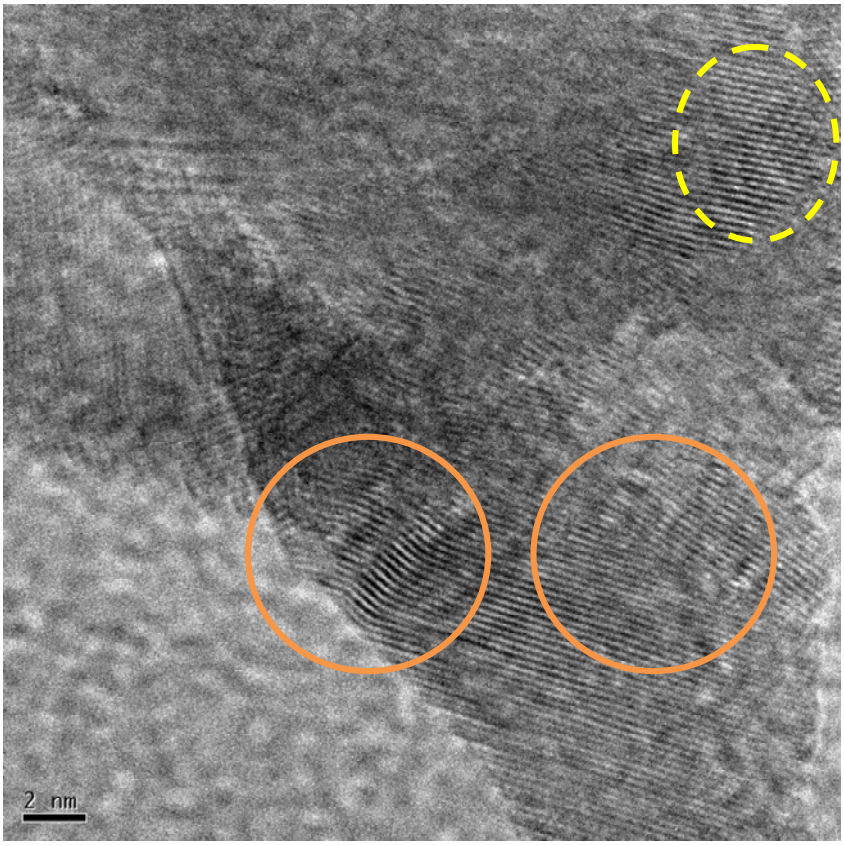

Figure 3. 16 *HRTEM micrograph of the P9-5 specimen. The presence of deformed planes and dislocations, as well as of a possible small angle grain boundary is evidenced by dashed circles.*

A possible validation for the XRD results comes from the TEM investigation. In the present case, given the high density of defects and extensive agglomeration of domains, it is not possible to obtain a size distribution from TEM. It is instead possible, using HRTEM, to observe the presence of defects, quantitatively measured by WPPM of the XRD data. *Figure 3.16* shows, for instance, a HRTEM micrograph of the P9-5 specimen: the distortion of the lattice planes is visible, together with the presence of the traces of dislocations (causing local deformation of the lattice), and the possible presence of small angle grain boundary. All those defects can be caused by the pileup of a large number of

dislocations, and this can justify the large value of the dislocation density observed for this material.

As an Energy Dispersive X-ray Spectroscopy gives unphysical results here (the absolute determination of oxygen in heterogeneous powders like those proposed here is really challenging), it is not possible to identify where CuO and Cu (possibly contaminated by Fe from the milling set) are located.

3.3.4 Thermal Equilibrium phase relations of the Cu_2O-CuO-Cu system.

As powders will be consolidated to form dense solid layers for application purposes, investigating the thermal stability regions of the component phases is important.

The thermal stability of the milled powders was investigated in air under atmospheric conditions. As an example, the Thermogravimetry (TG) and Differential Thermal Analysis result for the P9-5 specimen is shown in figure 3.17.

The Cu-O system has been extensively studied in the literature, but definitive and unique results cannot be found [30, 31, 32]. It seems clear, however, that CuO transforms into Cu_2O in air (partial oxygen pressure of 0.21) at 1031 °C and subsequently melts at 1134°C [33]. Theoretical values indicate that Cu_2O melts at 1235 °C, while Cu melts at 1083.0 °C in air.

The increase of about 7.9 % above 200°C with an enthalpy change of 134.8 J/g corresponds to the Cu_2O to CuO (Cu^+ to Cu^{2+}) transformation. The endothermic effect of CuO - Cu_2O reduction occurs between 560 °C - 1031 °C leading to a weight loss of about 2.6% with a corresponding enthalpy change of ΔH = 135 J/g. The DTA signal at about 1055°C is due to the melting of metallic copper associated with a ΔH of 451 J/g to a weight loss of about 9.7 %. Finally, melting of CuO is indicated by a sharp endothermic peak (ΔH = 158.8 J/g) at about 1140 °C in the DTA plots corresponding to a weight loss of about 0.6 %. It is worth stating

that the weak endothermic peak around 1240 °C could be attributed t the melting of Cu_2O; the signal is too low to be reliable since it is overlapping with the instrumental baseline. In conclusion, the stability regions are in reasonable agreement with the literature data [33].

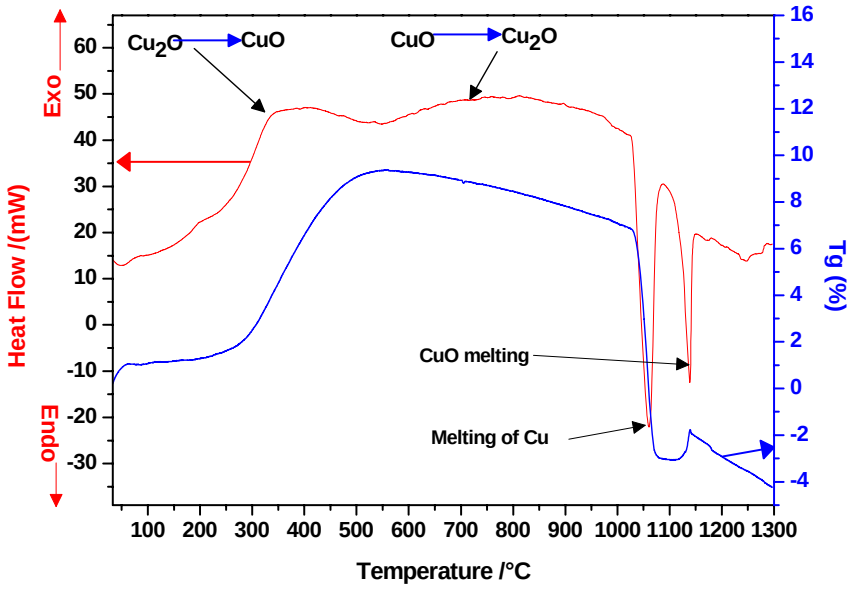

Figure 3. 17. ***TG/DTA curves for the P9-5 milled specimen.***

3.4. CONCLUSIONS

Cuprite powder was milled in a vibrating cup mill suitably modified to work in controlled temperature and atmosphere. The microstructural and thermal stability of the powder kept at -20°C under static air was studied as a function of the milling time.

Laboratory and Synchrotron Radiation X-Ray Diffraction data were collected and the superior quality of the former clearly evidenced, especially in the analysis of the line profile broadening. The latter was analyzed by the Whole

Powder Pattern Modelling (WPPM) algorithm. WPPM provides consistent and detailed quantitative information on the microstructure of the powders in terms of a lognormal distribution of domain sizes and presence of line defects.

For short milling time, work hardening takes place, with a steep decrease in domain size and corresponding increase in dislocation density - possibly at the grain/sub-grain boundaries. This tends to level out after 20 min, when domain size and lattice defects values reach a steady state, indicating that a nanocrystalline state has been achieved. Electron microscopy shows a corresponding increase in the quantity of fragmented and fine particles. Limit values for the grinding of Cu_2O are a mean domain size of ca. 9 nm (with progressively narrower distribution) and a dislocation density of ca. $4x10^{16}$ m^{-2}, the latter particularly high for an oxide. The correlation between dislocation density and domain size suggests that at shorter milling times dislocation cells forms, as in a conventional plastic deformation process. Thermal stability data of the milled powder give suggestions on the temperature range for consolidation whiles keeping the pure Cu_2O phase.

REFERENCES

1 L. Profaizer, "Macinazione meccanica ad alta energia in condizioni di temperatura e atmosfera controllate", *Tesi*, Università degli studi di Trento, Italy, (2005).

2 M. D'Incau, "High Energy Milling in Nanomaterials Technologies: process modelling and optimization", *PhD thesis*. Università degli Studi di Trento, Italy, (2008).

3 P. Scherrer, "Nachr. Ges. Wiss. Göttingen", *Math.-Phys., Kl*., **2**, 98, (1918).

4 J. I. Langford and A. J. C. Wilson: "Scherrer after sixty years: A survey and some new results in the determination of crystallite size". *Journal of Applied Crystallography*, **11,[2]**, 102-113, (1978).

5 P. Scardi and M. Leoni, "Whole Powder Pattern Modelling", *Acta Cryst.*A, **58**, 190-200, (2002).

6 A. Mittiga, E. Salza, F. Sarto, M. Tucci, R. Vasanthi, "Heterojunction solar cell with 2% efficiency based on a Cu_2O substrate", *Appl. Phys. Lett.,* **88,**163502, (2006).

7 S.T. Shishiyanu, T.S. Shishiyanu, O.I. Lupan, "Novel NO_2 gas sensor based on cuprous oxide thin films", *Sensors & Actuators B,***113**,468,(2006).

8 M. Hara, T. Kondo, M. Komoda, S. Ikeda, K. Shinohara, A. Tanaka, J.N. Kondo, K. Domen, "Mechano-catalytic overall water splitting (II) nafion-deposited Cu_2O",*Chem. Commun*.,357, (1998).

9 P.E. de Jongh, D. Vanmaekelbergh, J.J. Kelly, "Cu_2O: A catalyst for the photochemical decomposition of water", *Chem. Commun.,* 1069, (1999).

10 G. Rothenberger, J. Moser, M. Gratzel, N. Serpone, and D. K. Sharma, "Charge carrier trapping and recombination dynamics in small semiconductor particles" *J. Am. Chem. Soc*.;**107[26]** 8054–8059,(1985).

11 D.V. Ragone, “Thermodynamics of Materials”, **vol.1**, MIT series, John Wiley & Sons. Inc, Canada, (1995).

12 J. P. Cline, R. D. Deslattes, J.L. Staudenmann, E. G. Kessler, L. T. Hudson, A. Hennins, and R. W. Cheary, “NIST Certificate (SRM 660a) ,LaB6 ,Line Position and Line Shape Standard for Power Diffraction”, Gaithersburg USA, NIST Standard Reference Materials Program, NIST, USA (2000).

13 G. Caglioti, A. Paoletti and F.P. Ricci, “Choice of collimators for a crystal spectrometer for neutron diffraction”, *Nucl. Instr. and Meth*. **3**, 223, (1958).

14 R. A. Young (editor), “The Rietveld method, International Union of Crystallography”, Oxford University Press, (1993).

15 Diffracplus Topas **V.4,** Bruker AXS GmbH, Karlsruhe, Germany.

16 M. Leoni, T. Confente, and P. Scardi, “PM2K: a flexible program implementing Whole Powder Pattern Modelling”, *Z. Kristallogr. Suppl*. **23**, 249 (2006)

17 P. Scardi, M. Leoni, “Diffraction line profiles from polydisperse crystalline systems”, *Acta Crystallographica,* **A 57**, 604-613, (2001).

18 M. A. Krivoglaz and K. P. Ryaboshapka, “Effect of dislocation distribution correlation on X-ray diffraction by deformed crystals” *Fiz. Met. Metalloved,*.**15**, 18, (1963).

19 M. A. Krivoglaz, “Theory of X-ray and Thermal Neutron Scattering by Real Crystals”, *Plenum*, New York, (1969).

20 M. Wilkens, “Fundamental Aspects of Dislocation Theory”, *Natl. Bur. Stand. Spec. Publ. No. 317*, J. A. Simmons, R. de Wit, R. Bullough, (eds),U.S. GPO, Washington, D.C., **Vol. II**, pp. 1195–1221,(1970)

21 E.J. Mittemeijer and P. Scardi, “Diffraction Analysis of the Microstructure of Materials”, *Springer Series in Materials Science*, **Vol.68**, Springer-Verlag,

Berlin, (2004).

22 T. Ungár, I. Dragomir, Á. Révész, and A. Borbély: "The contrast factors of dislocations in cubic crystals: The dislocation model of strain anisotropy in practice". *J. Appl. Crystallogr.*, **32**, 992, (1999).

23 M.Wilkens, "The Determination of Density and Distribution of Dislocations in Deformed Single Crystals from Broadened X-Ray Diffraction Profiles", *phys.stat.sol. (a)***, 2, 359**, (1970).

24 J. Martinez-Garcia, M. Leoni, and P. Scardi, "Analytical expression for the dislocation contrast factor of the cubic slip-system: application to Cu_2O", *Physical Review B,* **76**, 174117, (2007).

25 M. Leoni, J. Martinez-Garcia, P. Scardi, "Dislocation effects in powder diffraction", *J. Appl. Cryst.,* **40**,719-724, (2007).

26 A. G. Every and A. K. McCurdy, in "Crystal and Solid State Physics", D. F. Nelson, Landolt-Börnstein, (eds), *New Series, group III*, **Vol. 29,** p. 68,(Springer, Berlin, 1992).

27 G. Vagnard and J. Washburn, "Plastic Deformation of Cuprous Oxide", *J. Am. Ceram. Soc.,* **51**, 88, (1968).

28 N.C. Popa, "The (*hkl*) Dependence of Diffraction-Line Broadening Caused by Strain and Size for all Laue Groups in Rietveld Refinement", *J. Appl. Crystallogr.,* **31**, 176, (1998).

29 Y. Xu, Z. G. Liu, M.Umemoto and K. Tsuchiya, "Formation and Annealing Behaviour of Nanocrystalline Ferrite in Fe-0.89C Spheroidite Steel Produced by Ball Milling", *Metallurgical and Materials Transaction A***, 33A,** 2195-2203, (2002).

30 A. M. M. Gadalla and J. White, "Equilibrium Relationships in the System CuO-Cu, O-ZrO," *Trans. Br. Ceram. Soc.,* **65**, 383-90, (1966).

31 H.S. Roberts and F.H. Smyth, “The Copper- Cupric Oxide- Oxygen System,” *J. Am. Chem. Soc.,* **43**, 1061-1079, (1921).

32 V.R. Palkar, P. Ayyub, S. Chattopadhyay, M .Multani. “Size-induced structural transitions in the Cu-O and Ce-O systems”, *Phys Rev B*, **53,** 2167, (1996).

33 J. P. Neumann, T. Zhong, and Y. A. Chang, “The Cu-O (Copper-Oxygen) System,” *Bull. Alloy Phase Diagrams*, **5 [2],** 136-140 (1984).

CHAPTER 4

4. Microemulsion synthesis of CuO nanorod-like structures[3]

ABSTRACT

Copper oxide (CuO) nanorod-like structures made of spherical nanocrystals were synthesized at moderate temperature (80°C) starting from $CuCl_2 \cdot 2H_2O$ crystals in a water/n-heptane microemulsion stabilised by the nonionic Brij-30 surfactant. Whole Powder Pattern Modelling of the X-ray diffraction pattern shows absence of linear and planar defects with crystalline domains in the range of 4 - 8 nm. A linear correlation between the average size of the particles and the quantity of water in the system was observed: all synthesised specimens show a large blue shift of the energy bandgap (up to 2.7 eV versus 1.2 eV of bulk CuO) resulting from quantum confinement effects. The mechanism of growth of the spherical nanoparticles into nanorod-like structures has been elucidated.

4.1. INTRODUCTION

Nanostructured semiconductor materials have stimulated intensive research interest in the recent years due to their unique properties (different from the bulk ones) and the potential applications in photonic and nanoelectronics [1-3]. Synthetic 1-dimensional nanostructures such as e.g. quantum dots, nanorods or nanotubes, are ideal systems for the study of dimensional and morphological dependence of optical, electrical and mechanical properties of final materials [4]. It is believed that nanostructures with dimensions of a few nanometers will have novel and unique physical and chemical properties due to quantum confinement

[3] *Part of the results shown in the present chapter has been included in the manuscript: D. Dodoo-Arhin, M. Leoni, P. Scardi, "Microemulsion synthesis of CuO nanorod-like structures", Materials Science and Engineering: A, 2010 (submitted).*

effects.

High-temperature superconductivity in materials such as copper oxide perovskites [5, 6], has been attributed to a Jahn-Teller distortion in a highly symmetric divalent copper monoxide structure which introduces a strong electron-phonon interaction leading to the superconductivity. The need to understand the origin and mechanism of this phenomenon has led to extensive studies of simple and complex copper oxides [7-9].

Monoclinic cupric oxide CuO (tenorite, space group C2/c, a = 4.6850 Å, b = 3.4230 Å, c = 5.1320 Å, β = 99.52°, ICDD PDF card # 72-0629) is an important p-type transition metal oxide. The material is a direct bandgap semiconductor. It couples a narrow band gap (E_g = 1.2 - 1.8 eV) [10-12] with a set of properties such as high-temperature superconductivity and good photoconductivity and photochemical properties [13]. This largely explains the growth of applications in the last years in the more diverse fields such as solar cells [14], gas sensors [15], field emission (FE) emitters [16], and lithium ion battery electrode materials [17].

The structure of CuO is certainly an exception in the periodic table [18]: all neighbouring oxides (from MnO to NiO), in fact, show the cubic rocksalt structure and are correlated antiferromagnetic (AFM) insulators [19-22]. Cupric oxide, on the contrary, is monoclinic, ferroelectric [18] and recent studies seem to indicate it possesses at least three different magnetic polymorphs [23, 24].

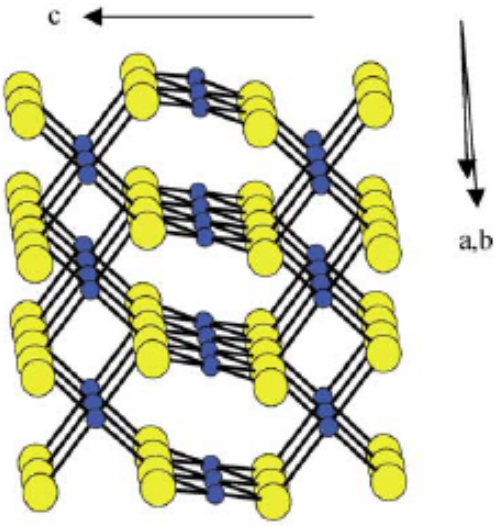

Figure 4. 1. ***Structure of CuO: smaller (blue) spheres represent Cu atoms, larger (yellow) spheres the oxygen atoms [14].***

Size and morphology of copper oxide particles have a strong effect on the optical, semiconducting, and piezoelectric properties of the material. To investigate for those effects and for possible applications, nanostructured copper oxides have been synthesised in several shapes such as nanobelts [25], nanorods [26], nanowires [27], and nanoribbons [28]. Several techniques, ranging from reverse micelles microemulsions [29], electrochemical and sonochemical deposition [30, 31], chemical vapour deposition [32], alcoho-thermal and hydrothermal synthesis [33, 34], thermal decomposition [35] and high-temperature synthesis [36] are available to produce such non-equilibrium morphologies. Self-assembly (e.g. reverse micelle microemulsions) driven e.g. by surface tension, capillary effects, electric and magnetic forces, and hydrophobic interactions, is an effective strategy for forming a wide variety of motifs, otherwise impossible to form under equilibrium conditions [34, 37, 38]. However, precise control over nanocrystalline CuO synthesis remains a big challenge.

The availability of good techniques for the measurement of size and size distribution of crystalline domains is also a critical factor. Techniques such as TEM and XRD Line Profile Analysis usually provide information only about the average

particle size (e.g. Scherrer formula [39] and Williamson-Hall plot [40]) or are limited to the analysis of a small number of particles (TEM). Moreover, TEM analysis may suffer of systematic errors caused by the specimen preparation and by the presence of extensive agglomeration of nanoparticles. The Whole Powder Pattern Modelling (WPPM) of X-ray diffraction data is a possible solution, being at the same time statistically valid (millions of particles sampled), relatively unaffected by specimen preparation issues, and user-independent. The technique provides a complete microstructural information on nano-scale powders based on the direct refinement of physical models on the experimental data, with no arbitrary assumptions on the peak profiles.

In this section of the study, we discuss a thermally mediated single reverse micelle microemulsion method for the preparation of nanorods-like CuO nanocrystals. The analysis of the powders will reveal some insights on the possibility of self assembly of spherical particles into long chains, imparting an overall rod-like shape to the particles.

4.2. EXPERIMENTAL

4.2.1. Materials and specimens

A stable reverse micelle microemulsion was prepared by mixing a non-ionic surfactant (2-dodecoxyethanol, Brij 30) and oil (n-heptane) and then subsequently adding deionised water (<1.8 μS/cm). Batches of 20 ml were made by adding a fixed volume (16.54 %) of surfactant (Brij 30, Sigma Aldrich 98% purity) to n-heptane (Sigma Aldrich, 99% purity) and further adding a varying content of deionised water (1-5%). Table 4.1 identifies the various batches and the corresponding specimens. Each batch was produced at least 3 times to guarantee the reproducibility of the result.

Sample	Brij30®		n-Heptane		$CuCl_2$	NaOH	H_2O	ω	<D>
		equiv.		equiv.			%		nm
	g	ml	g	ml	mg	mg			
CuO-P1	3.144	3.31	11.216	16.49	24.0	50.0	1.0	1.3	4.0(0)
CuO-P2	3.145	3.31	11.075	16.29	25.0	50.0	2.0	2.6	4.5(2)
CuO-P3	3.143	3.31	10.946	16.10	25.0	51.0	3.0	3.8	7.3(2)
CuO-P4	3.145	3.31	10.811	15.90	26.0	52.0	4.0	5.1	7.5(1)
CuO-P5	3.143	3.31	10.674	15.70	25.0	51.0	5.0	6.4	7.6(2)

Table 4. 1. ***Synthesis conditions and average size of as-produced CuO nanocrystals***

An aliquot of 25 mg of $CuCl_2 \cdot 2H_2O$ (Sigma Aldrich, 6174-250GF) crystals was added to each microemulsion and left under magnetic stirring for 10 mins until a sky blue transparent mixture was obtained. 50mg of NaOH crystals were then dissolved into the mixture under constant stirring for about 15 mins. A deep blue microemulsion was obtained without precipitation.

The mixture was then heated at 80°C and kept under gentle stirring at 2 rpm for 3 hours. The mixture gradually changed from deep blue to greenish-blue then to dark brown. The so-formed sol was allowed to cool to room temperature and then added 10 ml acetone (Sigma Aldrich 99% purity) to break the microemulsion.

Particles were subsequently washed with 10 ml ethanol and 20 ml deionised water. For a faster and effective collection, the solution was centrifuged four times at 6000 rpm for 5 mins. No macroscopic agglomeration was observed. Powders were dried at 100°C on (*h*00) Si wafer for XRD analysis.

4.2.2. Characterisation techniques

X-ray powder diffraction (XRD) patterns were collected on a Rigaku 3D-max Bragg-Brentano diffractometer operating with a copper tube (Cu Kα radiation) at 40 kV and 30 mA. The goniometer is equipped with a curved-crystal graphite analyser in the diffracted beam, providing a symmetrical instrumental profile over the investigated range.

Data for all specimens were recorded in the 30 - 70° 2θ range with a step size of 0.1° and a counting time of 20 s per step. Data were analysed using the Whole Powder Pattern Modelling (WPPM) method [41] implemented in the PM2K software [42]. The instrumental resolution function was characterised with the NIST SRM 660a (LaB_6) standard [43, 42]: all peak profiles of the LaB_6 phase were simultaneously fitted with symmetrical pseudo-Voigt functions whose width and shape were constrained according to the Caglioti *et al.* formulae [44].

Transmission electron microscopy was performed on a Philips EM400T electron microscope operated at 120 kV and providing a maximum resolution of 3.0 Å.

Transmission FTIR spectra were recorded on a Nicolet Avatar 550 (Thermo Optics Electron Corporation, Waltham, MA) instrument in the 4000 - 400 cm^{-1} range with 2 cm^{-1} resolution; the Spectrum v5.3.0 software was employed for the FTIR analysis. (Nicolet Avatar 550 FT-IR from Thermo

UV-Vis-NIR was performed on a Varian Cary 5000 spectrophotometer in the range of 300 - 850 nm based on an R928 (PMT) detector with a resolution of 2 nm. The spectrophotometer is equipped with an out-of-plane double Littrow monochromator which minimizes photometric noise and stray light, providing excellent limiting resolution of < 0.045 nm in the UV range and < 0.18 nm in the NIR region. Gratings size of 70x45 mm, blaze angle of 8.5°/10.3°, and blaze wavelength of 250/1192 nm were used for the measurements.

4.3. RESULTS AND DISCUSSION

4.3.1 Synthesis

In aqueous solution, $CuCl_2 \cdot 2H_2O$ dissociates into $[Cu(H_2O)_6]^{2+}$ ions (responsible for the sky blue colouring) and Cl^- anions. Coordination of Cl^- with other Copper ions may partially occur. In the $[Cu(H_2O)_6]^{2+}$ structure, six water molecules completely surround each Cu^{2+} ion, shielding it. Due to the solvating action when copper salt is dissolved in water, four water molecules surround the Cu^{2+} to form a square structure ($Cu(OH)_4^{2-}$), and the other two water molecules locate at its axis. According to the anionic coordination polyhedra theoretical model [45-49], cations exist in the form of complexes whose ligands are OH^- ions in an aqueous solution: the complex whose coordination numbers are equal to that of the crystal formed is called a growth unit. Moreover, the formation of growth units and the incorporation of the growth units into the crystal nucleus are induced by a dehydration reaction. Accordingly, the growth units for CuO nanocrystals are considered to be $Cu(OH)_6^{4-}$, a coordinating octahedron in the NaOH solution. In this case, four OH^- ions are arranged on a planar square, and the other two OH^- ions are located on a perpendicular axis (*see Figure 4.2*).

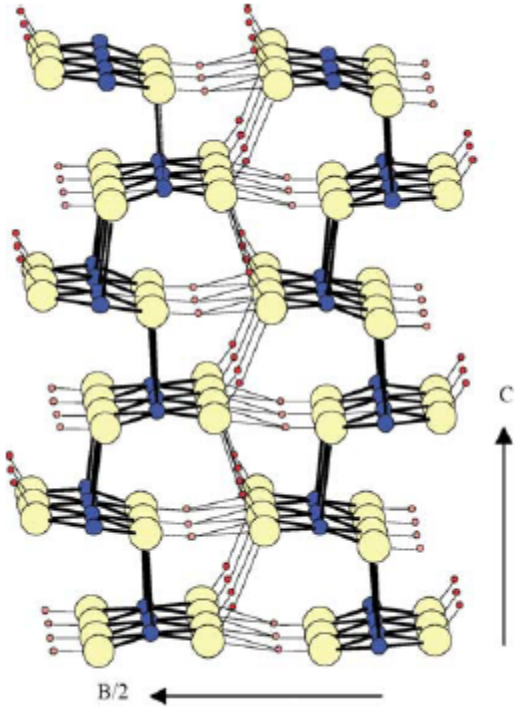

Figure 4. 2. *Crystal structure of the $Cu(OH)_6^{4-}$ complex: small blue spheres are Cu atoms, yellow spheres are oxygen atoms and red sphere are hydrogen atoms [14].*

The binding energies of the two OH^- ions located on the octahedron axis are lower than those of OH^- located on the plane [14]. This means that the two OH^- ions located at the axis are easily replaced and dehydrated to form CuO nanocrystallites, so that the growth rate along the axes is higher than in the plane. The growth mechanism and formation of different shapes of CuO nanocrystals (e.g. nanorods, nanobelts, nanowires, etc) can be explained with this difference in growth rates along various directions. The reaction temperature can play an important role there. More in detail, the reactions leading to the formation of CuO can be summarised into:

$$Cu^{2+}Cl^-(aq)+2Na^+OH^-(aq)\longrightarrow Cu(OH)_2(aq)+2NaCl(aq) \qquad (0.35)$$

$$Cu(OH)_2(aq)+2OH^-(aq)\longrightarrow\left[Cu(OH)_4\right]^{2-}(aq) \qquad (0.36)$$

$$\left[Cu(OH)_4\right]^{2-}(aq) \xrightarrow{heat} CuO_{(s)} + 2OH^-(aq) + H_2O \qquad (0.37)$$

Schematically, the process takes place as in *Figure 4.3*.

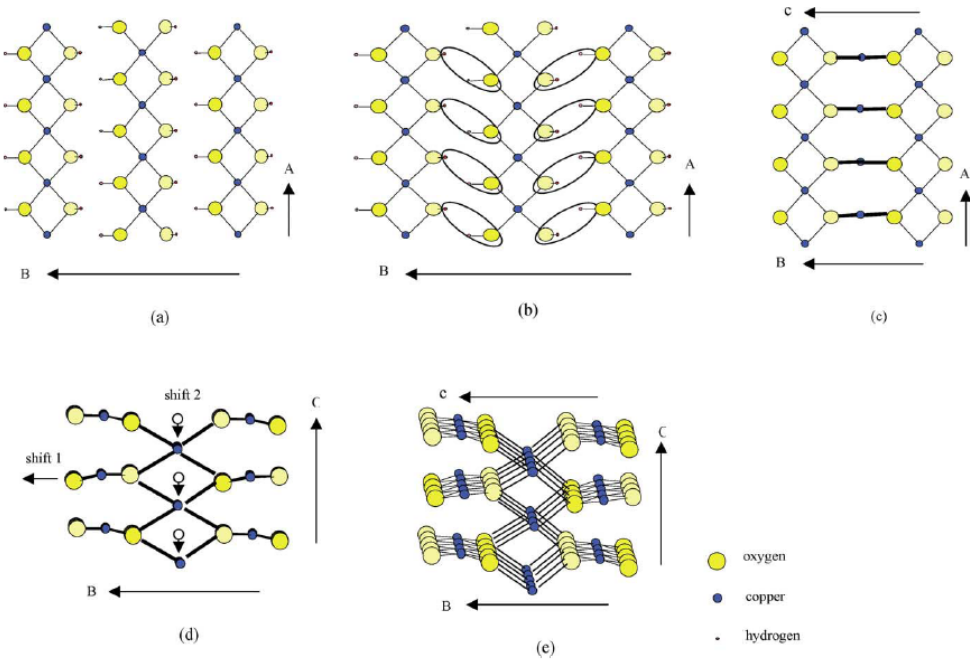

Figure 4. 3. *$Cu(OH)_2$ →CuO transformation process: (a) $Cu(OH)_2$ (A,B)-plane; (b) $Cu(OH_2)$ (A, B)-plane loss of water; (c) CuO (A, B)-plane oxolation process;(d) CuO (B, C)-plane oxolation process, shift 1≈1.4 Å, shift 2: C/4 = 1.3 Å; (e) CuO perspective view [7].*

At low temperatures, the hydroxyl groups of the $Cu(OH)_6^{4-}$ complex (produced on addition of NaOH) might form hydrogen bonds by interconnection: the directional growth would then be inhibited, leading to the formation of irregularly shaped nanocrystals [50-52]. At higher temperatures - close to room temperature (T ≤ 25 °C) - only small quantities of hydrogen bonds are destroyed. The residual hydrogen bonds may still lead to the formation structures with mixed morphologies. When the reaction temperature is increased (25 °C < T < 100 °C), there is a corresponding increase in the nucleation and growth rates as well as the destruction of more hydrogen bonds. In our case, the reaction temperature has been chosen to be 80°C to prevent evaporation of the water and to be lower than the

breaking point temperature of the surfactant. Further investigation on the effect of reaction temperature and time on the particle size, size distribution, morphology and the surfactant breaking point boundary conditions of the Brij 30 will lead to a better understanding of the growth mechanism of the as-produced CuO nanostructures.

In the synthesis, reactions *(0.35)* and *(0.36)* take place within reverse micelles of the microemulsion. The microemulsion droplets (reverse micelles) act as the nanoreactors to produce the dissolved $Cu(OH)_2$ nanocrystals. Based on its structural features and specific interactions of the Cu^{2+} ions with ligands in the solution, $Cu(OH)_2$ tends to form a wire-like structure. This structure has been determined to consist of oblate chains of $Cu(OH)_2$ in the (001) planes and oriented along the [100] direction: a feature characteristic of the square-planar coordinated Cu^{2+} ions [53].

The surfactant molecules adhere to the surface of nanoparticles which serve as a protective layer to prevent and fusion of the droplets as a result of collisions [54,55].

There are two important factors that affect the exchange rate of reverse micelles in microemulsion, namely, the dimer stability and the size of channels between the dimers [56]. The dimer stability, which depends on the intermicellar attractive potential, determines the interdroplet transfer of reactants. On the other hand, the size of channels, which depends on the rigidity of interfacial film in the microemulsion, determines the Ostwald ripening contribution. At lower water content, the interfacial film is more rigid since it is closely surrounded by the surfactant molecules. Hence, the fused dimers formed through droplets collision can disappear rapidly since the film stability is high, and channel for the exchange of reactants is narrower. This results in relatively smaller particle size and narrower size distribution of the resulting nanocrystals [7].

When the water content is increased, there are more free water molecules in the microemulsion and the interfacial rigidity is reduced as compared with that at

lower water content.

4.3.2. X-ray diffraction analysis

The XRD patterns (*Figure 4.4*) show a predominant presence of CuO with traces of $Cu(OH)_2$. This can be a consequence of the existence of residual interconnected hydrogen bonds which were not destroyed during the synthesis stage. The presence of those bonds suggests that reaction time is an important factor in the synthesis of pure CuO crystals.

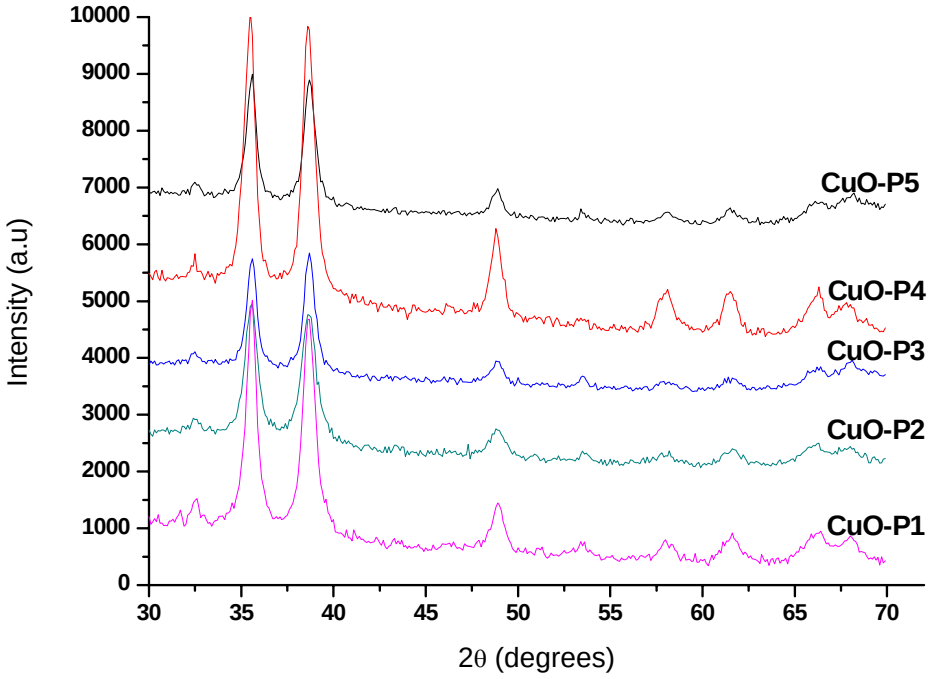

Figure 4. 4. *XRD patterns of as-synthesized CuO nanocrystals.*

The large broadening of the diffraction peaks suggests a very small size of the coherently diffracting domains. Quantitative microstructure analysis was performed using the Whole Powder Pattern Modelling approach, which directly connects a physical model for the microstructure with the diffraction pattern,

allowing an extraction of microstructure parameters without recurring to arbitrary peak shapes to fit each diffraction peak. This is a more realistic alternative to traditional Line Profile Analysis based on the Williamson-Hall or Warren-Averbach methods. As an example, *Figure 4.5* shows the diffraction pattern of CuO-P5 modelled via WPPM; results for the other specimens are analogous. The modelling was done by assuming the presence of a lognormal distribution of spherical domains; analysis results are condensed in *Figure 4.6*.

Although data are quite noisy, the agreement between data and model is rather good, suggesting that the equiaxial shape assumption is correct for the domains investigated here.

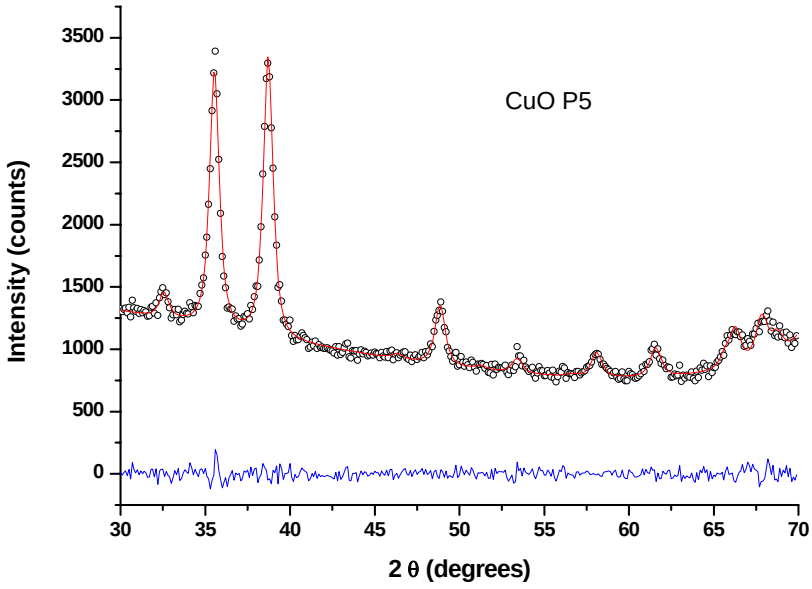

Figure 4. 5. *WPPM result. Data (circle), model (line) and difference between the two (residual, line below) for the P5 specimen*.

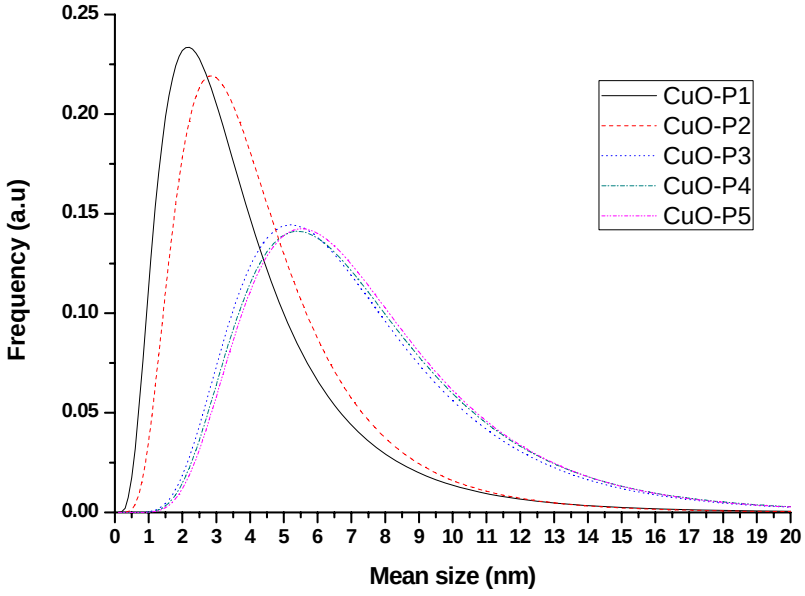

Figure 4. 6. *Lognormal distribution of the whole set of specimens investigated here.*

In order to validate the presence of a lognormal distribution, the WPPM modelling was done again by considering the size distribution being described by an arbitrary histogram, directly modelled to the experimental data. *Figure 4.7* shows the results to be compared with the corresponding lognormal curves proposed in *Figure 4.6*. It can be observed a quite good agreement between the distributions obtained with the lognormal approximation and those obtained here.

Both in the lognormal (analytical) and free histogram (numerical) cases, the mean domain size ranges from ~4 nm (CuO-P1) to ~8 mn (CuO-P5). A clear correlation between domain size and quantity of water inside the micelles can be observed, consistent with the literature relations between the size of the initial nanoreactors and the size of the final particles (see e.g. [57] and references therein).

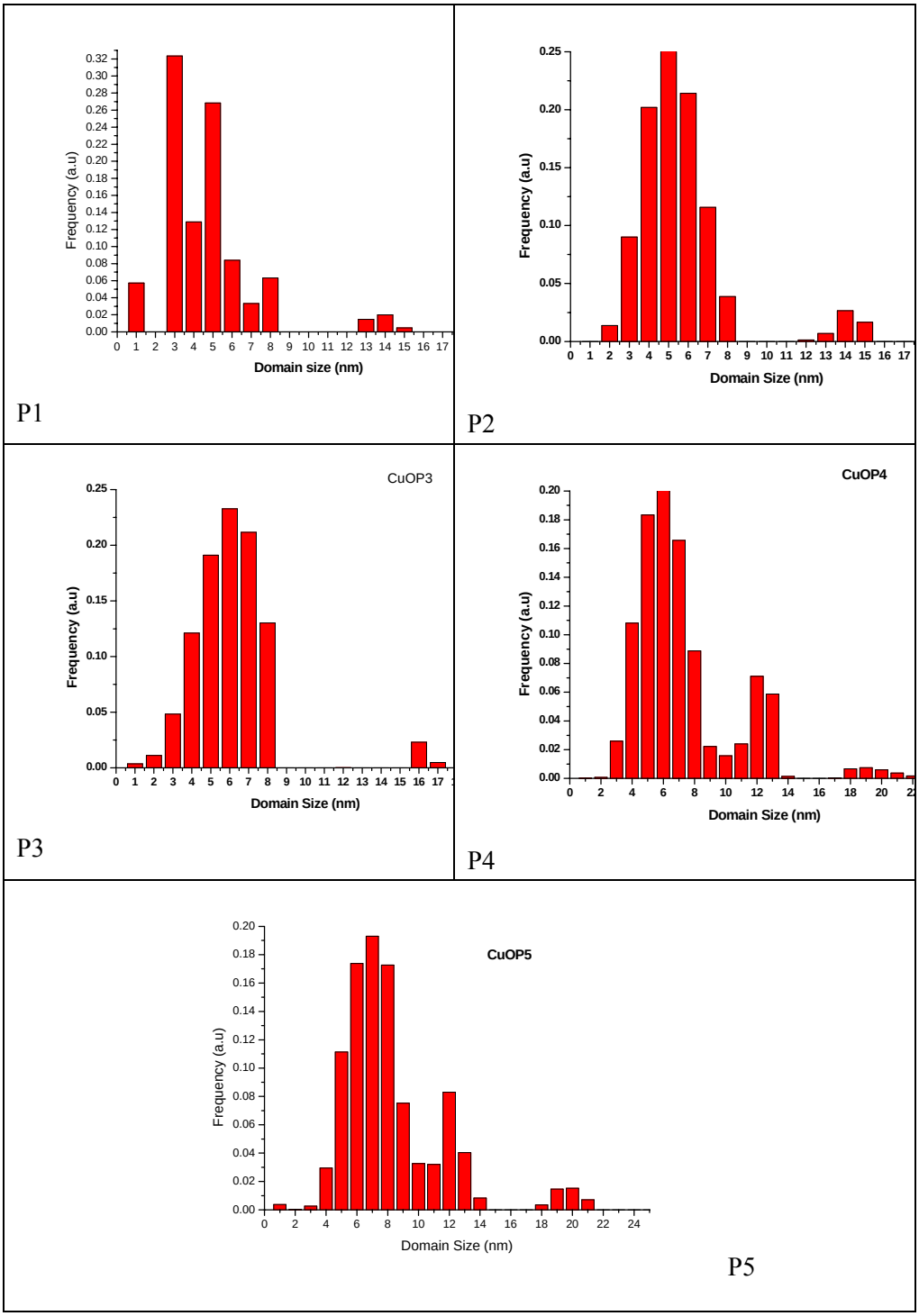

Figure 4. 7. *Histogram size distribution for the whole set of specimens investigated here.*

4.3.3. Transmission Electron Microscopy

The TEM images in (*Figure 4.8*) indicate the synthesis of rod-like nanostructures for all conditions investigated here. From the image of the CuO-P3 specimen (*Figure 4.9*) it appears that the nanorod-like structure is indeed made up of small spherical particles that have been self- aligned to form rods. This is consistent with earlier explanation of the directional growth of CuO nanocrystals along the axis. The size obtained by X-ray diffraction is consistent with the size of the nanoparticles forming the rod-like structures: this is an indication that particles are aligned along the rods but have no crystallographic relationship (i.e. a proper epitaxy did not occur).

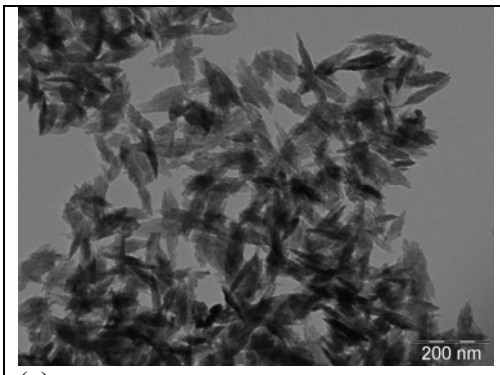

(a)

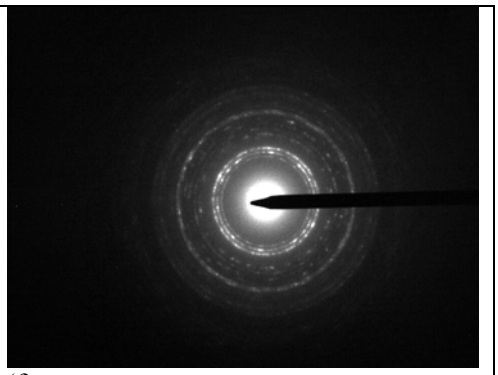

(f)

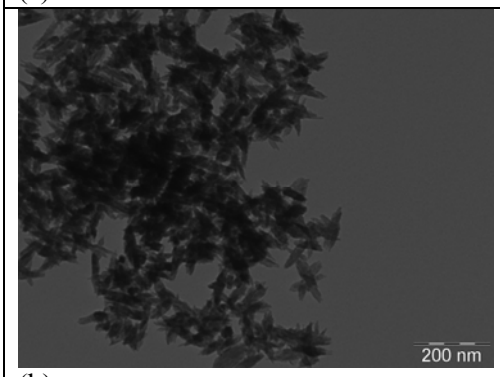

(b)

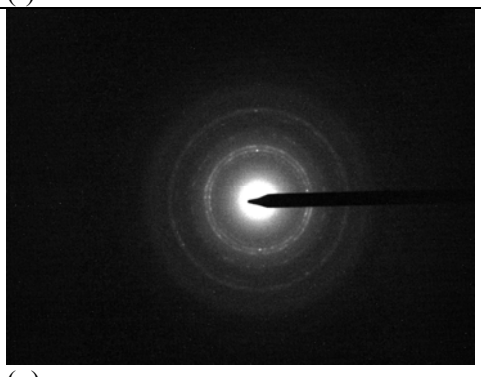

(g)

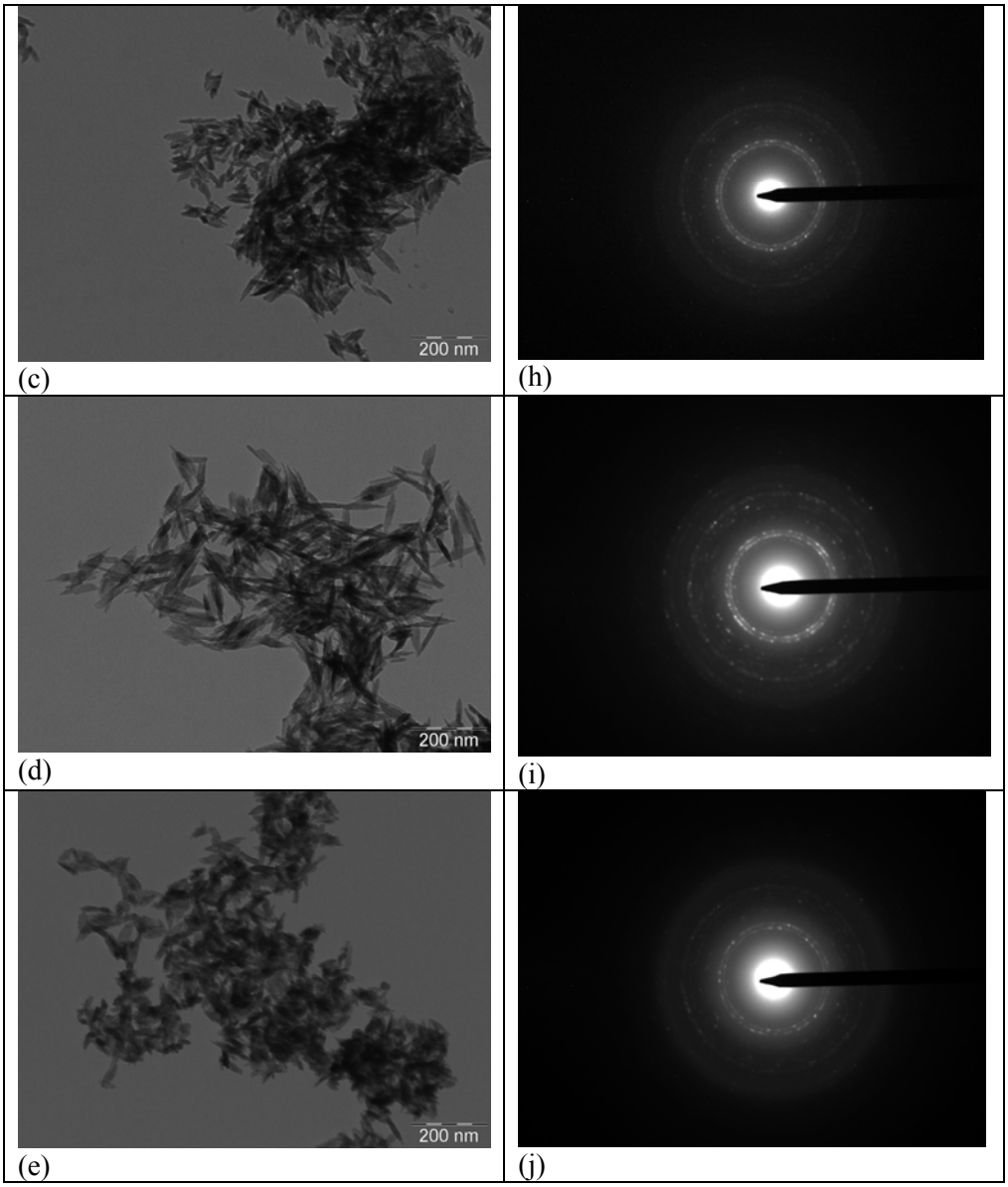

Figure 4. 8. *TEM images of CuO-P1 to CuO-P5 (a-e) and corresponding SAED (f-j).*

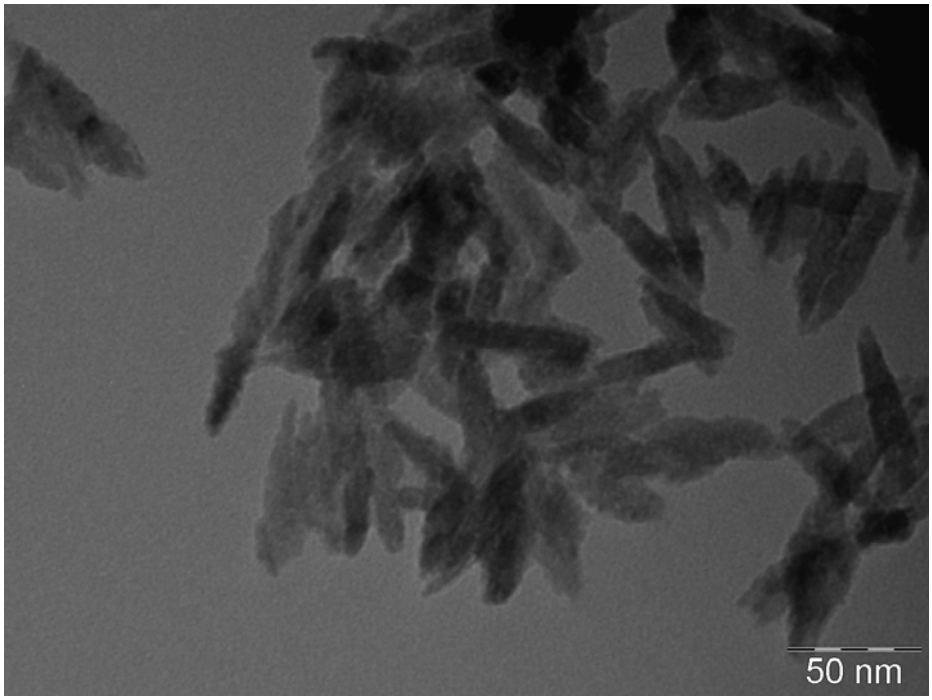

Figure 4. 9 *Image of CuO-P3 specimen showing rod-like structures of spherical particles.*

4.3.4. Fourier-Transform Infrared (FTIR) spectroscopy

FTIR spectroscopy (*Figure 4.10*) has been used to validate the results of the XRD line profile analysis (*cf. Figure 4.1*) and to further check the purity of the prepared CuO nanocrystals. The band at 425 cm^{-1} can be assigned to the Cu-OH stretching mode of residual $Cu(OH)_2$ [58]. The absorption peaks at around 418 cm^{-1}, 536 cm^{-1} and 590 cm^{-1} are due to stretching of the Cu-O bond along the [101] direction [59-61]. The peak at ca. 1632 cm^{-1} is due to the bending vibrations of physically adsorbed water [62] whereas the signature of an OH in-plane bending is at 1257 cm^{-1}.

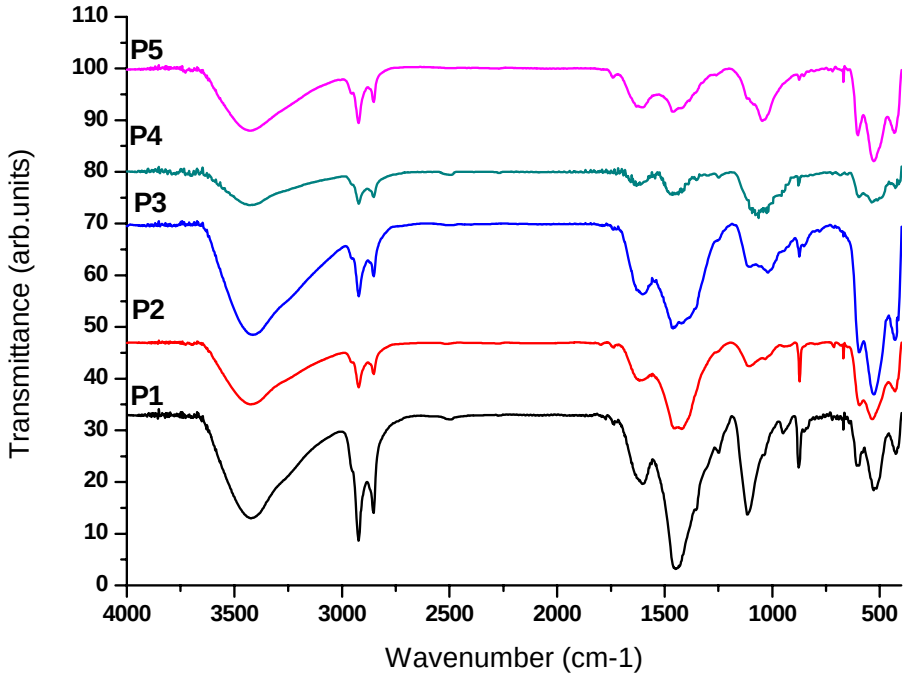

Figure 4. 10. *FTIR spectra of the as-prepared CuO nanocrystals*.

The peak at 1440 cm^{-1} is attributed to CH_2 in-plane bending while that at 725 cm^{-1} is due to CH_2 in-plane rocking. The broad band between 1200 cm^{-1} and 1080 cm^{-1} is due stretching of the C-O bond coordinated to metal cations [63] (Polyoxyethylene bond, present in the head group of Brij 30) and the peak around 668 cm^{-1} is the bending of CO_2. All those signals are a clear signature of the residual presence of the Brij 30 surfactant. The two peaks located around 2851 cm^{-1} and 2921 cm^{-1} are attributed to the CH_2 symmetric stretching and CH_2 asymmetric stretching modes respectively. The shift in position towards higher values (2785 cm^{-1} and 2850 cm^{-1}) could be attributed to the size effect of the particles, whereas the strong presence the O-H stretching band around 3500 - 3200 cm^{-1} is mainly due to water and ethanol residues.

4.3.6. UV-Visible-NIR spectroscopy and Optical energy band gap

Ultraviolet, Visible and Near InfraRed (UV-Vis-NIR) absorption spectroscopy is one of the most widely used techniques to reveal the energy structures and optical properties of a semiconductor. The room temperature spectroscopy of the as-prepared CuO nanoparticles dispersed in pure ethanol allowed us to investigate the excitonic transitions and optical absorption properties of the material. The spectrum is presented in *Figure 4.6*. Though the spectrum seems featureless, there is observable absorption peak centred at about 350 nm and 400 nm. The seemingly featureless nature of the spectrum could be due to increasing scattering by the dispersed particles.

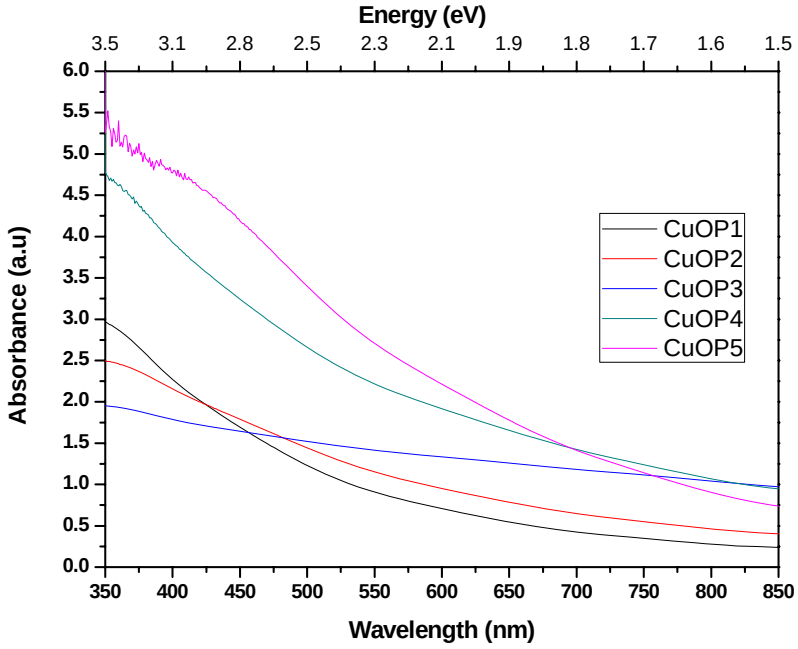

Figure 4. 11. *UV-Vis Spectra for the set of specimens analysed here*.

To better understand the optical and electronic properties of the prepared nanocrystal, the study and estimation of the mean value of the energy bandgap is of paramount importance. Following the classical Tauc approach, the energy band gap of the CuO nanocrystals can be estimated according to the

equations [64, 65];

$$\alpha E_p = k\left(E_p - E_g\right)^n \tag{0.38}$$

$$\alpha h\nu = k\sqrt{h\nu - E_g} \tag{0.39}$$

where α is the absorption coefficient, $E_p = h\nu$ is the incident photon energy, E_g is the optical band gap, h is Planck constant and k is a proportionality constant. The exponential n depends on the type of band-band transition and it goes from ½ for a direct bandgap semiconductor, to 2 for an indirect bandgap one. The value of ½ should therefore be used for CuO.

The absorption coefficient α can be calculated from the Beer-Lambert law expressed in terms of the intensity of the incident light I_0 and the intensity I of the light transmitted through a specimen of thickness l:

$$I = I_0 e^{-\alpha l} \tag{0.40}$$

The ratio between the transmitted and incident intensities can be experimentally measured and converted into the so called absorbance (A), defined as the base 10 logarithm of the reciprocal of the transmittance:

$$A = \log_{10}\frac{I}{I_0} = \log_{10}\frac{1}{T} \tag{0.41}$$

Combining the previous equations the following can be written:

$$\alpha = 2.303\frac{A}{l} \tag{0.42}$$

where l is the path length of the light through the sample, a 1 cm (0.01m) cuvette of square-section.

The bandgap E_g was determined for the various specimens (i.e. increasing ω values as in *Table 4.1*) by extrapolating the straight line of the $(\alpha h\nu)^2$ vs. hν plot to intercept on the horizontal photon energy axis as shown in *Figure 4.6b*. The energy band gap of the as prepared CuO nanocrystals is estimated to be between 2.71eV

and 2.16 eV which is larger than the reported value of bulk CuO (E_g = 1.85eV) [12]. The increase in the band gap of the CuO nanocrystals with the decrease in particle size is attributed to a quantum confinement effect [66].

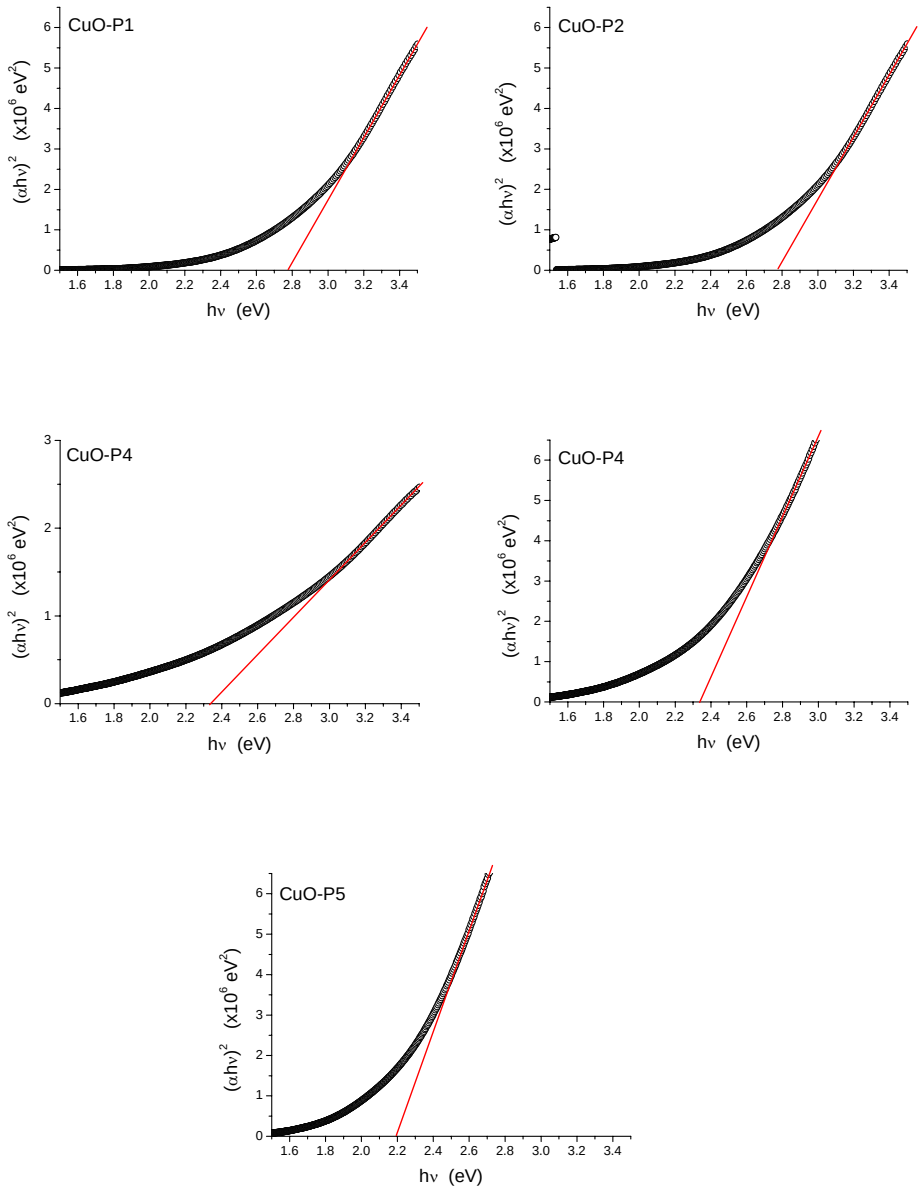

Figure 4. 12. *Plots of $(\alpha h\upsilon)^2$ vs. $h\upsilon$ for the CuO specimens analysed here.*

4.4. CONCLUSIONS

Heptane/water microemulsions stabilised with the non-ionic Brij 30 surfactant were used to produce minimally agglomerated rod-like CuO nanocrystals. TEM shows that the nanorod-like structures consist of well aligned spherical particles of 4-8 nm in diameter. This suggests that reactions occurred in the spherical micelles followed by directional growth along the axes. The increase in the water to surfactant molar ratio causes an increase in both the average domain size and in the width of the size distribution. Heating of the microemulsion is the key to synthesise CuO nanocrystals with a well defined morphology.

REFERENCES

1 A.M. Morales, C. M. Lieber, "A Laser Ablation Method for the Synthesis of Crystalline Semiconductor Nanowires", *Science*, **279**, 208-211, (1998).

2 G. Fasol, "Room-Temperature Blue Gallium Nitride Laser Diode", *Science,* **272**, 1751-1752, (1996).

3 Y. Wu, H. Yan, P. Yang, "Inorganic Semiconductor Nanowires: Rational Growth, Assembly, and Novel Properties", *Chem. A Eur. J.*, **8**, 1260-1268, (2002).

4 P. Yang, H. Yan, S. Mao, R. Russo, J. Johnson, R. Saykally, N. Morris, J. Phan, R. He, and H. J. Choi, *Adv. Funct. Mater.,* **12**, 322, (2002).

5 H. Kamimura, H. Ushio, S. Matsuno, T. Hamada, "Theory of Copper Oxide Superconductors", *Springer-Verlag*, Berlin Heidelberg, (2005).

6 J. Bednorz and K. Muller, "Perovskite-type oxides - the new approach to high-T_c superconductivity", *Rev. Mod. Phys.,* **60**, 585, (1988).

7 D. Hana, H. Yang, C. Zhu and F. Wang, "Controlled synthesis of CuO nanoparticles using TritonX-100-based water-in-oil reverse micelles", *Powder Technology*, **185, [3]**, 286-290, (2008).

8 L. de'Medici, X. Wang, M. Capone and A. J. Millis, "Correlation strength, gaps, and particle-hole asymmetry in high-T_c cuprates: A dynamical mean field study of the three-band copper-oxide model", *Phys. Rev.,* **B 80**, 54501, (2009).

9 E V Antipov, A M Abakumov "Structural design of superconductors based on complex copper oxides," *Phys. Usp.,* **51**, 180, (2008).

10 J. Wang, S. He, Z. Li, X. Jing, M. Zhang, Z. Jiang "Self-assembled CuO nanoarchitectures and their catalytic activity in the thermal decomposition of ammonium perchlorate", *Colloid Polym. Sci.*, **287**,853–858, (2009).

11 G Papadimitropoulos, N Vourdas, V EmVamvakas and D Davazoglou,

"Deposition and characterization of copper oxide thin films", *Journal of Physics: Conference Series*, **10**, 182–185, (2005)

12 H. Wang, J. Z. Xu, J. J. Zhu, H. Y Chen, "Preparation of CuO nanoparticles by microwave irradiation", *J. Cryst. Growth*, **244**, 88, (2002).

13 E. Vigil, B. González, I. Zumeta, C. Domingo, X. Doménech, J. Ayllón, "Preparation of photoelectrodes with spectral response in the visible without applied bias based on photochemically deposited copper oxide inside a porous titanium dioxide film", *Thin Solid Films*, **489**, 50,(2005).

14 A. Sambandam, W. Xiaogang, and Y. Shihe, "Room temperature growth of CuO nanorod arrays on copper and their application as a cathode in dye-sensitized solar cells", *Materials Chemistry and Physics*, **93,** [1],35-40,(2005).

15 A. Chowdhuri, V. Gupta, K. Sreenivas, R. Kumar, S. Mozumdar, P. Patanjali, "Response speed of SnO_2-based H_2S gas sensors with CuO nanoparticles", *Appl. Phys. Lett.*, **884,** 1180, (2004).

16 J. Chen, S. Deng, N. Xu, W. Zhang, X. Wen, S. Yang. "Temperature dependence of field emission from cupric oxide nanobelt films", *Appl.Phys. Lett.*, **83**, 746, (2003).

17 X. Gao, J. Bao, G. Pan, H. Zhu, P. Huang, F. Wu, D. Song., "Preparation and Electrochemical Performance of Polycrystalline and Single Crystalline CuO Nanorods as Anode Materials for Li Ion Battery," *J.Phys. Chem. B.*, **108**, 5547, (2004).

18 W. Siemons, G. Koster, D. H. A. Blank, R. H. Hammond, T. H. Geballe, and M. R. Beasley, "Tetragonal CuO: End member of the 3d transition metal monoxides", *Phys. Rev. B,* **79**, 195122, (2009).

19 W. A. Harrison, "Heisenberg exchange in the magnetic monoxides", *Phys. Rev. B*, **76**, 054417, (2007).

20 L. F. Mattheiss, "Electronic Structure of the 3d Transition-Metal Monoxides.

I. Energy-Band Results", *Phys. Rev. B*, **5**, 290, (1972).

21 K. Terakura, T. Oguchi, A. R. Williams, and J. Kübler, "Band theory of insulating transition-metal monoxides: Band-structure calculations", *Phys.Rev. B,* **30**, 4734, (1984).

22 J. Zaanen and G. A. Sawatzky, "Band gaps and electronic structure of transition-metal compounds", *Phys. Rev. Lett.,* **55**, 418-421, (1985).

23 X. G. Zheng, C. N. Xu, Y. Tomokiyo, E. Tanaka, H. Yamada and Y. Soejima, "Observation of Charge Stripes in Cupric Oxide", *Phys. Rev. Lett.,* **85**, 5170, (2000).

24 D. Prabhakaran, C. Subramanian, S. Balakumar and P. Ramasamy, "Morphology and etching studies on YBCO and CuO single crystal", *Physica C*, **319**, 99, (1999).

25 X. Song, H. Yu, S. Sun, "Single-crystalline CuO nanobelts fabricated by a convenient route", *J. Colloid Interf. Sci.,* **289,** 588, (2006).

26 W. Jisen, Y. Jinkai, S. Jinquan, B. Ying, "Synthesis of copper oxide nanomaterials and the growth mechanism of copper oxide nanorods, *Mater. Des.,* **25**, 625, (2004).

27 M. Kaur, K.P. Muthe, S.K. Despande, S. Choudhury, J.B. Singh, N. Verma, S.K. Gupta, J.V. Yakhmi, "Growth and branching of CuO nanowires by thermal oxidation of copper", *J. Cryst. Growth*, **289**, 670, (2006).

28 C.L. Zhu, C.N. Chen, L.Y. Hao, Y. Hu, Z.Y. Chen, "Template-free synthesis of $Cu_2Cl(OH)_3$ nanoribbons and use as sacrificial template for CuO nanoribbons", *J. Cryst. Growth*, **263**, 473, (2004).

29 J. Rockenberger, E C Scher and A P Alivisatos, "A new nonhydrolytic single-precursor approach to of transition metal oxides", *J. Am. Chem. Soc.,* **121**, 11595-11596, (1999)

30 L. Wang, G. Cheng, X. Jiang, S. Wang, X. Zhang, and Z. Du, "Modulating the

surface states of electric field assembled CuO nanowires by electrochemical deposition method", *Appl. Phys. Lett.,* **95**, 083107 (2009)

31 R V Kumar, Y. Diamant and A. Gendanken, Sonochemical Synthesis and Characterization of Nanometer-Size Transition Metal Oxides from Metal Acetates, 2000 Chem. Mater. 12 2301

32 D. Barreca, E. Comini, A. Gasparotto, C. Maccato, C. Sadad, G. Sberveglieri and E. Tondello "Chemical vapour deposition of copper oxide films and entangled quasi-1D nanoarchitectures as innovative gas sensors", *Sensors and Actuators B: Chemical,* **141, [1]**, 270-275, (2009).

33 Z-S Hong, Y. Cao and J-F. Deng, "A convenient alcohothermal approach for low temperature synthesis of CuO nanoparticles", *Mater. Lett.,* **52** 34, 2002

34 M.A. Dar , Q. Ahsanulhaq , Y.S. Kim , J.M. Sohn , W.B. Kim , H.S. Shin, "Versatile synthesis of rectangular shaped nanobat-like CuO nanostructures by hydrothermal method; structural properties and growth mechanism", *Applied Surface Science*, **2556**, 279–6284, (2009)

35 C. Carel, M .Mouallem-Bahout and J.C Gaude, "Re-examination of the non-stoichiometry and defect structure of copper(II) oxide or tenorite, Cu1±zO or CuO1±ε: A short review", *Solid State Ion.,* **117**,47, (1999)

36 C.T. Hsieh, J.M. Chen, H.H. Lin, H.C. Shih, "Synthesis of well-ordered CuO nanofibers by a self-catalytic growth mechanism", *Appl. Phys. Lett.*, **82**, 3316, (2003).

37 B. Liu, H.C. Zeng, "Mesoscale Organization of CuO Nanoribbons: Formation of "Dandelions", *J. Am. Chem. Soc.,* **126**, 16744, (2004).

38 Y. Xu, D. Chen, X. Jiao, "Fabrication of Malachite with a Hierarchical Sphere-like Architecture", *J. Phys. Chem. B*, **109,** 13561, (2005).

39 P. Scherrer, "Nachr. Ges. Wiss. Göttingen", *Math.-Phys., Kl*., **2**, 98, (1918).

40 G.K. Williamson, W.H. Hall, "X-ray line broadening from filed aluminium

and wolfram," *Acta Metall.*, **1**, 22-31, (1953).

41 P. Scardi and M. Leoni, "Whole powder pattern modelling", *Acta Cryst.*, **A58**, 190-200, (2002)

42 M. Leoni, T. Confente, and P. Scardi, "PM2K: a flexible program implementing Whole Powder Pattern Modelling", *Z. Kristallogr. Suppl.*, **23**,249, (2006)

43 J.P. Cline, R. D. Deslattes, J.-L. Staudenmann, E. G. Kessler, L.T. Hudson, A. Hennins, and R. W. Cheary, "NIST Certificate, (SRM 660a) Line Position and Line Shape Standard for Power Diffraction", Gaithersburg USA, NIST *Standard Reference Materials Program*, NIST, USA (2000)

44 G. Caglioti, A. Paoletti and F.P. Ricci, "Choice of collimators for a crystal spectrometer for neutron diffraction", *Nucl. Instr. and Meth.* , **3**, 223, (1958).

45 W.J. Li, E.W. Shi, W.Z. Zhong, Z.W. Yin, "Growth mechanism and growth habit of oxide crystals", *J. Cryst. Growth*, 203, 186, (1999).

46 W.J. Li, E.W. Shi, W.Z. Zhong, Y.Q. Zheng, Z.W. Yin, "Synthesis of yttria-stabilized zirconia nanoparticles by heating of alcohol-aqueous salt solutions,", *J. Chin. Ceram. Soc.,* **27**, 164, (1999).

47 W.Z. Zhong, G.Z. Liu, E.W. Shi, S.K. Hua, D.Y. Tang, Q.L. Zhao, "Growth habits and mechanism of ZnO microcrystallites under hydrothermal conditions" (in Chinese), *J Chin Ceram Soc China*, ,**25**, 223-229,(1997).

48 E.W. Shi, W.Z. Zhong, S.K. Hua, R.L. Yuan, B.G. Wang, C.T. Xia, W.J. Li, "On the negative ion polyhedron coordination growth model", *Sci. Chin. Ser. E*, **28**, 37-45,(1998).

49 X. Zhang, Y. Xie, F. Xu, X.H. Liu, D. Xu, "Shape-controlled synthesis of submicro-sized cuprous oxide octahedral", *Inorg. Chem. Commun.,* **6**, 1390-1392, (2003).

50 H. Cano, N. Gabas, J.P. Canselier, "Experimental study on the ibuprofen

crystal growth morphology in solution", *J. Cryst. Growth*, **224**, 335, (2001).

51 Z. Zhou, Q. Zhang, "Crystal transformation and characterization of ibuprofen crystal", *Chin. J. Spectrosc. Lab.*, **23**, 212-215, (2006).

52 Y.G. Sun, Y.N. Xia, "Large-Scale Synthesis of Uniform Silver Nanowires through a Soft, Self-Seeding, Polyol Process", *Adv. Mater.*, **14**, 833-837, (2002).

53 H.R. Oswald, A. Reiler, H.W. Schmalle, and F. Dubler, "Structure of Copper(II)hydroxide", *Acta Crystallogr., Sect. C*, **46**, 2279, (1990).

54 H. Weller, H. M. Schmidt, U. Koch, A. Fojtik, S. Baral, A. Henglein, W. Kunath and, K. Weiss, E. Dieman , "Photochemistry of colloidal semiconductors. Onset of light absorption as a function of size of extremely small CdS particles", *Chem. Phys. Lett.*, **124**, 557-560, (1986).

55 A. Manna, T. Imae, T. Yogo, K. Aoi, M. Okazaki, "Synthesis of Gold Nanoparticles in a Winsor II Type Microemulsion and Their Characterization" *J. Colloid and Interface Sci.*, **256,** 297,(2002).

56 S.Quintillán, C. Tojo, M.C. Blanco, M.A. López-Quintela, "Effects of the intermicellar exchange on the size control of nanoparticles synthesized in microemulsions," *Langmuir*, **17**, 7251-7254,(2001).

57 J. Solla Gullon, "Characterizacion y comportamiento electroquimico de nanoparticulas metalicas preparadas en microemulsion". *Universidad de Alicante*, (2003).

58 R. A. Nyquist, R. O Kagel, "Infrared spectra of inorganic compounds".1st ed., *Academic Press,* New York and London, 220, (1971).

59 G. F Zou, H Li, D.Zhang, W.; Xiong, K.; Dong, C.; Y. T Qian. "Well-Aligned Arrays of CuO Nanoplatelets", *J. Phys. Chem. B*, **110**, 1632, (2006).

60 K. Kliche, Z. V Popovic, "Far-infrared spectroscopic investigations on CuO," *Phys. Rev. B*, **42**, 10060, (1990).

61 B. Balamurunga, B.R. Mehta, "Optical and structural properties of nanocrystalline copper oxide thin films prepared by activated reactive evaporation", *Thin Solid Films,* **396,** 90-96,(2001).

62 A.S. Arico, V.Baglio, A. Di Blasi, V. Antonucci, "FTIR spectroscopic investigation of inorganic fillers for composite DMFC membranes, *electrochemical communications,* **5**, 862-866, (2003).

63 A. Bernson, J. Lindgren, W. Huang, R. Frech, "Coordination and conformation in PEO, PEGM and PEG systems containing lithium or lanthanum triflate", *Polymer*, **36**, 4471, (1995).

64 T.S. Moss, "Optical Properties of Semiconductors", *Butterworth*, London, (1959)

65 S Tsunekawa, T Fukuda, A Kasuya, "Blue shift in ultraviolet absorption spectra of monodisperse CeO_{2-x} nanoparticles", *J. Appl. Phys.*, **87**,1318,(2000).

66 J. P Yang, F. C Meldrum, J. H Fendler, "Epitaxial Growth of Size-Quantized Cadmium Sulfide Crystals under Arachidic Acid Monolayers", *J. Phys. Chem.*, **99,** 5500, (1995)

CHAPTER 5

5. Photonics inks based on copper oxide[4]

ABSTRACT

A set of Cu_2O-based inks for photonics applications have been developed using cost effective techniques. A single-stage procedure based on planetary ball milling allowed the production of a sprayable slurry containing Cu_2O nanoparticles of 5 - 23nm average diameter that can be effectively sintered at temperatures as low as 300 °C. The films show a good uniformity and a low roughness, and optical spectroscopy indicates a good response to light in the visible range.

5.1. INTRODUCTION

The sun is a limitless source of energy: if harvested this energy could be put to use in the most diverse technological applications. The radiation from the sun can be considered as a black body radiation (≈ 5600 K) which is emitted from a number of different surface temperature layers capable of absorbing and emitting different wavelengths. This means that the solar energy that reaches the earth comes with different wavelengths. The energy that one would expect from a perfect blackbody radiation at the mean earth-sun distance with that actually reaching the earth's atmosphere and the ground is shown in the energy distributions plot in *Figure 5.1*. The intensity of light from the sun at different wavelength is called AM0 spectrum (AM standing for Air Mass) while that in the earth's atmosphere depending on conditions is either AM1 (equator) or AM 1.5 (central Europe).

Ideally much of the energy can be harvested; however, existing solar energy harvesting mechanisms (photonic devices) are quite expensive and are rarely capable of competing with traditional fossil fuel sources. The world energy crises of the 1970's, fostered the research of alternative sources of energy to sustain the

[4] A paper on this part of the thesis is currently in preparation.

world in times of crises. These quests for alternative sources led to the development of new photonic devices and to the use of solar energy harvesting mechanism such as solar cells (photovoltaic cells) for commercial purposes.

Solar cells today belong to one of three main generations, with a direct influence on the photovoltaic industry. The first generation - the largest in the industry (80%) - comprises silicon based cells. Those cells have reached their maturity with an efficiency of the order of 20 % but their manufacturing process involves high costs.

The second generation solar cells are the so called thin-film solar cells. They are somehow cheaper to produce (much less material necessary), they are quite flexible, but they are characterised by a lower efficiency with respect to silicon devices.

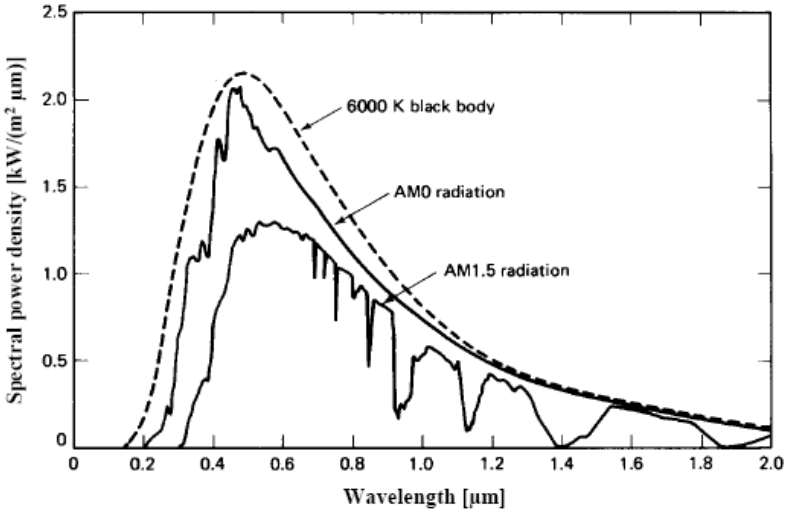

Figure 5. 1. *Solar irradiance spectra: comparison between the blackbody radiation at 6000K, the extraterrestrial spectrum (AM0) and the AM1 radiation [1].*

The third generation is the current state of the art. It includes technologies and devices that are basically non-silicon based such as dye sensitized, polymer and nanocrystalline materials based cells. These technologies are still at the

laboratory stage, hoping to penetrate the market. The trend for efficiencies in terms of development and generation is shown in *Figure 5.2*.

The emerging field of printed electronics using photonic inks promises to create a wide range of consumable electronic and optoelectronic devices, many of which will be manufactured in very high volumes and very low cost including third generation solar cells and gas sensors. The ability to directly print these devices using well known printing techniques (roll-to-roll, screen printing etc) can lower the cost of production, the consumption of materials and the environmental impact. Light-absorbing inks can be directly printed or painted onto inexpensive plastic, glass or flexible surfaces to form multilayers without wasting materials; this may lead to the realization of low cost flexible printable solar cells.

Nanocrystalline semiconductor particles have in recent years drawn considerable interest because of their unique properties; the large surface-to-volume ratio and the quantum confinement effect cause the appearance of special optical and electronic properties, in most cases different from those shown by the bulk counterpart [2-4].

With the current state of research on the use of nano-optoelectronic technologies, the use of nanocrystalline semiconductors to form absorbent layers is imperative. Most importantly, to increase the conversion efficiency as well as reducing solar cell cost, the use of nanostructured materials is of paramount importance. This is because, it is known that, for randomly generated charge carriers, the average diffusion time from the bulk to the surface is given by $\tau = r^2/\pi^2 D$, where, r is the grain radius and D is the diffusion coefficient of the carrier [5]. Hence when the grains radius is reduced from the micron to the nanometer scale, the opportunities for recombination can be dramatically reduced thereby improving the performance of the as-prepared device.

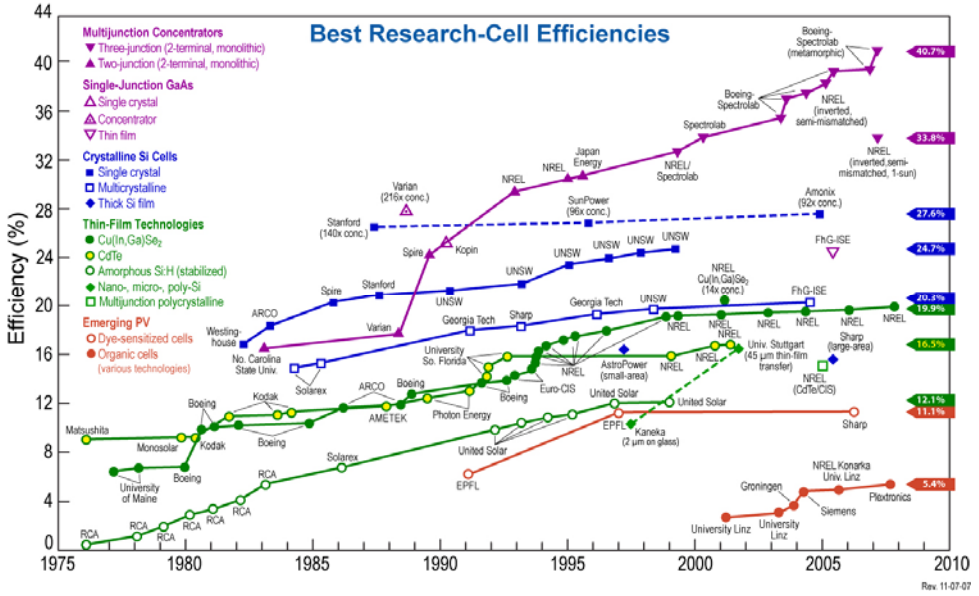

Figure 5. 2. *Research trends of solar cell efficiencies* [6].

Semiconductor nanoparticle ink utilization is now at the cutting edge of technology, making them promising precursors for the production of low cost printable solar cells and gas sensors. In recent times, films of semiconductor nanocrystals produced by spin coating, dip coating, or inkjet printing of nanocrystal colloids (inks), have attracted much attention due to their potential to reduce the manufacturing cost for large-area electronic and optoelectronic devices [7,8].

However, one of the initial obstacles to the widespread utilization of these nanocrystals semiconductor films was their poor electrical conductance caused by the presence of ligands used during synthesis [9]. Those ligands, in fact, limit the electronic coupling between the nanocrystals in the photonic device [10, 11]. However, recently techniques have been proposed that successfully overcome this hurdle through cross-linking with conjugated ligands, electrochemical charging [12-14], engineering of the interparticle distance [15] or exploiting synergistic effects in binary nanocrystal superlattices [16].

Most of these exciting developments have been limited to chalcogenide semiconductors such as CdSe and PbSe, for which colloidal synthesis methods are well established. However, from the point of view of environmental health and safety, abundance and cost of the materials and presence of a technology infrastructure, the availability of stable inks of less toxic materials would be desirable. Copper oxides (Cu_2O and CuO) are promising replacement candidates. They are in fact relatively non-toxic p-type semiconductors with a direct band gap of 2.1eV and 1.2eV respectively. It has been reported that excitons can propagate coherently through single crystalline Cu_2O; it is possible to convert photons into excitons, which then travel through small apertures or small dimension waveguides with little loss by scattering or diffraction. At the end of the path, the excitons can be converted back into photons [17].

The development of copper oxide inks, however, has so far been hampered possibly due to the lack of efficient routes to form stable aqueous colloidal solutions of copper oxide nanocrystals without the usual phase transformation. In this work we present a preliminary study on the production of Cu_2O inks showing a low sintering temperature for applications in solar energy conversion.

5.2. EXPERIMENTAL

5.2.1 Ink preparation

One of the major problems in producing devices based either on Cu_2O particles or inks lies in the difficulty to achieve a perfect and uniform compaction of the powder. To get a uniform and compact layer, temperatures up to 1200°C (approximately the melting temperature of Cu_2O) are necessary. Those high temperatures could be impossible to withstand for a solar cell fabrication, as usually low-melting-point substrates are used. This is the case for instance of aluminium whose melting point is 660 °C, soda-lime glass showing a glass transition temperature as low as 600 °C, or polymeric films that can withstand a

few hundred degrees centigrade. In the present case, soda-lime glass coated with a conductive indium doped tin oxide layer was used as substrate.

It is known from the literature that using nanostructured materials, sintering can be achieved at temperatures and pressures lower than those necessary for coarse powders. This trick will be used here: powders will be produced both via a top-down and a bottom-up technique. Milling is here employed to reduce the size of a coarse powder (top-down) and as a means of defect engineering to improve the sintering ability of the material (IA inks in the following). Nanocrystalline powders previously produced via microemulsions (bottom-up, *see Chapter 3*) will be alternatively used (IB inks).

Being the few available recipes for the production of solar inks unknown (they are covered by patents that just give a hint on the composition), a series of preliminary tests was conducted to explore the various possibilities available to produce a stable ink of pure cuprite (Cu_2O).

A first test was made using a two-stages procedure for inks production: in a first stage powders are produced and in a second one, an ink was made out of the powders. Powders were initially dry ground in a low-energy vibratory mill and then mixed with alcohol, Brij 30 or ethylene glycol in a mortar to obtain a slurry (*figure 5.3a*). Due to the type of grinding, leading to highly non-uniform powders, all those inks failed in providing smooth layers. A better situation can be obtained by using a higher energy ball mill. A Pulverisette P4 planetary ball mill (*figure 5.3b*) was employed to produce a second test set of inks. Finer powders were obtained; however the powder contained both metallic copper and iron, the latter coming from the steel balls and bowl. Copper and iron are deleterious for the solar cell as they can cause short circuits. The situation did not improve when a vibrating cup mill (Fritsch Pulverisette P9) was used in place of the planetary one. The major problems were identified in both cases as the heat developed during dry milling (due to the dry sliding) and the difficulty in dispersing the powder partly

aggregated by the mill.

A single-stage method was then developed, involving a wet milling of the powders in a suitable solvent, directly leading to the formation of the ink. A new set of inks (IA) was then produced this way. Approximately 1.0 g of heat treated bulk Cu_2O powder (heat treatment discussed in *Chapter 3*) was put into an 80 ml martensitic steel bowl with 25 steel balls each with a diameter of 12 mm and a weight of 7.0 g. In succession, 7 ml ethanol, 3 ml ethylene glycol and 0.4 ml polyethylene glycol (PEG 600) were added. The ethylene glycol lowers the vapour pressure of ethanol and acts as a dispersant whereas the polyethylene glycol acts as binding agent. Milling was performed on a Fritsch Pulverisette P4 planetary ball mill using W=200, w/Ω=-2.6 and working in batch cycles of 1 h followed by a pause of 30 min necessary to thermalise the system. Effective milling times of 1, 5, 10, 20 and 40 h were employed. The corresponding inks are identified as IA-P4-1 through IA-P4-40 where the last number in the code identify the milling time. The planetary mill was chosen over the vibrating cup mill as it is less severe. In wet conditions it is important to have a reduction of size without a high increase in temperature to avoid the dynamic annealing of the powder and the denaturation of the ink components.

The resulting slurry is shown in *Figure 5.3c* inside the mill bowl. The apparent separation between alcohol and powder, visible in the inks prepared with the two stages procedure, does not occur here. Inks produced with the two stages method contains a rather high amount of particles and seems stable in time. The various inks obtained via milling are shown in *Figure 5.3d.*

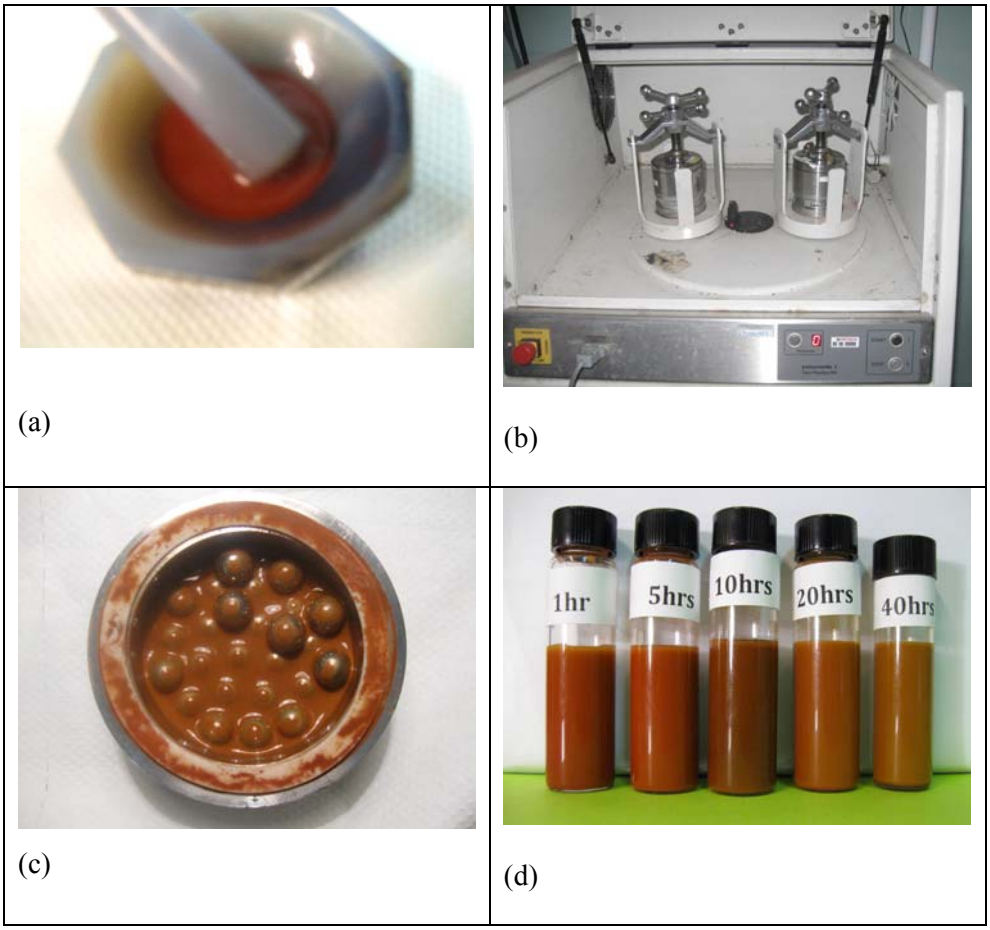

Figure 5. 3. *Ink processing;(a) preliminary testing using mortar grinding set, (b) production using the Fritsch Pulverisette P4 planetary mill (c) ink, balls and vial (d) inks produced at different grinding times (IA-P1-1 to IA-P1-40).*

Various ink deposition methods were employed on various substrates (glass, silicon wafer and gold- coated silicon wafers). These include drop casting and spin coating.

As-produced inks were spread and dried at 70°C on a Si (*h*00) sample holder for XRD analysis. The X-ray diffraction measurement were performed on a Rigaku PMG-VH diffractometer (*figure 5.4*) operated at 40 kV and 30 mA. The machine is equipped with a secondary crystal analyzer and an optical setup consisting of 1° divergence slit, 2° Soller slit, 1° antiscatter slit, 2° secondary Soller slits, and a 0.15

mm receiving slit. This set-up provides a narrow and symmetrical instrumental profile for 2θ>20°. High quality data was obtained by collecting the patterns in step scan mode from 25° to 145°, with a step size of 0.1° and a fixed acquisition time of 60 s per point. The instrumental profile was determined by measuring the NIST line profile standard SRM 660a (LaB_6) [18] as explained earlier in the thesis.

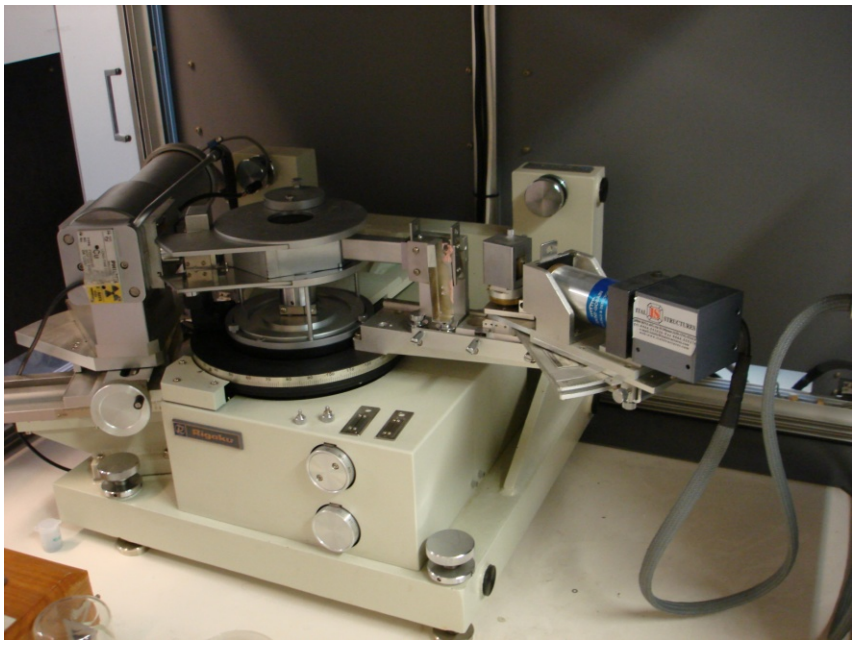

Figure 5. 4. *Rigaku PMG/VH powder diffractometer.*

The morphology of the powders was studied with a FEI XL30 Environmental Scanning Electron Microscope (ESEM) equipped with an Energy Dispersive X-ray Spectroscopy system (EDAX FALCON) based on a nitrogen-cooled Si-Li detector (*see Figure 5.5*). Observations were made at 20 kV in ESEM mode and under a partial water pressure of 0.8 Torr. Under those conditions the powders could be spread on a graphite holder and observed with no need for metallization.

Figure 5. 5. *FEI XL30 ESEM equipped with the EDAX EDS detector.*

Atomic Force Microscopy (AFM) was employed to investigate the surface uniformity and roughness of the deposits. The Solver P-47H AFM instrument shown in *figure 5.6* was used.

Figure 5. 6. *Solver P-47H Atomic Force Microscope.*

A Varian Cary 5000 spectrophotometer based on an R928 (PMT) detector (resolution of 2 nm) was used to perform UV-VIS-NIR spectroscopy in the range of 300 nm – 850 nm. The instrument is shown in figure 5.7.

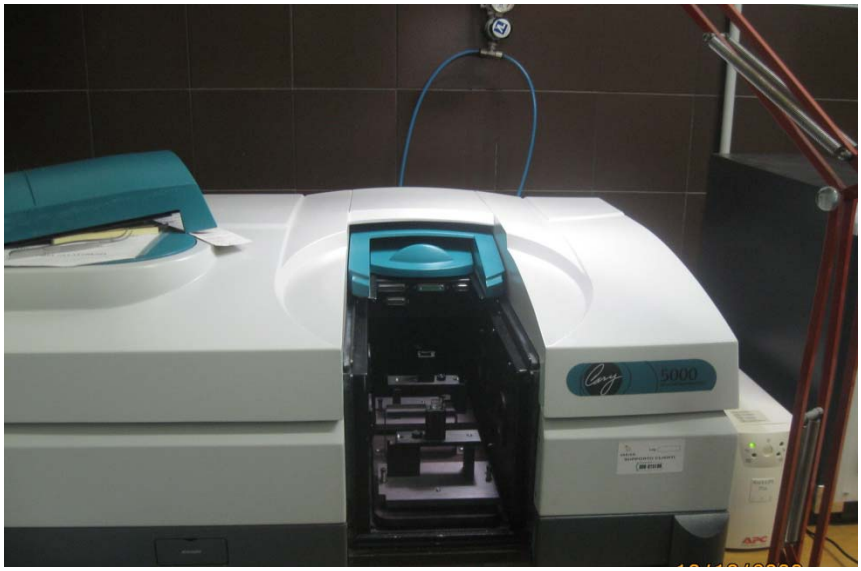

Figure 5. 7. *Varian Cary 5000 UV-Vis-NIR spectrophotometer.*

Thermal analysis was performed on the dry ink using a TG-DTA Setaram apparatus (*see Figure 5.8*) equipped with a LABSYS TG-ATD 1600°C rod. The specimens were subjected to a linear heating ramp from 30°C to 1300°C at 10°C/min and were then cooled at 50°C/min.

Figure 5. 8. *Setaram TG-DTA/DSC instrument.*

5.2.2 Deposition of Inks on substrates

Spin-coating was obtained with a SCS 8 Desk-Top Precision Spin-Coating System Model P-6708D (*figure 5.9*). After deposition the films were dried at about 80 °C for 1 h, and held at this temperature for 5 h in air. This was done to allow adhesion of another coating layer. For each specimen, the deposition and annealing treatment were repeated 3 times in order to get an overall thickness of about 3 µm.

Figure 5. 9. *Spin-Coating System Model P-6708D and sample with ink.*

Another approach to create films was the drop casting. A single drop of ink from a pipette is placed at the centre of a masked substrate; the drop spreads to

cover the entire surface. The film and substrate is allowed to dry in air for about 30 min at a temperature of about 50 - 60°C. The risk of phase transformation in air is limited in view of the fact that the polymer (ethylene glycol) behaves as capping agent preventing contact with air. It is worth stating further that the ink is non-aqueous. The quality of the films produced via drop casting is sensibly lower than that of the films produced via spin coating. Films produced with the latter were therefore chosen for further testing.

Thermal analysis data indicates that cuprite is stable in a temperature range between ca. 200 and 850°C. Sintering of the films produced using the inks were then tried in this interval. Ink particles were observed to sinter on both the glass and the silicon substrates already at temperatures as low as 350 – 400 °C. Formation of smooth film has been achieved using powders milled for 40 h (IA-P4-40). This is due to the fine nature of the ink particles. Earlier test did not result in smooth layers which are attributed to the coarse nature of the particles. Figure 5.10 shows the various layers that have been produced via spin coating. This variation is also observed in the SEM data presented in Figure 5.13.

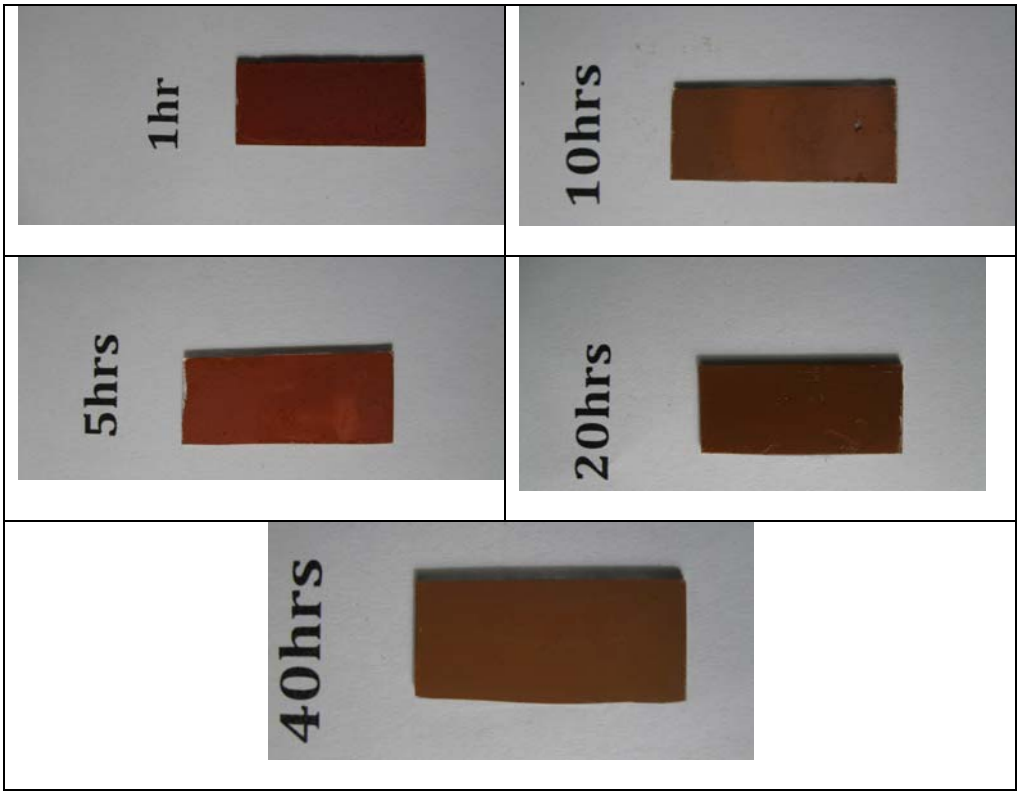

Figure 5. 10. *Specimens obtained by deposition of the IA set of inks. The corresponding milling time is indicated in the figure*.

5.3.RESULTS AND DISCUSSION

5.3.1. XRD and WPPM Analysis

The diffraction patterns of the dried IA set of inks are shown in figure 5.11. Broadening of the peaks increasing with the milling time is evident. The patterns were modelled using the WPPM approach to extract microstructure information assuming domains being spherical and distributed according to a lognormal function, and assuming the presence of dislocations As witnessed by the residue (difference between raw data and modelling) plotted below each pattern in *figure 5.11*, the modelling is excellent. Figure 5.12 shows that even the very small details in the pattern are taken into account by the WPPM. The model parameters obtained for the various powders are shown in Table 5.1.

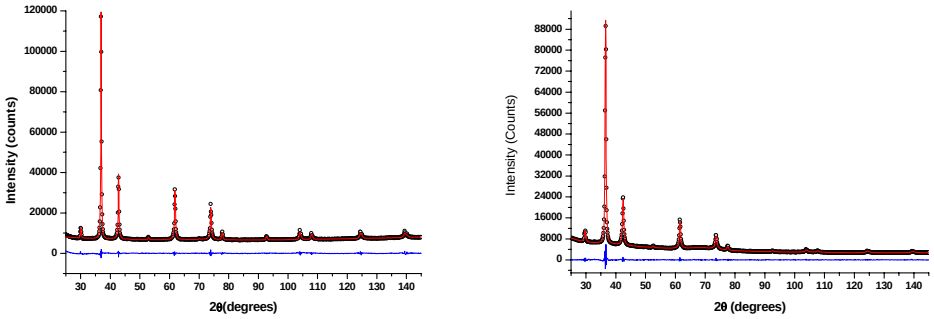

IA-P4-1

IA-P4-5

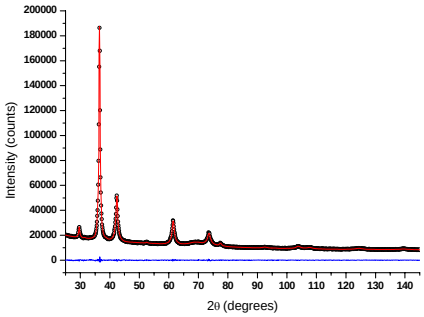

IA-P4-10

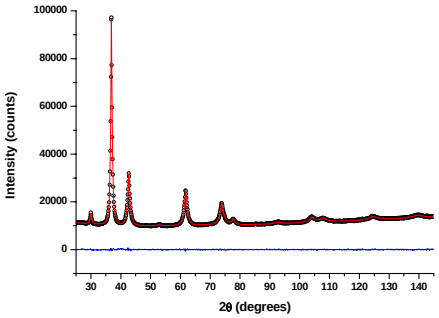

IA-P4-20

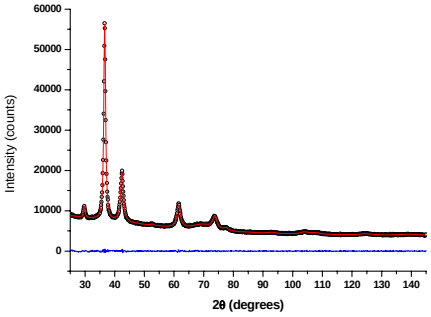

IA-P4-40

Figure 5. 11. *Patterns of the IA-P4-1 to IA-P4-40 dried inks. The experimental data (dots) are shown together with the WPPM calculation (line) and the corresponding residual (line below).*

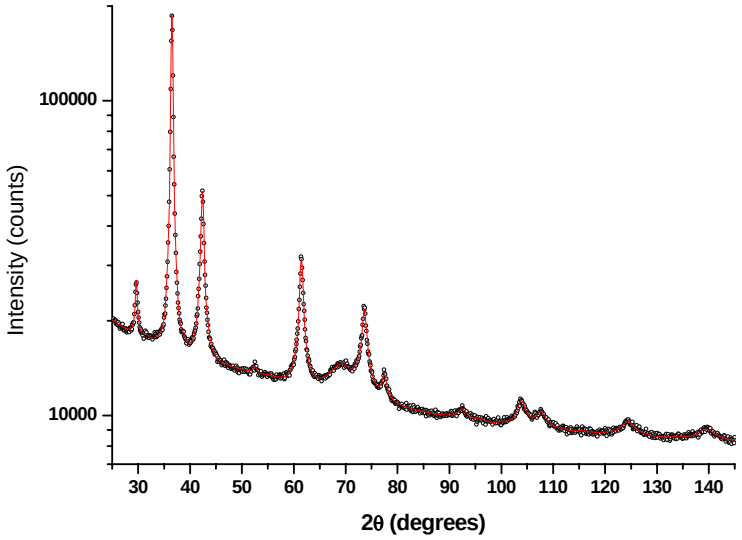

Figure 5. 12 *Logarithm plot of the WPPM result for the IA-P4-40 ink (cf. Figure 5.11) witnessing the quality of the modelling of tails and small peaks. All features in the pattern seem properly taken into account by the model.*

The lognormal size distribution for the various inks is shown in Figure 5.13. As shown in Table 5.1, the average domain size reduces from 22 nm (IA-P4-1) down to 6 nm for the specimen milled 40 h.

Specimen	Size (nm)	Dislocation density ($x10^{16}m^{-1}$)	Cell Parameter a_0 (Å)
IA-P4-1	22(1)	1.2(5)	4.26859
IA-P4-5	18(1)	1.3(5)	4.26826
IA-P4-10	12(3)	22(2)	4.27032
IA-P4-20	9(3)	57(3)	4.27101
IA-P4-40	6(2)	79(1)	4.27246

Table 5. 1. *WPPM results for the IA set of inks*

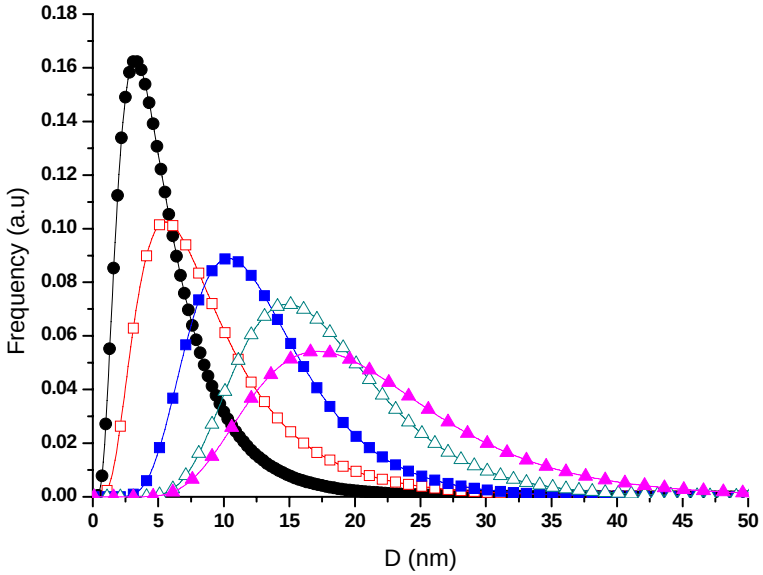

Figure 5. 13. *Lognormal distribution of spherical domains for the various specimens: IA-P4-1 (triangles), IA-P4-5 (open triangles), IA-P4-10 (squares), IA-P4-20 (open squares), IA-P4-40 (dots).*

5.2.2. Thermal Analysis

Obtaining a dense and continuous film (showing i.e. no pores) is especially important in the fabrication of solar cells. The existence of pores, in fact, could lead to short circuiting when multilayers are created, e.g. when the absorbing film is sandwiched in between two electrodes. A further issue in the case of cuprite, is the need to produce a single-phase film: as already mentioned, transformation of Cu_2O into either tenorite (CuO) or metallic copper, can be obtained if the sintering conditions are not properly chosen.

Thermal analysis was then conducted on the various inks in order to identify the suitable treatment ranges in which a pure cuprite phase can be retained. Both Differential Thermal Analysis (DTA) and ThermoGravimetric Analysis (TG or

TGA) were applied in the study of phase transition and thermal stability of dried inks used in this thesis.

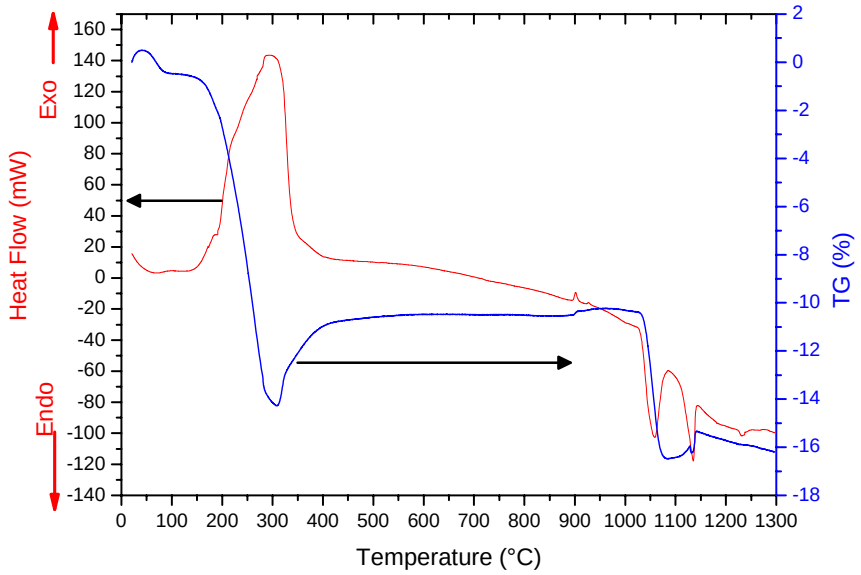

Figure 5. 14. TG/*DTA of the IA-P4-40 Cu_2O ink*

As an example, *figure 5.12* shows the TG/DTA plots obtained from the air dried IA-P4-40 ink. The other inks show a similar behaviour. An exothermic effect is observed around 297°C with enthalpy change of ca. -369 J/g and mass loss of 13.4 % that can be attributed to the burning of the organic phases (additives) used in the ink preparation. The exothermal peak is followed by the endothermic transformation of Cu_2O into CuO (Cu^+ to Cu^{2+} oxidation) with enthalpy change of 669 J/g. Exothermic conversion of CuO back to Cu_2O is observed with an enthalpy change of -362 J/g in the 435 - 889°C range. A further transformation of Cu_2O to CuO (endothermic) is observed in the range 892 - 911 °C accompanied by an enthalpy change of ca. 3 J/g. When the temperature is increased to about 1030 °C, an endothermic transition of CuO to Cu metallic is observed with an enthalpy change of 33 J/g. At around 1057 °C, a deep exothermic effect is present with

enthalpy change of -12.9 J/g and mass loss of 5.8 % is attributed to the melting of metallic copper. Metallic copper is converted back to CuO starting at ca. 1110 °C, with corresponding enthalpy change of -7 J/g and the process ends with the CuO melting at ca. 1137 °C with an enthalpy change of -4.8 J/g. Finally, the weak endothermic peak located around 1237°C with a corresponding mass loss could be attributed to the melting of Cuprite (Cu_2O).

5.2.3 Scanning Electron Microscopy

The morphology of the ink particles was analysed using an Environmental Scanning Electron Microscope (ESEM). Figure 5.13 shows the micrographs of the films obtained by sintering the IA set of inks. The IA-P4-1 ink shows the presence of large particles and the presence of some sharp edges: it is possible that short milling is insufficient to reach a high level of homogeneity in the powder. It can also be seen that the best uniformity of the surface and reduced level of roughness is obtained when the ink with the smaller particles is employed, i.e. for the IA-P4-40 ink.

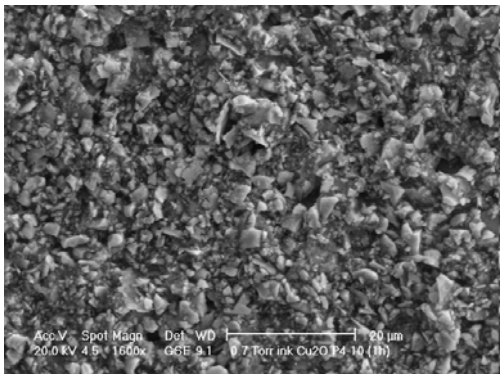

IA-P4-1

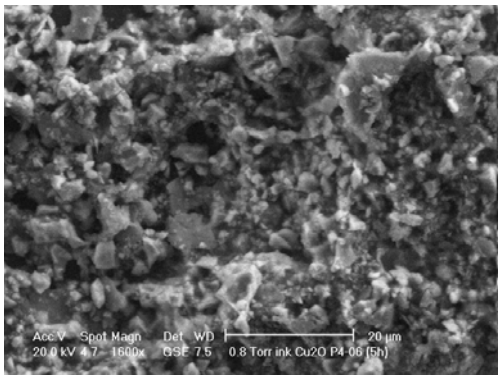

IA-P4-5

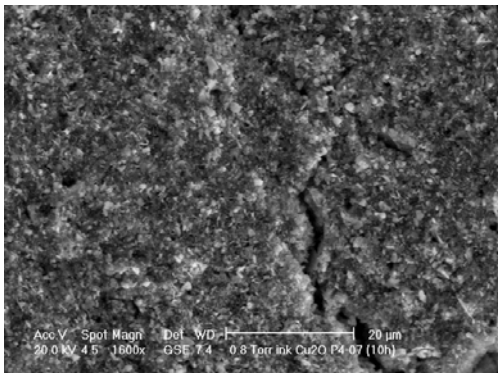

IA-P4-10

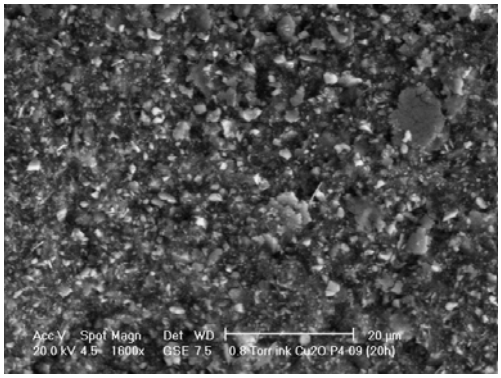

IA-P4-20

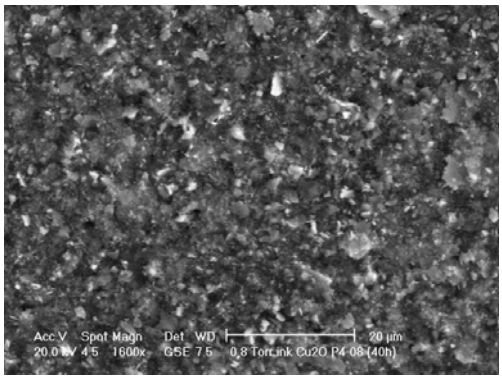

IA-P4-40

Figure 5. 15. *ESEM micrographs of the various inks*.

5.2.4. Atomic Force Microscopy

To quantify and better study the surface roughness of the as-deposited inks layers, the topographic images obtained with a Solver P-47H AFM were employed. Figures *5.14* and *5.15* show the topography of the films obtained by spin coating the IA-P4-40 ink onto the ITO-coated glass substrate and sintered at 200°C and 400°C, respectively. The roughness is quite uniform on the whole surface and it seems slightly influenced by the sintering temperature. The sintering treatment therefore causes just the compaction of the film, with limited growth of the particles.

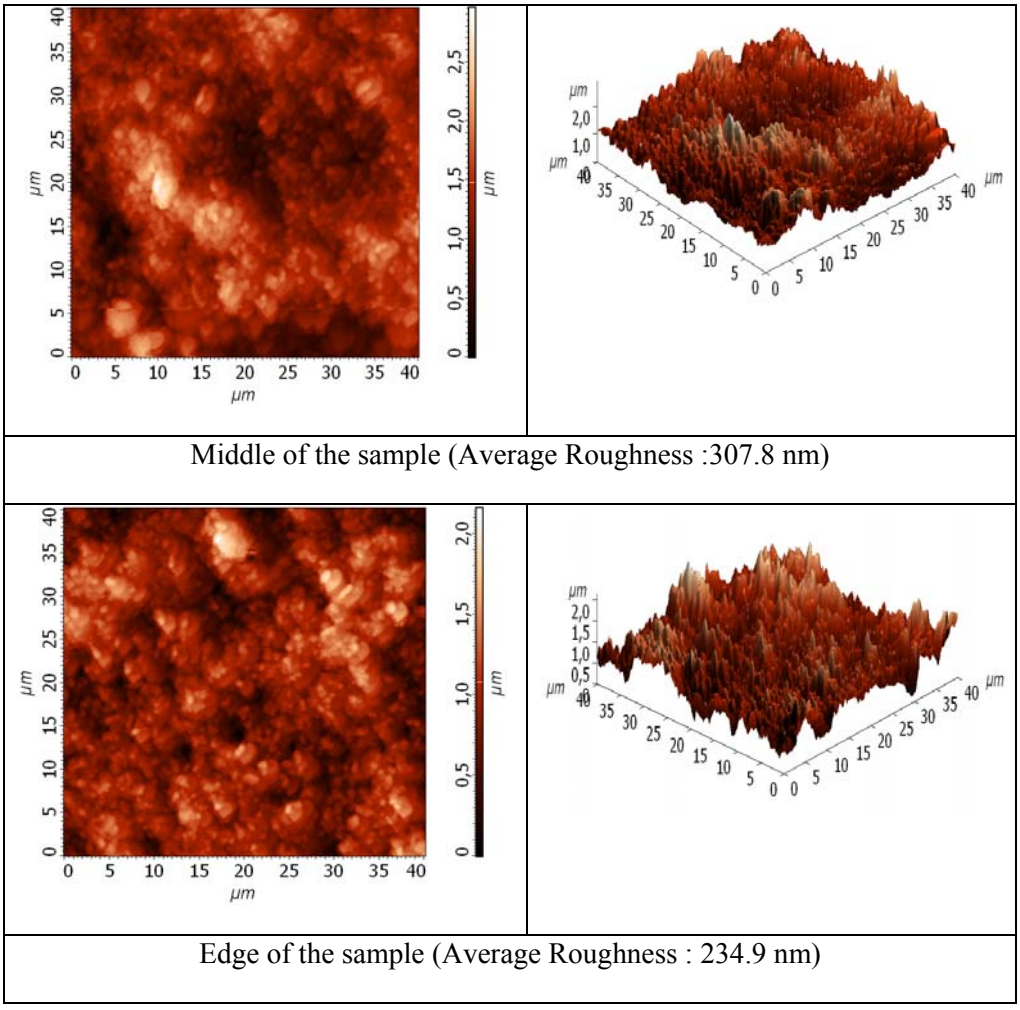

Figure 5. 16. *AFM topography of the films obtained by sintering the spin coated inks at 200°C. In (a) the middle section and in (b) the edge of the film.*

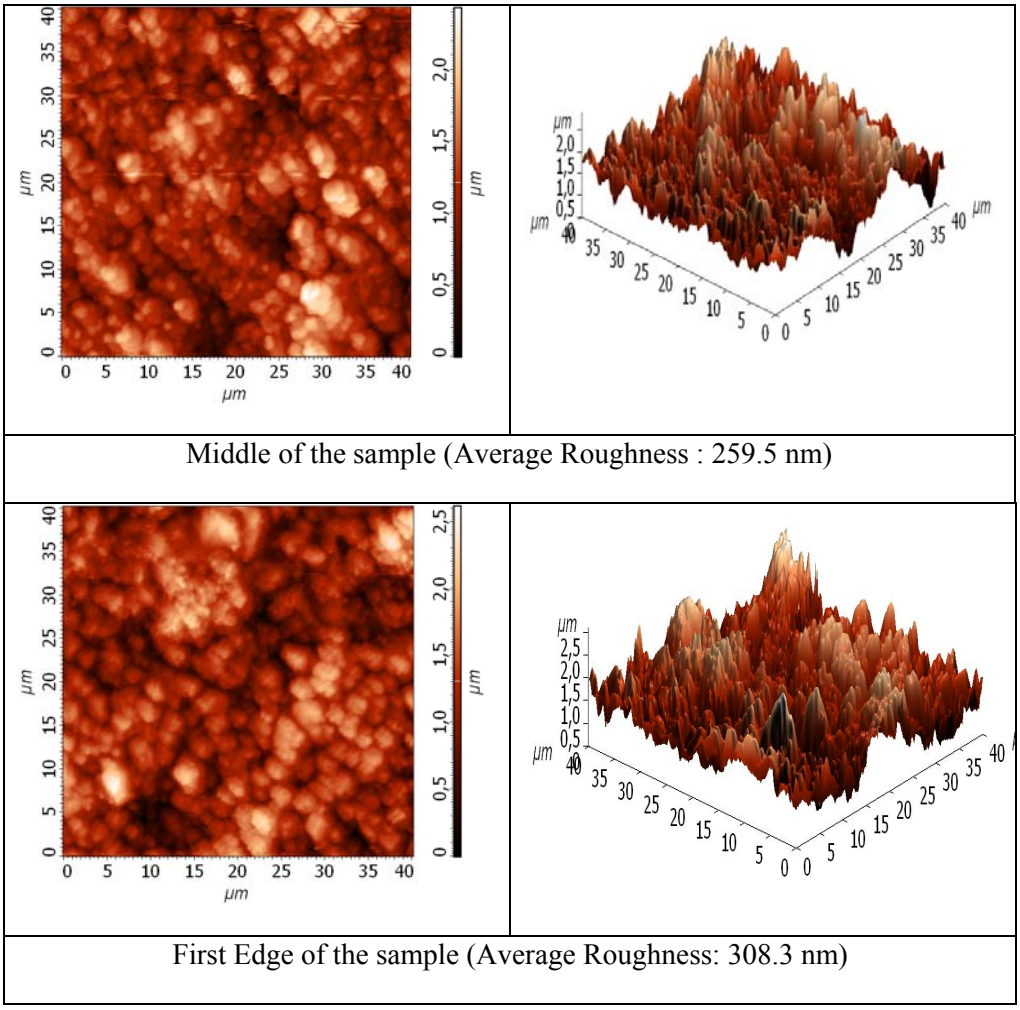

Figure 5. 17. *AFM topography of the films obtained by sintering the spin coated inks at 400°C. In (a) the middle section and in (b) the edge of the film.*

5.2.5. UV-Vis-NIR Spectroscopy

The UV-Vis-NIR spectra for the films obtained sintering the IA-P4-1 and IA-P4-40 inks at 400°C are shown in *figure 5.17*. The peaks at 450 nm, 530 nm and around 590nm (IA-P4-40) and 600 nm (IA-P4-1) nm indicate slight change in absorbance in the visible range.590nm and 600nm corresponds to energy values of

2.1eV- 2.0eV. This approximate value is consistent with the energy bandgap of bulk Cu_2O [19]. The same behaviour is obtained for all inks, independent of the initial particle size. The features are compatible with those of traditional Cu_2O films. The initial nanometric size of the cuprite particles has therefore little influence on the final optical properties of the film: it is however a prerequisite for an effective reduction of the sintering temperature.

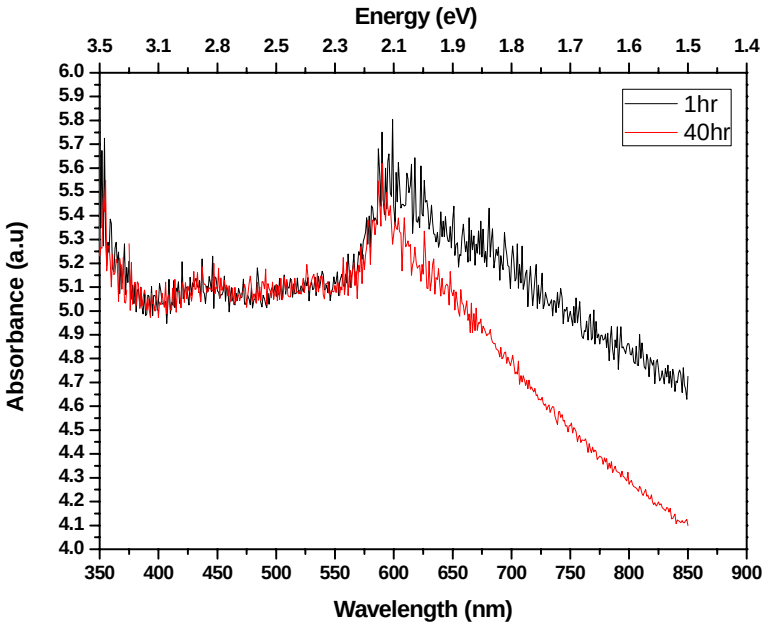

Figure 5. 18. *UV-Vis-NIR spectra of the films produced by heat treating the IA-P4-1 and IA-P4-40 inks at 400 °C.*

The optical energy band gap could not be calculated from the absorbance plots using the classical Tauc approach due to strong scattering of the ink particles.

5.2.6 Photoluminescence

The photoluminescence of the specimens obtained by heat treating the deposited inks at 400°C was investigated to judge the optical performance of the films and the possible appearance of extra absorbption due to the presence of intermediate bands or defect sites. The film obtained from the IA-P4-20 ink shows

an important luminescence in the infrared around 870 nm (*see figure 5.18*). Some residual luminescence is also observed at slightly higher energy (850 nm wavelength) for the film obtained from the IA-P4-10 ink. Luminescence seems absent for the IA-P4-40 derived specimens.

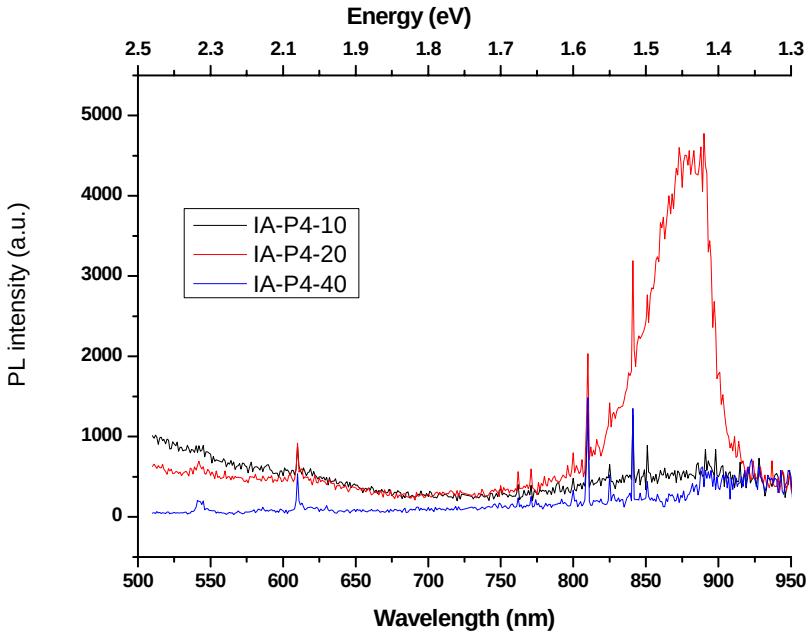

Figure 5. 19. *PL measurement of IA-P4 ink particles sintered at 400°C.*

To confirm the observation, a further measurement was done by removing the filter placed just after the laser (employed to clean the laser signal) so to increase the power delivered by the laser on the specimen. A small peak appears around 900 nm, confirming a red shift of the signal for decreasing domain size. Above 950 nm the spectrum becomes very noisy due to intrinsic limitations of the instrument employed for the analysis. The observed luminescence effect indicates the presence of defect sites (supporting recombination) consistent with the high dislocation density observed by XRD.

5.4. CONCLUSIONS

A set of stable inks based on nanostructured Cu_2O was produced using rather inexpensive techniques. X-ray diffraction indicates that the crystalline domains in the ink are in the 6 – 22 nm. Films can be obtained by spin-coating the ink and a good compaction is observed at temperatures as low as 400 °C. The best results in term of reduced roughness and uniformity are obtained with the inks of smaller size. Tests are in progress to optimise the inks further in order to employ them for the active layers of a printable solar cell.

REFERENCES

1 http://www.superstrate.net/pv/illumination/spectrum.html

2 A. Hagfeldt, M. Gratzel, "Light-Induced Redox Reactions in Nanocrystalline Systems", *Chem. Rev.*, **95**, 49, (1995).

3 A Henglein, "Small-particle research: physicochemical properties of extremely small colloidal metal and semiconductor particles", *Chem. Rev.*, **89**, 1861–1873, (1989)

4 T. D. Golden, M.G. Shumsky, Y. Zhou, R. A. Vander Werf, R. A. Van Leeuwen, J. A. Switzer, "Electrochemical Deposition of Copper(I) Oxide Films", *Chem. Mater.*, **8 (10)**, 2499–2504, (1996).

5 G. Rothenberger, J. Moser, M. Gratzel, N. Serpone, D. K. Sharma, "Charge carrier trapping and recombination dynamics in small semiconductor particles" *J. Am. Chem. Soc.*; **107[26]**, 8054 – 8059, (1985).

6 (http://en.wikipedia.org/wiki/Solar_cell)

7 C. P. Collier, T. Vossmeyer, "Quantum Dot Superlattices," *J. R. Heath, Annu. Rev. Phys. Chem.,* **49**, 371, (1998)

8 C. B. Murray, C. R. Kagan, M. G. Bawendi, "Synthesis and characterization of monodisperse nanocrystals and close-packed nanocrystal assemblies", *Annu. Rev. Mater.Sci.,* **30**, 545, (2000).

9 L. Mangolini, U. Kortshagen, "Plasma-Assisted Synthesis of Silicon Nanocrystal Inks". *Adv. Mater.,* **19**, 2513–2519, (2007).

10 D. S. Ginger, N. C. Greenham, "Charge injection and transport in films of CdSe nanocrystals," *J. Appl. Phys*., **87[3]**, 1361, (2000).

11 N. Y. Morgan, C. A. Leatherdale, M. Drndic, M. V. Jarosz, M. A Kastner, M. Bawendi, "Electronic transport in films of colloidal CdSe nanocrystals", *Phys. Rev. B: Condensed Matter and Materials Physics*,

66[7], 075331-075339, (2002).

12 D. Yu, C. Wang, B. L. Wehrenberg, P. Guyot-Sionnest, "Variable Range Hopping Conduction in Semiconductor Nanocrystal Solids", *Phys. Rev. Lett.,* (2004), **92[21]**, 216 802.

13 D. Yu, C.Wang, P. Guyot-Sionnest, "n-Type Conducting CdSe Nanocrystal Solids", *Science*, **300**, 1277, (2003).

14 P. Guyot-Sionnest, C.Wang, "Fast Voltammetric and Electrochromic Response of Semiconductor Nanocrystal Thin Films", *J. Phys. Chem. B,* (2003), **107[30]**, 7355–7359.

15 D. V. Talapin, C. B. Murray, "PbSe Nanocrystal Solids for n- and p-Channel Thin Film Field-Effect Transistors", *Science,* **310**, 86-89, (2005).

16 J. J. Urban, D. V. Talapin, E. V. Shevchenko, C. R. Kagan, C. B.Murray, "Synergism in binary nanocrystal Superlattices leads to enhanced p-type conductivity in self-assembled PbTe/Ag2Te thin films", *Nat. Mater.* **6**, 115, (2007).

17 D. Snoke, "Coherent Exciton Waves," *Science*, **273**, 1351, (1996).

18 J. P. Cline, R. D. Deslattes, J.L. Staudenmann, E. G. Kessler, L. T. Hudson, A. Hennins, and R. W. Cheary, "NIST Certificate (SRM 660a) ,LaB_6 ,Line Position and Line Shape Standard for Power Diffraction, Gaithersburg USA, NIST Standard Reference Materials Program", *NIST*, USA (2000).

19 S. Ishizuka, T. Maruyama and K. Akimoto "Thin-Film Deposition of Cu_2O by Reactive Radio-Frequency Magnetron Sputtering", *Jpn. J. Appl. Phys.,* **39,** L786-L788, (2000).

Conclusive remarks

and suggestions for future works

Conclusive remarks and suggestions for future works

The main objective of this thesis was to synthesize, characterise and investigate the possible applications of nanostructured copper oxides in the field of low cost renewable energies. The reason for studying nanostructured materials and not bulk ones is in the observation that nanometer scale structures could improve to a high extent the performance of optoelectronic devices. The extra performance is obtained practically via bandgap and defect engineering.

The investigations herein have been focused on the two most important oxides of copper: cuprite Cu_2O and tenorite CuO. Correlations have been sought between experimental process parameters and final microstructure in the production of defect-free Cu_2O and CuO. A bottom-up technique such as the synthesis in reverse micelle (water-in-oil) microemulsions (nanoreactors) has been employed in the production of these nanocrystals. The main process parameter identified as determinant to control the microstructure is the amount of water in relation to the fixed surfactant concentration. A relationship was found and theoretically described between the parameters of the microemulsion and the average domain size obtained. Nanometric particles in the range 2-20 nm were obtained, exhibiting a characteristic bimodal distribution. The occurrence of this bimodal distribution was elucidated considering the growth mechanisms of cuprite in a micellar system.

The effect of light on the stability of the Cu_2O nanoparticles in water was also elucidated, indicating the possible use of the prepared nanocrystals in photocatalytic applications.

The microemulsion technique was extended to the synthesis CuO nanocrystals. In that, a viable solution was working at high temperature to favour the formation of CuO versus Cu_2O. By profiting of the self-assembling of the

particles synthesised in the nanoreactors, a set of nanorod-like structures consisting of directional arrangement of spherical particles was obtained. XRD analysis identified the primary spheres being of the order of 2 - 9 nm whereas the overall nano objects, measured by TEM, were of the order of 50 nm. The growth mechanism has been highlighted.

This small size of the composing spherical domains tends to influence the optical properties of the nanorods that show a characteristic strong blue shift in both absorption and photoluminescence spectra. Quantum size effects and the correlation between particle size and optical energy bandgap was investigated, showing a clear bandgap expansion with decreasing domain size. In particular, the CuO particles showed band gaps of 2.1 - 2.7 eV compared to the 1.2 - 1.8 eV of the bulk component.

As part of the defect engineering process, a top-down approach was also proposed to produce highly defective nanostructured Cu_2O powders with a potential use in new generation intermediate-band solar cells. High energy milling, using a suitably modified vibrating-cup mill allowing operation under controlled environment and temperature, was employed to produce highly defective and relatively pure cuprite nanopowders. The effect of milling duration on the final microstructure was investigated using both laboratory and synchrotron radiation X-ray diffraction. The results, supported by High Resolution TEM and SEM analysis established a strong influence of the process parameters on the microstructure in terms size reduction, lattice expansion, defects levels/concentration, such as the possibility of loading the particles with a dislocation density as high as $\rho \approx 4\times10^{-16}$ m^{-2}.

The availability of nanopowders with a high content of stored (elastic) energy was identified as possible solution for the production of compact films using an ink-based technique. In fact it is known that sintering temperature can be highly reduced in nanopowders and when extra stored energy is available. Milling

was thus employed in the production Cu_2O inks with potential photonics applications. It is expected that these inks could be applied in low cost printable solar cells and gas sensors. A set of stable inks has been produced and corresponding films sintered at temperatures as low as 300 °C. The microstructure and optical properties of the films led us to establish the potential of these inks in the proposed solar cells and gas sensors.

This last part of the work is still in the preliminary research stage, but the first results are very promising; complete or conclusive results are therefore not yet available. It is expected that in the very near future a prototype solar cell - currently under preparation - will be completed. Further investigations are ongoing to improve the effect of mobility, resistivity and the temperature ranges to allow for an easy production of a multijunction solar cell. Further, the inks can be easily printed on substrates like alumina to produce cost effective alumina/copper oxide gas sensors.

Scientific Production

- D. Dodoo-Arhin, M. Leoni, P. Scardi, E. Garnier, A. Mittiga, "Synthesis, Characterization and stability of Cu_2O nanoparticles produced via reverse micelles microemulsion", *Materials Chemistry and Physics*,2010, doi:10.1016/j.matchemphys.2010.03.053 ,(online).
- Scardi P., Leoni M., Dodoo-Arhin D., "On the modelling of diffraction line profiles". *Solid State Phenomena,* **163**, 19-26, (2010.) doi:10.4028/www.scientific.net/SSP.163.19.
- D. Dodoo-Arhin, G. Vettori, M. D'Incau, M. Leoni, P. Scardi, "High Energy Milling of Bulk Cu_2O powder", *Z. Krist Suppl.*, 2010.-Paper *(Submitted*)
- D. Dodoo-Arhin, M. Leoni, P. Scardi, "Microemulsion synthesis of CuO nanorod-like structures", *Materials Science and Engineering: A*, 2010 - Paper (*submitted*).
- D. Dodoo-Arhin, M. Leoni, P. Scardi, "Copper oxide photonic inks", (*in preparation*).